Stability Analysis and Robust Controller Design of Indirect Vector Controlled Induction Motor

Jitendra Kumar Jain

Department of Electrical Engineering
National Institute of Technology Rourkela

Stability Analysis and Robust Controller Design of Indirect Vector Controlled Induction Motor

Dissertation submitted in partial fulfillment

of the requirements of the degree of

Doctor of Philosophy

in

Electrical Engineering

by

Jitendra Kumar Jain

(Roll Number: 512EE1010)

based on research carried out

under the supervision of

Prof. Sandip Ghosh

and

Prof. Somnath Maity

December, 2017

Department of Electrical Engineering

National Institute of Technology Rourkela

Department of Electrical Engineering
National Institute of Technology Rourkela

December 29, 2017

Certificate of Examination

Roll Number: *512EE1010*
Name: *Jitendra Kumar Jain*
Title of Dissertation: *Stability Analysis and Robust Controller Design of Indirect Vector Controlled Induction Motor*

We the below signed, after checking the dissertation mentioned above and the official record book (s) of the student, hereby state our approval of the dissertation submitted in partial fulfillment of the requirements of the degree of *Doctor of Philosophy* in *Electrical Engineering* at *National Institute of Technology Rourkela*. We are satisfied with the volume, quality, correctness, and originality of the work.

Somnath Maity Co-Supervisor	Sandip Ghosh Principal Supervisor
K. B. Mohanty Member, DSC	Susovon Samanta Member, DSC
Anup Kumar Panda Chairman, DSC	I. N. Kar External Examiner

Department of Electrical Engineering
National Institute of Technology Rourkela

Prof. Sandip Ghosh
Assistant Professor

Prof. Somnath Maity
Assistant Professor

December 29, 2017

Supervisors' Certificate

This is to certify that the work presented in the dissertation entitled *Stability Analysis and Robust Controller Design of Indirect Vector Controlled Induction Motor* submitted by *Jitendra Kumar Jain*, Roll Number 512EE1010, is a record of original research carried out by him under our supervision and guidance in partial fulfillment of the requirements of the degree of *Doctor of Philosophy* in *Electrical Engineering*. Neither this dissertation nor any part of it has been submitted earlier for any degree or diploma to any institute or university in India or abroad.

Somnath Maity
Assistant Professor

Sandip Ghosh
Assistant Professor

Dedication

This research work is dedicated to my loving family ...

Signature

Declaration of Originality

I, *Jitendra Kumar Jain*, Roll Number *512EE1010* hereby declare that this dissertation entitled *Stability Analysis and Robust Controller Design of Indirect Vector Controlled Induction Motor* presents my original work carried out as a doctoral student of NIT Rourkela and, to the best of my knowledge, contains no material previously published or written by another person, nor any material presented by me for the award of any degree or diploma of NIT Rourkela or any other institution. Any contribution made to this research by others, with whom I have worked at NIT Rourkela or elsewhere, is explicitly acknowledged in the dissertation. Works of other authors cited in this dissertation have been duly acknowledged under the sections "Reference" or "Bibliography". I have also submitted my original research records to the scrutiny committee for evaluation of my dissertation.

I am fully aware that in case of any non-compliance detected in future, the Senate of NIT Rourkela may withdraw the degree awarded to me on the basis of the present dissertation.

December 29, 2017
NIT Rourkela

Jitendra Kumar Jain

Acknowledgment

First and foremost, I would like to express my deep sense of respect and gratitude towards my supervisor Prof. Sandip Ghosh and co-supervisor Prof. Somnath Maity, who have been the guiding force behind this work. I want to thank them for introducing me to the field of Induction Motor Drives Control and giving me the opportunity to work under them. Their undivided faith in this topic and ability to bring out the best of analytical and practical skills in people has been invaluable in tough periods. Without their invaluable advice and assistance with all kinds of support it would not have been possible for me to complete this thesis. I am greatly indebted to them for their constant encouragement and invaluable advice in every aspect of my research career. I consider it my good fortune to have got an opportunity to work with such wonderful persons.

I thank our H.O.D. Prof. Jitendriya Kumar Satapathy and DSC chairman Prof. Anup Kumar Panda for their blessings and constant support in my thesis work. They have been great sources of inspiration to me and I thank them from the bottom of my heart.

I would also like to thank all faculty members to provide me their regular suggestions and encouragements during the whole work.

At last but not the least I am in debt to my family to support me regularly during my hard times.

I wish to thank all PhD scholars, my seniors and juniors, all colleagues and secretarial staff of the EE Department for their sympathetic cooperation.

December 29, 2017 *Jitendra Kumar Jain*

NIT Rourkela Roll Number: 512EE1010

Abstract

The thesis considers stability analysis and controller design through different performance measures for indirect vector controlled induction motor (IVCIM). These problems are known to be complex due to nonlinearity, large order and multi-loop scenario. Some new approaches and results on IVCIM are proposed in this work.

IVCIM dynamics is well known for having different bifurcation behavior, viz., saddle-node, Hopf, Bogdanov–Takens and Zero–Hopf bifurcations due to rotor resistance variation. These bifurcations affect the control performance and may lead to stalling or permanent damage of motor. A numerical analysis of these bifurcations for proportional integral (PI) controlled IVCIM is made in this thesis using full-order induction motor model (stator dynamics is included). This analysis aids to determine the allowable bifurcation parameter variation range as well as suitable choice of speed-loop gains to avoid these. Some new observations on the bifurcation behavior are made. Simulation and experimental results are presented validating the bifurcation behaviors.

For improving dynamic performance in the presence of load torque and rotor resistance variation, a new method for designing PI gains is proposed for IVCIM. The inner-loop current PI controllers are tuned simultaneously along with the speed controller. This method is implemented using a static output feedback scheme in which iterative linear matrix inequality (ILMI) based H_∞ control technique is employed. Such a design makes stator currents and speed response to be robust against rotor resistance and load variations. A comparison between proposed design and a conventional one is shown using simulation and experimental results that validate the superiority of the proposed approach.

Owing to multi-loop and nonlinear system behavior, IVCIM dynamics is known to have coupling in between the two inner-loop stator current components (flux and torque). Such coupling affects the dynamic torque output of the motor. Decoupling of the stator currents are important for smoother torque response of IVCIM. Conventionally, additional feedforward decoupler is used to take care of the coupling that requires exact knowledge of the motor parameters and additional circuitry or signal processing. A method is proposed to design the regulating PI gains while minimizing coupling without any requirement of additional decoupler. The variation of the coupling terms for change in load torque is considered as the performance measure. The same ILMI based H_∞ control design approach is used to obtain the controller gains. A comparison between the conventional feedforward decoupling and proposed decoupling scheme is presented through simulation and experimental results that

establish the effectiveness of the proposed method riding over its simplicity.

Finally, since the PI controller can yield limited performance, a dynamic controller is designed for the IVCIM drive system. In the design process, iron-loss dynamics are incorporated into induction motor model to fetch benefit through better performance. A sequential design method is used for the controller design in which, first, the inner-loop controllers are designed. The designed inner-loop controllers is then used for designing the outer speed-loop controller. The proposed design employs ILMI based H_∞ control design for dynamic output feedback controller that makes stator currents and speed response to be robust against disturbances. A comparison among proposed dynamic controller design, PI controller and compensator design is shown using simulation and experimental results demonstrate enhanced performance of the proposed controller and suitability for industrial purpose.

***Keywords*: *Induction motor*; *indirect vector control*; *rotor resistance*; *equilibrium point*; *bifurcation phenomenon*; *speed-loop*; *current-loop*; *proportional integral control*; *iterative linear matrix inequality*; *decoupling*; *sensitivity*; *dynamic controller*.**

Contents

Certificate of Examination ii

Supervisors' Certificate iii

Dedication iv

Declaration of Originality v

Acknowledgment vi

Abstract vii

List of Figures xii

List of Tables xvi

Nomenclature xvii

1 Introduction 1

1.1 Background 1

1.2 Motivation 1

1.3 Main Objectives of the Thesis 2

1.4 Thesis Layout 3

2 Modeling and Control of Three-Phase Induction Motor 5

2.1 Introduction 5

2.2 Induction Motor (IM) Modeling 5

2.2.1 Two-Phase Transformation 7

2.2.2 Axes Transformation 7

2.2.3 Stationary Reference Frame Model 9

2.2.4 Synchronous Reference Frame Model 11

2.3 Control Techniques for Induction Motor 13

2.3.1 Volts/Hz or V/f Control 13

2.3.2 Vector Control 14

2.3.3 Direct Torque Control 18

2.4 Control Techniques Comparison 19

2.5 IM Controller Under Study . . . 20
2.6 Chapter Summary . . . 20

3 A Numerical Bifurcation Analysis of IVCIM 22
3.1 Introduction . . . 22
3.2 General IVCIM . . . 23
3.2.1 Higher-Order Model (HOM) . . . 23
3.2.2 Equilibrium Point . . . 25
3.2.3 Lower-Order Model (LOM) . . . 27
3.2.4 Linearization . . . 28
3.3 Bifurcation Analysis of General IVCIM . . . 29
3.3.1 Saddle-Node Bifurcation (SNB) . . . 30
3.3.2 Hopf Bifurcation (HB) . . . 32
3.3.3 Bogdanov–Takens Bifurcation (BTB) . . . 34
3.3.4 Zero-Hopf Bifurcation (ZHB) . . . 35
3.4 Bifurcation Analysis of Classical IVCIM . . . 36
3.4.1 SNB . . . 38
3.4.2 HB . . . 40
3.4.3 BTB . . . 41
3.4.4 ZHB . . . 41
3.5 Simulation Results . . . 42
3.6 Experimental Results . . . 44
3.7 Chapter Summary . . . 46

4 Concurrent Speed and Current-Loop PI Tuning for IVCIM 48
4.1 Introduction . . . 48
4.2 IVCIM Model . . . 49
4.2.1 Decoupled Controller Design . . . 50
4.2.2 Concurrent Inner and Outer-Loop Design . . . 55
4.2.3 Iterative LMI Algorithm . . . 57
4.3 Simulation Results . . . 60
4.3.1 Decoupled Design . . . 60
4.3.2 Proposed Design . . . 60
4.3.3 Bandwidth Comparison . . . 61
4.3.4 Robustness Evaluation . . . 61
4.4 Experimental Results . . . 63
4.5 Chapter Summary . . . 68

5 Decoupling PI Controller Design for IVCIM 69
5.1 Introduction . . . 69

5.2 System Under Study . . . 71
5.3 Inner-loop Feedforward Decoupler . . . 71
5.3.1 Decoupler Sensitivity . . . 72
5.4 Coupling Minimization Problem . . . 75
5.5 Validation and Discussions . . . 76
5.5.1 Simulation Results . . . 76
5.5.2 Experimental Results . . . 80
5.6 Chapter Summary . . . 82

6 A Dynamic Controller Design for IVCIM 83
6.1 Introduction . . . 83
6.2 The Proposed Dynamic Controller . . . 84
6.3 IVCIM Model . . . 85
6.4 Control Problem Formulation . . . 87
6.4.1 Current-Loop Model . . . 88
6.4.2 Speed-Loop Model . . . 90
6.5 Performance Evaluation . . . 95
6.5.1 Simulation Results . . . 95
6.5.2 Experimental Test . . . 96
6.6 Chapter Summary . . . 100

7 Conclusion and Future work directions 101
7.1 Thesis summary . . . 101
7.2 Contribution of the Thesis . . . 101
7.3 Future Research Directions . . . 103

Appendix A Nonlinear Dynamical System 105
A.1 Equilibrium point . . . 105
A.2 Linear System . . . 105
A.3 Linearization . . . 106
A.4 Characteristics of Nonlinear System . . . 106
A.4.1 Multiple Isolated Equilibrium Points . . . 107
A.4.2 Limit Cycles . . . 107
A.4.3 Finite Escape Time . . . 108
A.4.4 Bifurcations . . . 108

References 112

Dissemination 121

List of Figures

2.1 Schematic representation of a two-pole, three-phase IM. 6
2.2 Three-phase to two-phase transformation. 8
2.3 β equivalent IM model for stationary reference frame. 10
2.4 α equivalent IM model for stationary reference frame. 10
2.5 q equivalent IM model for synchronous reference frame. 12
2.6 d equivalent IM model for synchronous reference frame. 12
2.7 V/f Control scheme for IM. 14
2.8 Current vectors in dc motor and IM. 15
2.9 Principle of vector control technique. 15
2.10 Direct vector control of IM. 16
2.11 Indirect vector control of IM. 17
2.12 Direct torque control of IM. 19

3.1 Indirect vector control of induction motor. 24
3.2 (a) Variation of eigenvalue. (b) Variation in α_s. (c) Bifurcation curves for α_s with T_L. 30
3.3 (a) Variation of α_H for $K_{i\omega} = 30$. (b) Variation of α_H for $K_{p\omega} = 0.2$. (c) Variation of eigenvalues w.r.t. α. 31
3.4 Variation of α_H with T_L for different α, $K_{p\omega} = 0.1$ and $K_{i\omega} = 30$: (i) α_H below α_s, (ii) α_H above α_s. 33
3.5 Variation of α for BTB with $K_{i\omega} = 30$ at: (a) $\alpha < 1$, (b) $\alpha > 1$. 34
3.6 (a) Variation of α for $K_{i\omega} = 30$. (b) Variation of α for $K_{p\omega} = 0.2$. (c) Variation of eigenvalues w.r.t. α. 35
3.7 (a) Variation of α_H at $K_{i\omega}$=40 for the IM in [1]. (b) Variation of α_H at $K_{i\omega}$=30 for the IM in [2]. 36
3.8 Indirect vector control of induction motor. 37
3.9 Variation in equilibrium points with α at $T_L = 3$ N·m. 39
3.10 Bifurcation curves indicating change in equilibria with T_L. 39
3.11 Variation of eigenvalues w.r.t. α for $T_L = 3$ N·m: (a) Dominant eigenvalue 1, and (b) Dominant eigenvalue 2. 39
3.12 (a) Variation of α_H for $K_{i\omega} = 30$. (b) Variation of α_H for $K_{p\omega} = 0.2$. . . . 40
3.13 Variation of a pair of eigenvalues w.r.t. α when $T_L = 2$ N·m. 40

3.14 Variation of α with T_L for BTB at $K_{i\omega} = 30$. 41
3.15 Variation of α with T_L for ZHB at $K_{i\omega} = 30$. Variation of eigenvalues w.r.t. α when $T_L = 2.89$ N·m. 42
3.16 Simulation response of i_{qs} at: (a) $\alpha = 1.39$, (b) $\alpha = 0.76$, (c) $K_{p\omega} = 0.1$, $K_{i\omega} = 30$ and $\alpha = 2.43$, (d) $K_{p\omega} = 0.1$, $K_{i\omega} = 30$ and $\alpha = 2.145$, (e) $K_{p\omega} = 0.2$ and $K_{i\omega} = 30$, (f) $K_{p\omega} = 0.1$, $K_{i\omega} = 30$ and step change in α from 2.1 at 4 sec to 2.4 at 10 sec for $T_L = 5.12$ N·m, (g) $\alpha = 3.43$, (h) $K_{p\omega} = 0.1$, $K_{i\omega} = 30$, $\alpha = 2.71$ for $T_L = 2$ N·m, (i) $K_{p\omega} = 0.2$, $K_{i\omega} = 30$, step change in α from 2.71 at 4 sec to 5.2 at 10 sec for $T_L = 2$ N·m, (j) $K_{p\omega} = 0.2$, $K_{i\omega} = 25$ and $\alpha = 5.5$, and (k) $K_{p\omega} = 0.1$, $K_{i\omega} = 30$ and step change in α from 3.4 at 2 sec to 3.7 at 12 sec for $T_L = 2.90$ N·m, respectively. 43
3.17 Experimental setup. 44
3.18 Experimental response of i_{qs} for general IVCIM at $K_{p\omega} = 0.9$, $K_{i\omega} = 2$ for change in α as: (a) $1 \rightarrow 0.5 \rightarrow 0.2$, (b) $1 \rightarrow 0.1$, and (c) $1 \rightarrow 1.5 \rightarrow 2.5 \rightarrow 3$. 45
3.19 Experimental response of i_{qs}. (a) Generalized case: $K_{p\omega} = 0.1$, $K_{i\omega} = 2$ for change in α as $1 \rightarrow 1.5$. (b) Classical case: $K_{p\omega} = 0.9$, $K_{i\omega} = 2$ for change in α as $1 \rightarrow 1.5 \rightarrow 2.5 \rightarrow 3$. (c) Classical case: $K_{p\omega} = 0.1$, $K_{i\omega} = 2$ for change in α as $1 \rightarrow 1.8$. 46

4.1 Inner-loop control of induction motor drive system. 51
4.2 SOF controller design problem. 53
4.3 Bode bandwidth plot for decoupled inner and outer-loop controllers: (a) Inner-loop. (b) Outer-loop. 62
4.4 Bode bandwidth plot for concurrent inner-loop controller. 62
4.5 Bode bandwidth plot for concurrent outer-loop controller. 63
4.6 Decoupled design simulation results for step change in T_L. (a) i_{ds}. (b) i_{qs}. (c) ω_r. 63
4.7 Comparison between existing and proposed design for step change in ω_{ref} at $\delta = 0$: (a)-(c) existing design, (d)-(f) proposed design. 64
4.8 Variation of motor speed and stator currents for step change in $T_L = 6.5$ N·m at $\omega_{ref} = 130$ rad/sec for proposed design: (a) i_{ds}. (b) i_{qs}. (c) ω_r. . . 64
4.9 Experimental result with decoupled design for variation in T_L at $\omega_{ref} = 130$ rad/sec at $\delta = 0$: (a) Stator currents. (b) Motor speed ω_r. 65
4.10 Experimental result with decoupled design for variation in T_L at $\omega_{ref} = 130$ rad/sec at $\delta = 0.2\sigma$: (a) Stator currents. (b) Motor speed ω_r. 65
4.11 Experimental result with proposed concurrent design for variation in T_L at $\omega_{ref} = 130$ rad/sec: (a) $\delta = 0$. (b) $\delta = 0.2\sigma$. 65
4.12 Experimental result with existing design for variation in ω_{ref} at $\delta = 0$: (a) Motor speed ω_r. (b) Stator currents i_{ds} and i_{qs}. 66

4.13 Experimental result of ω_r with proposed design for variation in ω_{ref}: (a) $\delta = 0$, (b) $\delta = 0.2\sigma$. 66
4.14 Experimental results for variation in ω_{ref} from $100 \rightarrow 150 \rightarrow 100$ rad/sec at $\delta = 0$: (a) Existing design of [3]. (b) Proposed design. (c) $K_{p\omega} = 0.5$ and $K_{i\omega} = 1.5$. (d) $K_{p\omega} = 1$ and $K_{i\omega} = 3$. 67
4.15 Experimental result of current tracking performance for change in: (a) T_L. (b) ω_{ref}. 68

5.1 (a) Feedforward decoupling of inner-loop. (b) Behavior of i_{ds} for feedforward decoupling scheme. 72
5.2 Sensitivity of i_{ds} on controller gains: (a) Without decoupler. (b) With decoupler. 74
5.3 Sensitivity of i_{ds} with variation in frequency at $\omega_e = 80$ rad/sec: (a) Varying K_{pd}, K_{pq}. (b) $K_{pd} = K_{pq} = 100$ and 35% overestimation of R_r and L_m. . 74
5.4 Sensitivity of i_{ds} on change in R_r with variation in frequency for feedforward decoupler: (a) $K_{pd} = K_{pq} = 10$. (b) Varying K_{pd}, K_{pq}. 75
5.5 Bode plot for inner-loop PI controllers: (a) d current component. (b) q current component. 77
5.6 Comparison between proposed and feedforward decoupling for a step $T_L = 6.5$ N·m applied at 10 sec: (a) Stator current i_{ds}. (b) Stator current i_{qs}. . . . 79
5.7 ω_r for change in ω_{ref} in step $(100 \rightarrow 150)$. 79
5.8 Parameter variation effect on behavior of i_{ds}. 79
5.9 Measurement noise affect on i_{ds}: (a) Feedforward decoupling. (b) Proposed decoupling 80
5.10 Experimental result for variation in T_L: (a) Without decoupling [4]. (b) Without decoupling [1]. (c) Feedforward decoupling. (d) Proposed decoupling. 81
5.11 Experimental result for change in ω_{ref} in step $(100 \rightarrow 150 \rightarrow 100)$. . . . 81
5.12 Experimental result of current tracking performance for change in: (a) T_L. (b) ω_{ref}. 82

6.1 Indirect vector control scheme for induction motor. 84
6.2 Controller structure. 85
6.3 $d-q$ axis equivalent circuit with iron core loss:(a) d-equivalent circuit. (b) q-equivalent circuit. 87
6.4 Block-diagram of a feedback control system with disturbance. 87
6.5 Iron loss affect on stator current i_{qs}: (a) i_{qs} with change in T_L (6.5 N·m). (b) i_{qs} with change in ω_{ref} (100 rad/sec to 140 rad/sec at $T_L = 5$ N·m). . . 92

6.6 Comparison between proposed design and conventional PI when $T_L = 6.5$ N·m is applied at 10 sec for $\omega_{ref} = 130$ rad/sec: (a) Motor speed; (b) Stator current i_{qs}. 95
6.7 Comparison between proposed design and conventional PI when ω_{ref} is increased from 100 to 150 rad/sec: (a) Motor speed; (b) Stator current i_{qs}. . 96
6.8 Experiment result for variation in T_L from 0 to 6.5 N·m at $\omega_{ref} = 130$ rad/sec: (a)-(b) Conventional PI. (c)-(d) Proposed design. 97
6.9 Experiment result for existing speed loop design [3] at $\omega_{ref} = 130$ rad/sec. 98
6.10 Experiment result for variation in ω_{ref} from $100 \rightarrow 150 \rightarrow 100$ rad/sec: (a)-(b) Conventional PI. (c)-(d) Proposed design. 99
6.12 Experimental result of current tracking performance for change in: (a) T_L. (b) ω_{ref}. 99
6.11 Experiment result for variation in ω_{ref} from $100 \rightarrow 150 \rightarrow 100$ rad/sec at $\delta = 0$: (a) Conventional with $K_{p\omega} = 1$, $K_{i\omega} = 3$. (b) Dynamic controller without considering iron loss dynamics. 100

A.1 Limit cycle behavior. 107
A.2 Variation of eigenvalue for SNB. 109
A.3 Variation of eigenvalue for HB. 110

List of Tables

3.1 Comparison of equilibrium point 27
3.2 IM Parameters for analysis 30
3.3 Comparison of HB points at $T_L = 0$ N·m 41
3.4 Experimental IM Parameters 44

4.1 Initial Parameters for Algorithm 2 59
4.2 Controller gains 60

5.1 Initial Parameters for Algorithm 2 78
5.2 Controller gains 78

Nomenclature

R_s	Stator resistance	Ω
R_r	Rotor resistance	Ω
R_{fe}	Iron loss resistance	Ω
L_{ls}	Stator leakage inductance	H
L_{lr}	Rotor leakage inductance	H
L_s	Stator inductance	H
L_r	Rotor inductance	H
L_m	Magnetizing inductance	H
γ	Rotor time constant	sec
ω_r	Angular rotor electrical speed	rad/sec
ω_e	Synchronously rotating reference frame speed	rad/sec
ω_{sl}	Slip speed	rad/sec
s	Complex frequency	
P	Number of poles	
J	Moment of inertia	kgm^2
T_e	Electromagnetic torque	N·m
T_L	External load torque	N·m
B_m	Viscous friction coefficient	N·m/rad/s
i_{as}, i_{bs}, i_{cs}	Three-phase stator currents in real coordinates	A
i_{ar}, i_{br}, i_{cr}	Three-phase rotor currents in real coordinates	A
v_{as}, v_{bs}, v_{cs}	Three-phase stator voltages in real coordinates	V
v_{ar}, v_{br}, v_{cr}	Three-phase rotor voltages in real coordinates	V
ψ_{as},ψ_{bs},ψ_{cs}	Three-phase stator linkage fluxes in real coordinates	Wb
ψ_{ar},ψ_{br},ψ_{cr}	Three-phase rotor linkage fluxes in real coordinates	Wb
i_{ds}	Direct (d) stator current component	A
i_{qs}	Quadrature (q) stator current component	A
i_{dm}	Direct magnetizing current component	A
i_{qm}	Quadrature magnetizing current component	A
i_{dsref}	Reference current for i_{ds}	A
i_{qsref}	Reference current for i_{qs}	A

$i_{\alpha s}, i_{\beta s}$	Stator current components in $\alpha\beta$ coordinates (Clarke's Transformation)	A
$\psi_{\alpha s}, \psi_{\beta s}$	Stator flux components in $\alpha\beta$ coordinates (Clarke's Transformation)	Wb
$\psi_{\alpha r}, \psi_{\beta r}$	Rotor flux components in $\alpha\beta$ coordinates (Clarke's Transformation)	Wb
$v_{\alpha s}, v_{\beta s}$	Stator voltage components in $\alpha\beta$ coordinates (Clarke's Transformation)	V
v_{ds}	Direct (d) stator voltage component	V
v_{qs}	Quadrature (q) stator voltage component	V
ψ_{ds}	Direct stator flux component	Wb
ψ_{qs}	Quadrature stator flux component	Wb
ψ_{dr}	Direct rotor flux component	Wb
ψ_{qr}	Quadrature rotor flux component	Wb
ω_{ref}	Reference speed	rad/sec
ψ_{drref}	Reference rotor flux	Wb
K_{pd}	Direct current-loop proportional gain	
K_{pq}	Quadrature current-loop proportional gain	
K_{id}	Direct current-loop integral gain	
K_{iq}	Quadrature current-loop integral gain	
$K_{p\omega}$	Speed-loop proportional gain	
$K_{i\omega}$	Speed-loop integral gain	
α	Slip speed tuning gain or bifurcation parameter	
σ	Inverse of the rotor time constant	sec^{-1}

Chapter 1

Introduction

1.1 Background

Indirect vector control (IVC) of induction motor (IM) drives is used in industrial applications where high performance is required [5, 6]. Parameters of IM such as resistance, inductance may vary with temperature, ageing and other environmental reasons [7]. The IVC scheme is sensitive to changes in parameters, controller design and motor losses. These variations, particularly the rotor resistance variation, may lead to input-output torque nonlinearity, saturation of the machine and coupling of torque, flux component of stator currents [8, 9]. For minimizing the effect of this variation, several rotor resistance estimation schemes have been developed in [10–12]. However, an improper estimation may degrade the dynamic performance and lead to create bifurcation or chaos in control operation [9, 13–18]. In most of the industries, the classical proportional integral (PI) controller is preferred for IVCIM due to its simple structure and effectiveness [1, 3, 19]. The tuning of PI gains is important since rotor resistance and load variations may degrade performance. Owing to complex dynamics as induced by stator currents coupling, PI design is not straightforward. This current coupling increases with the motor speed and create non-smoothness of the torque response [4, 20]. Therefore, typically, a feedforward decoupling scheme is used to compensate the coupled terms [21]. However, it increases complexity and signal processing burden on the system. Although the PI controller is simple in structure, the tuning scheme can only bring some limited performance. Such limitations may cause large current overshoot for a sharp change in motor speed and load torque. A dynamic controller may overcome this limitation and can improve the performance of the motor.

1.2 Motivation

The rotor resistance variation may cause detuning in the indirect vector controlled induction motor (IVCIM) system [9]. Many rotor resistance estimation methods have been addressed [10–12, 22, 23] to compensate such detuning. However, the estimated resistance may vary beyond the stability limit of IM operation. Such detuning induce bifurcations into IM dynamics in steady-state. Mainly two types of bifurcations are observed:

1. PI tuning independent bifurcation (saddle node bifurcation (SNB))
2. PI tuning dependent bifurcation (Hopf bifurcation (HB), Bogdanov–Takens bifurcation (BTB), Zero–Hopf bifurcations (ZHB))

These bifurcations not only induce oscillations in IM dynamics, but also increase stator currents to very high value and may stall motoring operation. A priori knowledge of allowable stable rotor resistance variation range and suitable PI tuning may avoid these bifurcations. However, in existing literature, such bifurcations are not analyzed in detail and existing PI tuning rules to avoid these are limited to low load conditions.

The dynamic operation of IVCIM is also affected due to change in rotor resistance. Several modified controllers have been designed to improve the dynamic behavior of IM. However, these existing techniques are either based on reduced order model and decoupled design of inner current-and outer speed-loop controllers. In addition, a performance based PI controller design still not well reported in literature.

The IM dynamics are inherently coupled. In high speed applications, change in one reference quantity (either flux current or torque current) affects the other one. For mitigating the coupling affects, various type of decoupling schemes have been developed in literature. However, such techniques are based on modification or additional arrangement into conventional IVCIM. In addition, among these supplementary control methods, the simplest one is the feedforward decoupling. The decoupling is primarily affected by inner-loop current controller gains. A suitable choice of inner-as well as outer-loop PI gains may reduce the coupling effect and can improve (fast and smooth torque response) the dynamic operation of IVCIM.

For a sharp change in load and reference speed, a PI controller does not yield smooth response. A dynamical controller can overcome this limitation. In addition, IM also suffers from losses e.g. iron losses, stray losses, etc. Among these, the iron loss is considered to have more impacts on dynamic and steady-state behavior of IVCIM system. In existing literature, several reduced order model based controllers (decoupled structure) are designed to mitigate the affect of iron loss. However, a simple and dynamic performance based controller design, which consider parameter variations as well as iron loss dynamics has not been reported so far.

1.3 Main Objectives of the Thesis

A detailed stability analysis as well as robust controller design is in need to minimize the effects of the rotor resistance variation and improve the dynamic performance of IVCIM. The present work attempts to meet the following objectives.

- To determine the bifurcation conditions and its behavior on IM dynamics in order to obtain stability condition for rotor resistance variation and suitable outer speed-loop

gains that may avoid the bifurcations into IVCIM system.

- To devise methods for analysis considering full-order IM model.
- To improve the dynamic performance against the rotor resistance variation by robust design of current and speed-loop controllers.
- To investigate designing the PI controllers in order to minimize the dynamic coupling, possibly without any additional arrangement, e.g., feedforward decoupler.
- To design a higher-order dynamic controller compared to the conventional PI one for minimizing the affects of iron loss and parameter variations.

1.4 Thesis Layout

The thesis is organized in seven chapters. The contents of these chapters are summarized below:

Chapter 2 deals with the introduction to IM modeling. The most commonly used stationary and synchronous reference frame model for IM is discussed. The mathematical development of these models is also presented. Conventional control techniques comprising V/f, direct and indirect and DTC control with their principle of operation are briefed. A comparison among these techniques is also included.

Chapter 3 presents bifurcation analysis of the general and classical IVCIM in detail. SNB, HB, BTB and ZHB are analyzed with the occurrence conditions and bifurcations curves. An algorithm is constructed to determine the bifurcation points. These points are further used to obtain the PI tuning to avoid them. Experimental results are also presented to validate the analysis.

Chapter 4 covers the dynamic performance based concurrent PI tuning for current and speed-loop controllers in IVCIM. The design problem is framed in MIMO system framework involving full-order IM dynamics. An H_∞ based ILMI algorithm is used to obtain the controller gains. Experimental validation along with comparison to existing works are also presented.

Chapter 5 contains the development of robust PI control design technique for IVCIM to minimize the coupling affects. The feedforward decoupler and coupling sensitivity of the system with respect to current controller gains is presented. The dominating coupling terms are taken as performance measure to design the controller gains. H_∞ performance based ILMI algorithm (given in **Chapter 4**) is used to tune the controllers. Experimental validation of the proposed technique with comparison to the feedforward decoupling are demonstrated.

Chapter 6 presents a dynamic control design technique for IVCIM to overcome the limitations of the PI controller. It also improves the dynamic performance of the IVCIM

subjecting to iron loss and variation in rotor resistance. The controller is designed in the sequential control design framework. First, inner-loop controller is designed. The designed inner-loop current controller is then used for designing the outer speed-loop controller. The H_∞ based ILMI algorithm (given in **Chapter 4**) is used to determine the controller parameters. The IVCIM dynamics response with the proposed dynamical controller are compared with the existing PI controller using simulation as well as experimental works.

Chapter 7 presents a summary of the thesis contributions and contains the proposed future works.

Chapter 2

Modeling and Control of Three-Phase Induction Motor

2.1 Introduction

In most of the industrial applications, variable speed drives (VSD) are used in electrical and/or hybrid vehicles, pumps, elevators, ventilation, air conditioning, fans, robotics, machine tools, ship propulsion and rolling mills. In VSD, such applications are compiled with control of three types of motors dc, induction and synchronous. Among these motors, the dc motor control is simplest and have been preferred in fast torque and low speed applications [24]. However, owing to higher cost (due to commutator and brush assembly) and regular maintenance its applications are limited [25]. Whereas, due to cheaper cost, longer life, less maintenance, and development of semiconductor technology (e.g., insulated gate bipolar transistor) with fast signal processing (e.g., digital signal processor), three-phase IMs have been replaced dc motors [26–32]. These motors have covered most of the industrial use and hence helping in saving electrical energy.

In the next section, mathematical models and control techniques for Induction motor are covered. First, an equivalent model of three-phase IM in two-phase is derived. The two-phase model is represented in stationary and synchronous reference frames.

2.2 Induction Motor (IM) Modeling

The IM modeling is made with the underneath assumptions:

1. Both the stator and rotor windings are arranged symmetrically, wye connected, have three-phase and two poles.

2. The following are neglected: the dynamics associated with nonlinear magnetic circuits; the harmonic content of the magneto motive force (MMF) wave; variation in rotor resistance due to change in temperature and frequency.

Fig. 2.1 shows the schematic diagram of a two-pole, three-phase IM. The IM works on the principle that when stator windings are connected to a three-phase supply, a rotating magnetic

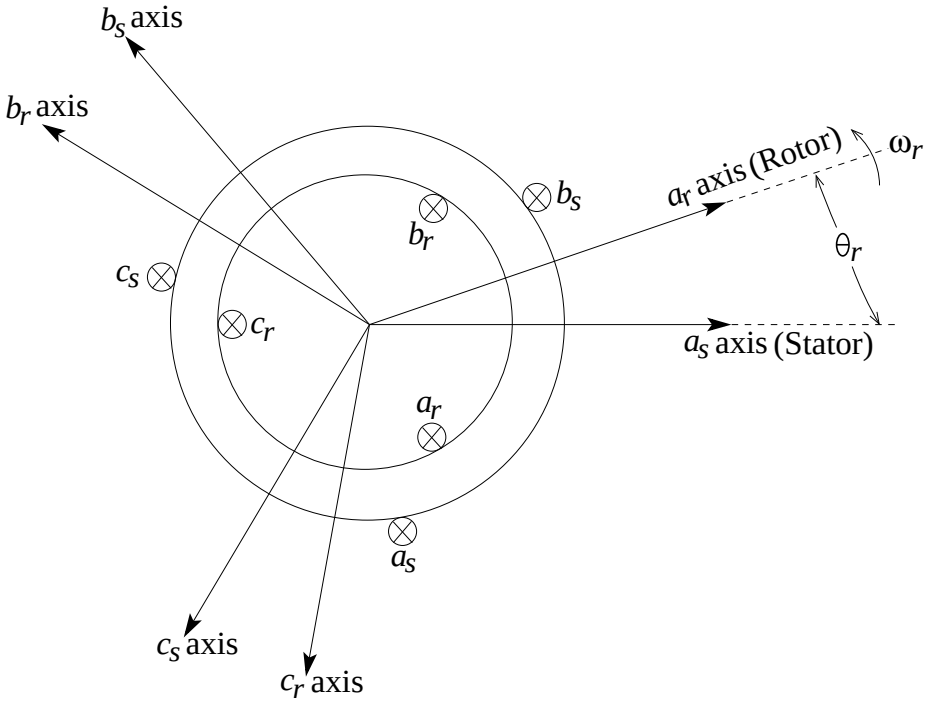

Figure 2.1: Schematic representation of a two-pole, three-phase IM.

field is generated into the air-gap. This magnetic field is rotated with the synchronous speed ω_e. The rotor part is short-circuited. The magnetic field induces a voltage into rotor windings that generates rotor current. When the generated rotor current is interacted with the air gap magnetic field, torque is produced. The rotor starts to rotate in a direction such that the relative speed between rotating magnetic field and rotor windings is reduced. In steady-state, the rotor is rotated with the speed, which is closer to its synchronous speed. If the rotor speed is matched with the synchronous speed, then the induced voltage and rotor current become zero and hence motor does not produce any torque. The difference between synchronous speed and rotor electrical speed is termed as a slip. It is defined mathematically as:

$$S = \frac{\omega_e - \omega_r}{\omega_e} \tag{2.1}$$

The three-phase stator voltage equations for the IM in stationary reference frame which is attached to the stator are given as

$$\left.\begin{aligned} v_{as} &= R_s i_{as} + \frac{d\psi_{as}}{dt} \\ v_{bs} &= R_s i_{bs} + \frac{d\psi_{bs}}{dt} \\ v_{cs} &= R_s i_{cs} + \frac{d\psi_{cs}}{dt} \end{aligned}\right\} \tag{2.2}$$

where i_{as}, i_{bs} and i_{cs} are the phase currents for each stator phase a, b and c, respectively; ψ_{as}, ψ_{bs} and ψ_{cs} defines the linkage flux associated with corresponding phase; R_s defines the stator phase resistance.

Similar to the stator side, the instantaneous rotor voltage equations for the stationary reference frame (attached to the rotor) can be written as

$$\left.\begin{aligned} v_{ar} &= R_r i_{ar} + \frac{d\psi_{ar}}{dt} \\ v_{br} &= R_r i_{br} + \frac{d\psi_{br}}{dt} \\ v_{cr} &= R_r i_{cr} + \frac{d\psi_{cr}}{dt} \end{aligned}\right\} \tag{2.3}$$

where phase currents, linkage fluxes and rotor phase resistance for the rotor phase are defined similarly to the stator phases.

Note that, the further development of modeling for a different number of poles can be determined by simply multiplying the number of poles to the torque equation.

2.2.1 Two-Phase Transformation

Since the rotor windings are considered in agreement with the stator windings, the dynamics analysis of IM in three-phase becomes complex. In the dynamical model of IM using three-phase, some of the motor inductances are the functions of the rotor speed and as well as vary with time [33]. A three-phase to two-phase transformation is used to minimize the complexity associated with the three-phase differential equations. Clarke's transformation is used to convert a three-phase stationary machine into an equivalent two-phase stationary machine (orthogonal components). In this transformation αs and αr correspond to stator and rotor direct-axis components, whereas βs and βr correspond to the quadrature stator and rotor components. However, the parameters are still time-variant. R. H. Park in 1920s has given a transformation approach for electric machine to solve the above mentioned problem. In his formulation, variables which are linked with stator side are transformed to a rotating frame as fixed with the rotor. Using this proposed transformation, all time-dependent inductances corresponding to electric circuits in relative motion and with varying magnetic reluctance are eliminated [33]. For the rotor side, all the variables appear as of constant values.

2.2.2 Axes Transformation

The three-phase variables can be transformed into stationary reference frame using Clarke's transformation. The Clarke's transformed quantities are represented by α and β components, respectively. Both components are orthogonal to each other and in the steady state have the sinusoidal form.

The criterion to transform three-phase stationary frame to two-phase stationary frame and two-phase stationary to two-phase synchronous frame is shown in Fig. 2.2. The synchronous frame is rotating with speed ω_e in the stationary reference frame. The relative speed between the rotor (position angle θ_r) and the synchronous reference frame (position angle θ_e) is $\omega_{sl} =$

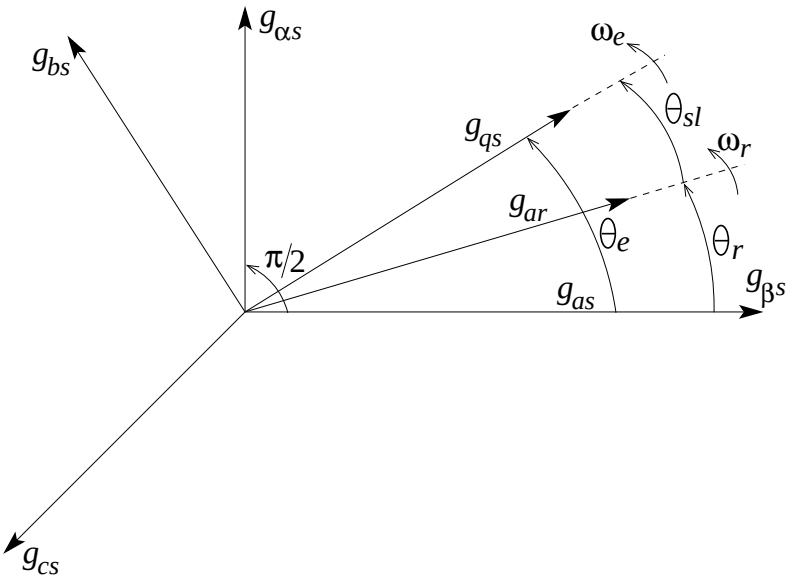

Figure 2.2: Three-phase to two-phase transformation.

$\omega_e - \omega_r$. The transformation corresponding to Clarke's as shown in Fig. 2.2 is given as:

$$\mathbf{g}_{\beta\alpha 0} = \mathbf{Z}_{\beta\alpha}\mathbf{g}_{abc} \tag{2.4}$$

where $(\mathbf{g}_{\beta\alpha 0})^T = \begin{bmatrix} g_\beta & g_\alpha & g_0, \end{bmatrix}$, $(\mathbf{g}_{abc})^T = \begin{bmatrix} g_a & g_b & g_c \end{bmatrix}$, $\mathbf{Z}_{\beta\alpha} = \frac{2}{3}\begin{bmatrix} 1 & -\frac{1}{2} & -\frac{1}{2} \\ 0 & \frac{\sqrt{3}}{2} & -\frac{\sqrt{3}}{2} \\ \frac{1}{2} & \frac{1}{2} & \frac{1}{2} \end{bmatrix}$. Here, g can be any variable among voltage, current, flux linkage and electric charge. The term $\frac{2}{3}$ indicates the per phase power invariant form.

Note that, the zero variables are not associated with the stationary reference frame. These are added to ensure reversibility of the transformed variables.

For the inverse of the Clarke's transformation, one can use

$$(\mathbf{Z}_{\beta\alpha})^{-1} = \begin{bmatrix} 1 & 0 & 1 \\ -\frac{1}{2} & \frac{\sqrt{3}}{2} & 1 \\ -\frac{1}{2} & -\frac{\sqrt{3}}{2} & 1 \end{bmatrix} \tag{2.5}$$

The Park's transformation introduces a new analysis which eliminates all the dynamical inductances (Varying with time) from the three-phase IM voltage equations. It is caused by transformations of all stationary framed quantities to synchronous reference frame corresponding to Fig. 2.2. The Park's transformed quantities are represented by d (direct) and q (quadrature) components, respectively. Park's transformation is given as:

$$\mathbf{g}_{qd0} = \mathbf{Z}_{qd}\mathbf{g}_{abc} \tag{2.6}$$

where

$$(\mathbf{g}_{qd0})^T = \begin{bmatrix} g_q & g_d & g_0 \end{bmatrix}, \ (\mathbf{g}_{abc})^T = \begin{bmatrix} g_a & g_b & g_c \end{bmatrix},$$
$$\mathbf{Z}_{qd} = \frac{2}{3} \begin{bmatrix} \cos(\theta_e) & \cos(\theta_e - \frac{2\pi}{3}) & \cos(\theta_e + \frac{2\pi}{3}) \\ \sin(\theta_e) & \sin(\theta_e - \frac{2\pi}{3}) & \sin(\theta_e + \frac{2\pi}{3}) \\ \frac{1}{2} & \frac{1}{2} & \frac{1}{2} \end{bmatrix}.$$

Here, θ_e represent the angular displacement for the rotating reference frame.

Similar to Clarke's transformation, the inverse of the Park's transformation can be determined using the following:

$$(\mathbf{Z}_{qd})^{-1} = \frac{2}{3} \begin{bmatrix} \cos(\theta_e) & \sin(\theta_e) & 1 \\ \cos(\theta_e - \frac{2\pi}{3}) & \sin(\theta_e - \frac{2\pi}{3}) & 1 \\ \cos(\theta_e + \frac{2\pi}{3}) & \sin(\theta_e + \frac{2\pi}{3}) & 1 \end{bmatrix} \tag{2.7}$$

Park's transformation is usually made first by transforming the three-phase quantities through Clarke's transformation and then one rotation. The following equations shows the relation between Park and Clarke transformation:

$$\begin{bmatrix} g_\beta \\ g_\alpha \end{bmatrix} = \frac{2}{3} \begin{bmatrix} \cos(\theta_e) & -\sin(\theta_e) \\ \sin(\theta_e) & \cos(\theta_e) \end{bmatrix} \begin{bmatrix} g_q \\ g_d \end{bmatrix} \tag{2.8}$$

and

$$\begin{bmatrix} g_q \\ g_d \end{bmatrix} = \frac{2}{3} \begin{bmatrix} \cos(\theta_e) & \sin(\theta_e) \\ -\sin(\theta_e) & \cos(\theta_e) \end{bmatrix} \begin{bmatrix} g_\beta \\ g_\alpha \end{bmatrix} \tag{2.9}$$

2.2.3 Stationary Reference Frame Model

The three-phase IM model equations (2.2) and (2.3) with flux linkage expressions from [33] are transformed into the stationary reference frame using (2.4). The transformed equations are written as

$$\left.\begin{aligned} v_{\alpha s} &= R_s i_{\alpha s} + \frac{d\psi_{\alpha s}}{dt} \\ v_{\beta s} &= R_s i_{\beta s} + \frac{d\psi_{\beta s}}{dt} \\ 0 &= R_r i_{\alpha r} + \frac{d\psi_{\alpha r}}{dt} - \omega_r \psi_{\beta r} \\ 0 &= R_r i_{\beta r} + \frac{d\psi_{\beta r}}{dt} + \omega_r \psi_{\alpha r} \end{aligned}\right\} \tag{2.10}$$

along with

$$\left.\begin{aligned} \psi_{\alpha s} &= L_{ls} i_{\alpha s} + L_m i_{\alpha m} \\ \psi_{\beta s} &= L_{ls} i_{\beta s} + L_m i_{\beta m} \\ \psi_{\alpha r} &= L_{lr} i_{\alpha r} + L_m i_{\alpha m} \\ \psi_{\beta r} &= L_{lr} i_{\beta r} + L_m i_{\beta m} \end{aligned}\right\} \tag{2.11}$$

where $i_{\alpha m} = i_{\alpha s} + i_{\alpha r}$ and $i_{\beta m} = i_{\beta s} + i_{\beta r}$.

The equivalent circuit diagram for the stationary reference frame IM model is shown in Fig. 2.3 and Fig. 2.4.

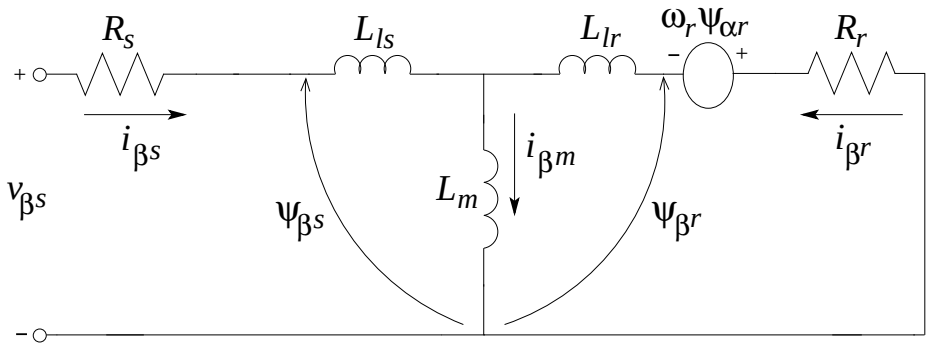

Figure 2.3: β equivalent IM model for stationary reference frame.

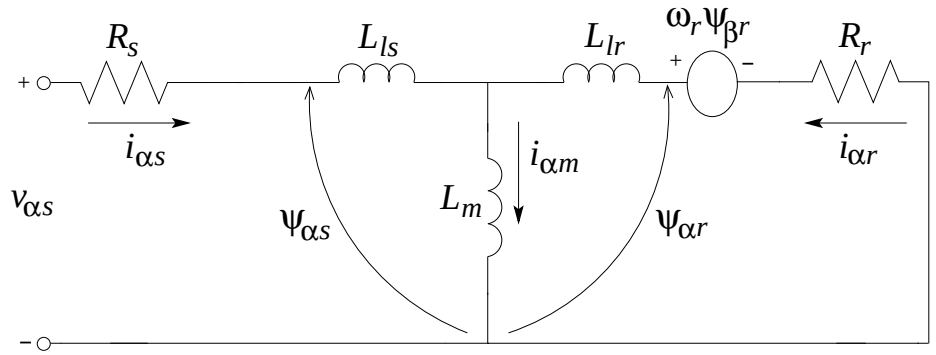

Figure 2.4: α equivalent IM model for stationary reference frame.

The above IM model (2.10)-(2.11) is comprised of stator currents, rotor fluxes and rotor currents. Practically, rotor currents are difficult to measure. These currents can be estimated from the rotor fluxes. Whereas rotor fluxes can be easily expressed in terms of stator currents using (2.11). Hence by solving (2.10)-(2.11) in terms of stator currents and rotor fluxes, the IM model in stationary reference frame is obtained as

$$\begin{bmatrix} si_{\alpha s} \\ si_{\beta s} \\ s\psi_{\alpha r} \\ s\psi_{\beta r} \end{bmatrix} = \begin{bmatrix} -a & 0 & b\sigma & b\omega_r \\ 0 & -a & -b\omega_r & b\sigma \\ \sigma L_m & 0 & -\sigma & -\omega_r \\ 0 & \sigma L_m & \omega_r & -\sigma \end{bmatrix} + \begin{bmatrix} c & 0 \\ 0 & c \\ 0 & 0 \\ 0 & 0 \end{bmatrix} \begin{bmatrix} v_{\alpha s} \\ v_{\beta s} \end{bmatrix} \tag{2.12}$$

where

$$L_s = L_{ls} + L_m,\ \ L_r = L_{lr} + L_m,\ \ a = \frac{R_s L_r}{L_r L_s - L_m^2} + \frac{L_m^2 R_r}{(L_r L_s - L_m^2) L_r},$$
$$b = \frac{L_m}{L_r L_s - L_m^2},\ \ c = \frac{L_r}{L_r L_s - L_m^2} \text{ and } \sigma = \frac{R_r}{L_r}.$$

Here σ represents the inverse of the rotor time constant and s denotes the Laplace operator.

2.2.4 Synchronous Reference Frame Model

The IM model (2.2) and (2.3) is converted into synchronously rotating reference frame using (2.6) as

$$\left.\begin{aligned} v_{ds} &= R_s i_{ds} + \frac{d\psi_{ds}}{dt} - \omega_e \psi_{qs} \\ v_{qs} &= R_s i_{qs} + \frac{d\psi_{qs}}{dt} + \omega_e \psi_{ds} \\ 0 &= R_r i_{dr} + \frac{d\psi_{dr}}{dt} - \omega_{sl} \psi_{qr} \\ 0 &= R_r i_{qr} + \frac{d\psi_{qr}}{dt} + \omega_{sl} \psi_{dr} \end{aligned}\right\} \tag{2.13}$$

and

$$\left.\begin{aligned} \psi_{ds} &= L_{ls} i_{ds} + L_m i_{dm} \\ \psi_{qs} &= L_{ls} i_{qs} + L_m i_{qm} \\ \psi_{dr} &= L_{lr} i_{dr} + L_m i_{dm} \\ \psi_{qr} &= L_{lr} i_{qr} + L_m i_{qm} \end{aligned}\right\} \tag{2.14}$$

where $i_{dm} = i_{ds} + i_{dr}$ and $i_{qm} = i_{qs} + i_{qr}$.

The equivalent circuit diagram for the synchronous rotating reference frame IM model is shown in Fig. 2.5 and Fig. 2.6.

Similar to the stationary reference frame model (2.12), the IM model with stator currents and rotor fluxes is expressed in rotating reference frame as

$$\begin{bmatrix} s i_{ds} \\ s i_{qs} \\ s\psi_{dr} \\ s\psi_{qr} \end{bmatrix} = \begin{bmatrix} -a & \omega_e & b\sigma & b\omega_r \\ -\omega_e & -a & -b\omega_r & b\sigma \\ \sigma L_m & 0 & -\sigma & \omega_e - \omega_r \\ 0 & \sigma L_m & \omega_r - \omega_e & -\sigma \end{bmatrix} + \begin{bmatrix} c & 0 \\ 0 & c \\ 0 & 0 \\ 0 & 0 \end{bmatrix} \begin{bmatrix} v_{ds} \\ v_{qs} \end{bmatrix} \tag{2.15}$$

The electromagnetic torque expression for the IM in d-q frame is given by [5, 6, 33]

$$T_e = \frac{3PL_m}{4L_r} \left(i_{qs}\psi_{dr} - i_{ds}\psi_{qr} \right) \tag{2.16}$$

The expression for the speed computation of the rotor is given by

$$J\frac{d\omega_m}{dt} = T_e - T_L \tag{2.17}$$

where ω_m represents the mechanical speed of the motor.

The relation between electrical speed ω_r and mechanical speed ω_m of the motor is given by

$$\omega_r = \frac{p}{2}\omega_m. \tag{2.18}$$

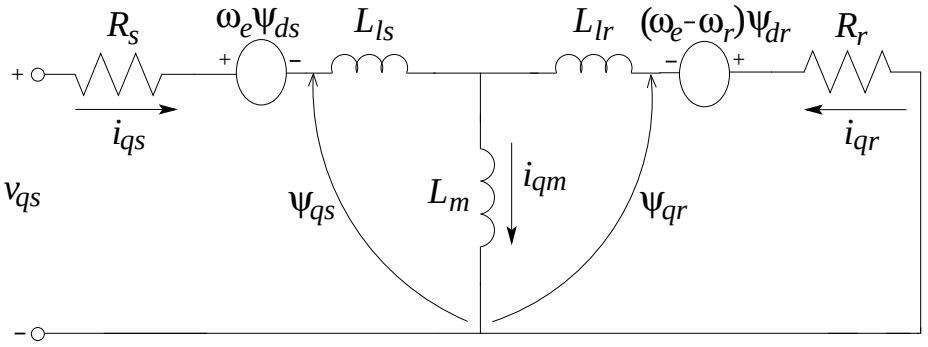

Figure 2.5: q equivalent IM model for synchronous reference frame.

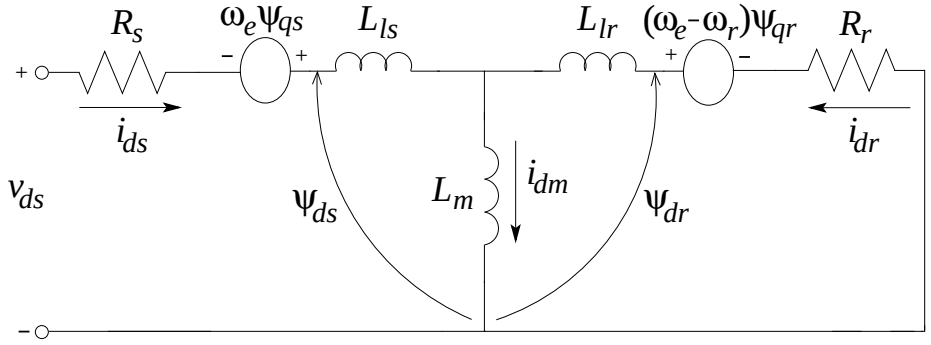

Figure 2.6: d equivalent IM model for synchronous reference frame.

Due to the presence of viscous friction, the motor speed is modified as

$$J\frac{d\omega_r}{dt} = K_m(T_e - T_L) - B_m\omega_r \tag{2.19}$$

where B_m represents the viscous friction coefficient.

The IM model combined with speed dynamics is obtained as

$$\left.\begin{aligned}
\frac{di_{ds}}{dt} &= -ai_{ds} + \omega_e i_{qs} + b\sigma\psi_{dr} + b\omega_r\psi_{qr} + cv_{ds} \\
\frac{di_{qs}}{dt} &= -\omega_e i_{ds} - ai_{qs} - b\omega_r\psi_{dr} + b\sigma\psi_{qr} + cv_{qs} \\
\frac{d\psi_{dr}}{dt} &= \sigma L_m i_{ds} - \sigma\psi_{dr} + (\omega_e - \omega_r)\,\psi_{qr} \\
\frac{d\psi_{qr}}{dt} &= \sigma L_m i_{qs} - (\omega_e - \omega_r)\psi_{dr} - \sigma\psi_{qr} \\
J\frac{d\omega_r}{dt} &= K_m(T_e - T_L) - B_m\omega_r
\end{aligned}\right\} \tag{2.20}$$

where

$$T_e = K_t(i_{qs}\psi_{dr} - i_{ds}\psi_{qr}),\quad K_t = \frac{3PL_m}{4L_r} \text{ and } K_m = \frac{P}{2}.$$

Next, the different control schemes V/f or scalar control, vector control, direct torque control

of IM as required for various industrial applications are reviewed.

2.3 Control Techniques for Induction Motor

The IM can be controlled by scalar or V/f control [34–39], vector control [6, 40–49], and direct torque control [50–55] which devise the performance of the drive system. V/f control is a conventional control scheme, which produces minimum steady state error for the IM drive. However, its torque response is sluggish. Vector control provides precise and fast torque control and a better alternative of V/f control (scalar control). Vector controlled induction motor (VCIM) drives are widely used in industries where reliability and high performance are the main concerns [5, 33]. On the other hand, the DTC is an advanced version of vector control. It is a sensorless control (does not require speed feedback information). The torque of IM is controlled directly rather than indirect manner as in vector control.

2.3.1 Volts/Hz or V/f Control

The motors powered with 50 Hz supply are operated at constant speed applications. V/f control is used to maintain the motor speed as constant. Its principle is based on maintaining the constant stator flux. This control technique is derived by applying steady state condition on (2.13) as

$$v_s = R_s i_s + \omega_e \psi_s \tag{2.21}$$

where ψ_s is the stator flux, v_s and i_s is either direct or quadrature component of respective stator voltage and stator current. If the stator resistance voltage drop is neglected for high motor speed, the above (2.21) can be written as:

$$\psi_s = \frac{v_s}{\omega_e} \tag{2.22}$$

From (2.22), it is depicted that for any speed variations one requires to change the stator voltage to maintain the constant flux $\psi_s = v_s/\omega_e$. The V/f control scheme block diagram is given in Fig. 2.7.

The motor is powered from a rectifier, and a three-phase inverter. The control action works without any feedback input. The reference quantity $\omega_{eref} \simeq \omega_r$ where slip speed ω_{sl} is considered as negligible. This ω_{eref} is further integrated to generate the position angle θ_e for the reference signals. The voltage signal v_s for three-phase command signal is obtained from ω_{eref} and a gain factor L. For making the controller suitability on low speed applications, a boost voltage v_0 is added. The effect of this boosting becomes negligible at higher ω_{eref}. This arrangement makes the flux ψ_s as constant. Besides the simplicity of V/f control implementation, it has certain disadvantages. In V/f control, when T_L is changed, ω_r is also changed by some amount. Hence, it is difficult to achieve precise speed control.

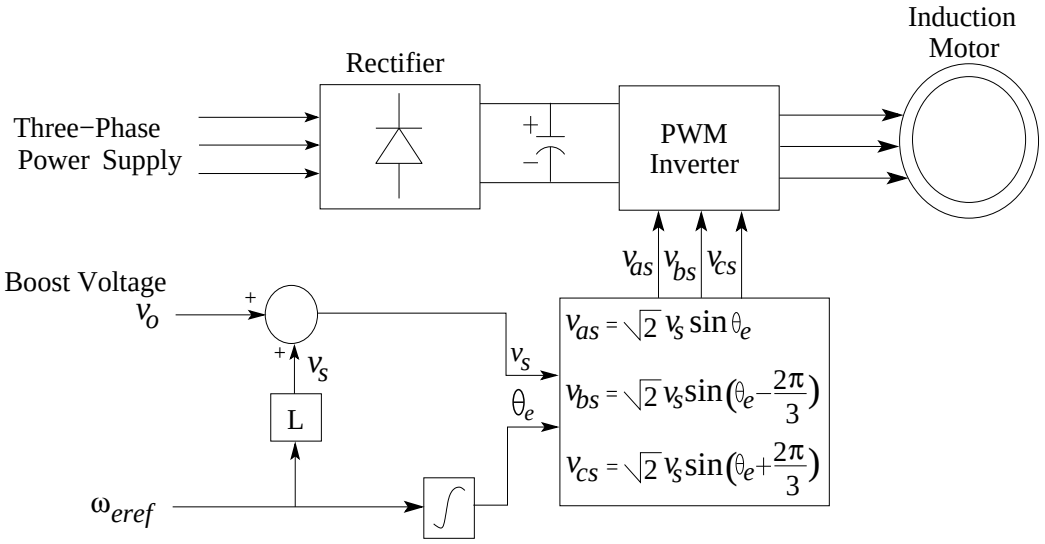

Figure 2.7: V/f Control scheme for IM.

This limit may be suitable for the applications like fan and pump drives. Moreover, when ω_{eref} is varied in a large step, the drive may become unstable.

2.3.2 Vector Control

Although the V/f control strategy for the IM is easy to implement, it makes the torque response sluggish. In V/f control strategy, a coupling exists between torque and flux response. As a consequence, if slip is increased to increase the torque, the flux is reduced. Even though if a flux controller loop is applied for compensating this reduction, the sensitivity of torque response is reduced. Hence response of motor is slowed down to any change in reference frequency. To overcome the above problem, in early of 1970's, a vector control strategy has been invented [6]. In this control technique, an IM is controlled analogously to a dc motor. This strategy is explained in Fig. 2.8.

The torque response of a separately excited dc motor is given by

$$T_{dc} = K_f I_f I_a \tag{2.23}$$

where K_f is a constant term, I_f is the field component of current and I_a is the torque component of current.

In a dc motor, both components of current produce orthogonal flux components. Hence, any change in field current does not affect torque current and vice versa. Due to this inherent decoupling, the dc motor produces a fast transient response. In the vector control, stator current i_{ds} behaves as dc motor field current I_f, whereas i_{qs} works similar to torque current I_a. This decoupling control can be achieved if i_{ds} is oriented in the direction of rotor flux $\hat{\psi}_r = \psi_{dr}$ ($\psi_{qr} = 0$) and i_{qs} is orthogonal to i_{ds} as shown in Fig. 2.9. As a consequence, when flux is controlled using i_{dsref}, it affects i_{ds} only. On the other hand, when i_{qsref}

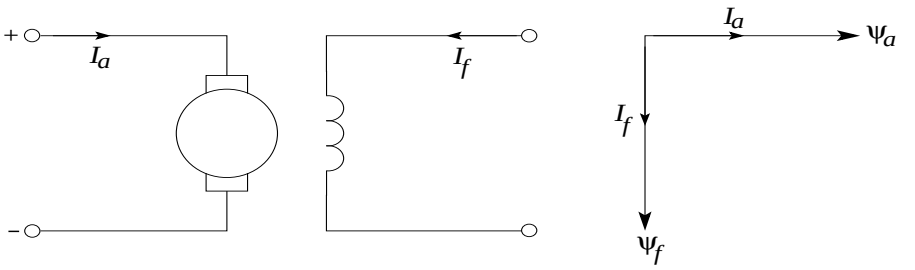

(a) Current vectors in dc motor

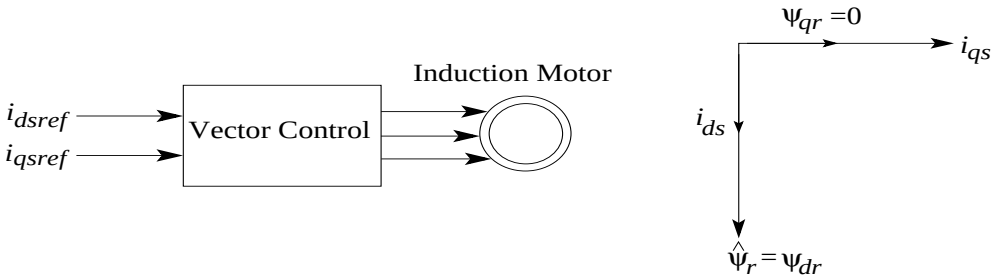

(b) Current vectors in vector controlled induction motor

Figure 2.8: Current vectors in dc motor and IM.

is changed, it affects i_{qs} only. Here i_{dsref} and i_{qsref} are the flux and torque reference current components. In general, implementation of vector control scheme requires speed information which is either estimated [56–59] or measured by an encoder [60, 61], stator currents, motor parameters and rotor flux position (θ_e). The rotor flux position information is utilized to generate the rotating reference unit vectors for the flux and torque component of current such that IM behaves similarly to a dc motor.

Vector control of IM is implemented by two methods direct [28, 62–69] and indirect [70–78]. Both the strategies are distinguished by the procedure of generating the angle or unit vectors ($\cos(\theta_e)$, $\sin(\theta_e)$) as required for alignment of i_{ds} and i_{qs} orthogonal to each other. Indirect vector control is preferred over direct one because (i) fewer number of transducers

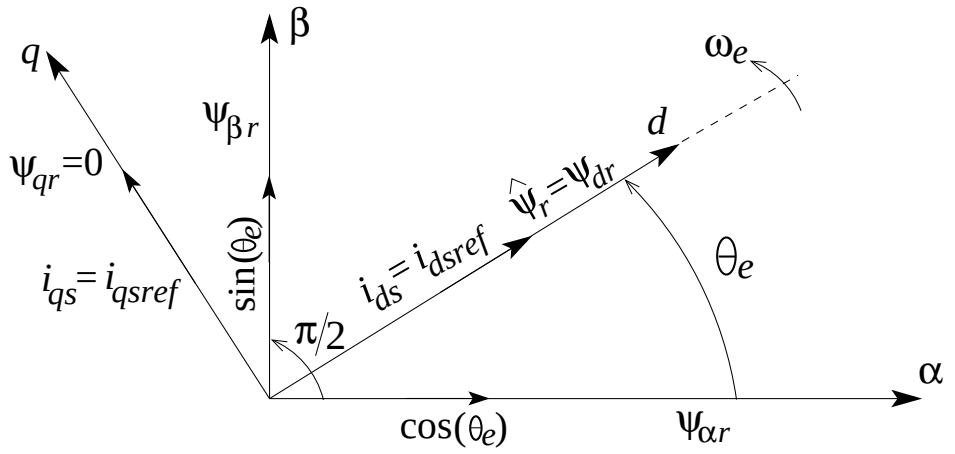

Figure 2.9: Principle of vector control technique.

and feedback loops are required, (ii) it is possible to operate the motor near zero-speed and (iii) better torque performance [7, 79].

Direct Vector Control

The rotor flux oriented direct vector control strategy is shown in Fig. 2.10. The reference flux ψ_{drref} is compared with the estimated rotor flux $\hat{\psi}_r$ and fed to the PI controller. The output of this controller (i_{dsref}) is subtracted from the flux component of current i_{ds}. The torque reference current i_{qsref} as obtained from the output of the speed-loop PI controller is subtracted from the torque component of current i_{qs}. The corresponding error signals are fed to the respective PI controllers, which yields direct and quadrature stator voltage components v_{ds} and v_{qs}, respectively. These voltages are further converted into three-phase stationary frame using rotor position θ_e as obtained from estimated $\psi_{\alpha r}$ and $\psi_{\beta r}$. These rotor fluxes are estimated from the mathematical model using stator currents $i_{\alpha s}$, $i_{\beta s}$ and/or stator voltages $v_{\alpha s}$, $v_{\beta s}$, and motor speed ω_r.

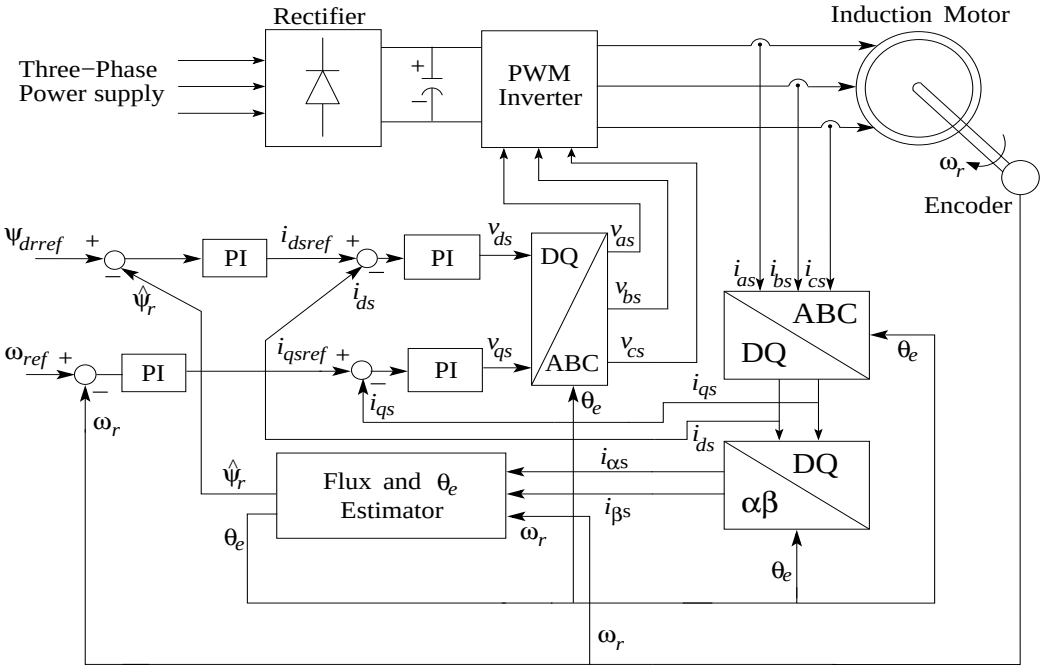

Figure 2.10: Direct vector control of IM.

In general, two techniques are used to estimate $\psi_{\alpha r}$ and $\psi_{\beta r}$, one is called as voltage model and the other one is termed as the current model. In the voltage model based flux estimation techniques, rotor fluxes are estimated from $v_{\alpha s}$ and $v_{\beta s}$ as obtained from (2.10) and (2.11). However, this method has limitations to be used at low speed and is affected by variation in R_s due to temperature. At low speed, the voltage drop across the stator resistance dominates the voltage signals $v_{\alpha s}$ and $v_{\beta s}$ and hence flux estimation is affected. On the other hand, in the current model based estimation the rotor fluxes are estimated directly from (2.10) and (2.11) in terms of i_{ds} and ω_r. This current model is suitable for high as well as at low

speed of the motor. The unit vectors and rotor flux can be written as

$$cos(\theta_e) = \frac{\psi_{\alpha r}}{\hat{\psi}_r}, \;\; sin(\theta_e) = \frac{\psi_{\beta r}}{\hat{\psi}_r} \text{ and } \hat{\psi}_r = \sqrt{(}\psi_{\alpha r}^2 + \psi_{\alpha r}^2) \tag{2.24}$$

When (2.24) is used for vector rotation, the synchronous frame flux components becomes $\psi_{dr} = \hat{\psi}_r$ and $\psi_{qr} = 0$. The corresponding torque expression (2.21) becomes

$$T_e = K_t i_{qs} \psi_{dr} \tag{2.25}$$

Note that, the above torque expression (2.25) is in agreement with the dc motor torque response (2.23). Hence using vector control technique an IM can be controlled similar to a dc motor.

Indirect Vector Control

The indirect vector control (IVC) scheme principle differs from the direct one in the sense of unit vectors generations. The unit vectors ($\cos(\theta_e)$, $\sin(\theta_e)$) are generated in feedforward fashion. The IVC scheme is shown in Fig. 2.11 where $\gamma = \frac{1}{\sigma}$, T_{re} is the torque reference as the output of the outer speed-loop PI controller. In IVC scheme, flux estimation is not required and it provides inherent decoupling rather than direct one. However, the rotor resistance variation may cause detuning of IVC scheme and leads to bifurcations if avoidance schemes (e.g., proper tuning of PI gains, stable limit for rotor resistance variation) are not applied.

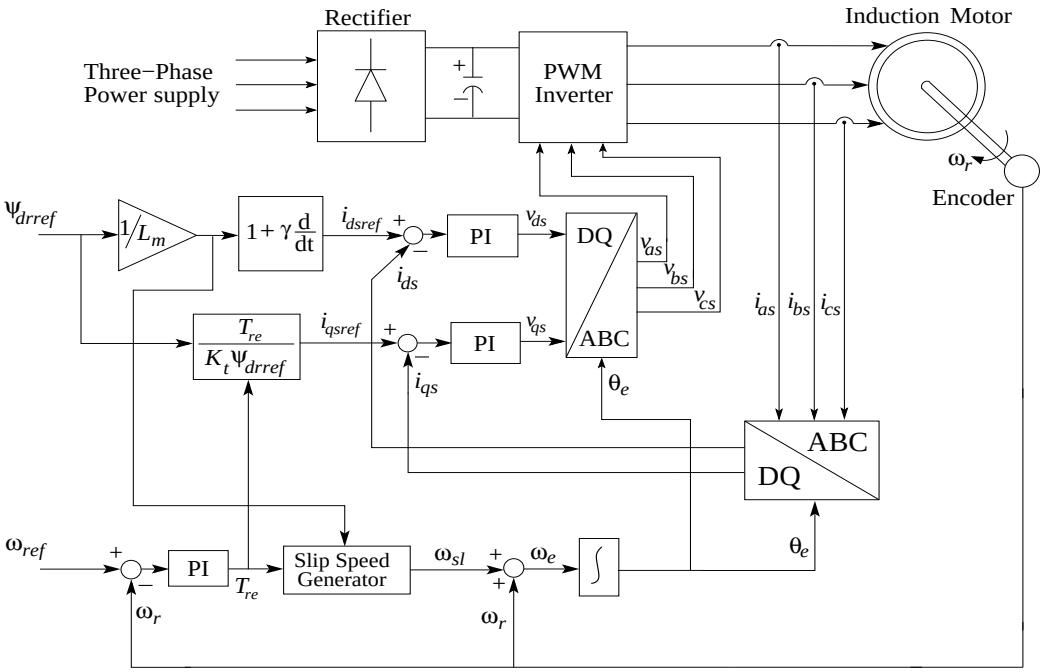

Figure 2.11: Indirect vector control of IM.

The rotor pole position is determined as

$$\theta_e = \int(\omega_e)dt = \int(\omega_r + \omega_{sl})dt \tag{2.26}$$

where $\omega_{sl} = \frac{\sigma L_m T_{re}}{K_t \psi^2_{drref}}$ and $\theta_{sl} = \int(\omega_{sl})dt$ is the slip angle between the synchronously rotating reference frame and the rotor reference frame. The angle between stator reference frame and rotor reference frame is $\theta_r = \int(\omega_r)dt$.

The independent control of motor using IVC approach is derived in the following way. From (2.20), the rotor flux equation in synchronously rotating reference frame is written as

$$\begin{aligned} \frac{d\psi_{dr}}{dt} =& \sigma L_m i_{ds} - \sigma\psi_{dr} + (\omega_e - \omega_r)\,\psi_{qr} \\ \frac{d\psi_{qr}}{dt} =& \sigma L_m i_{qs} - (\omega_e - \omega_r)\psi_{dr} - \sigma\psi_{qr}. \end{aligned} \tag{2.27}$$

For the independent control, it is desired that

$$\psi_{dr} = \hat{\psi}_r \text{ and } \psi_{qr} = 0. \tag{2.28}$$

Substituting (2.28) into (2.27), one gets the following equations which governs the IVC operation

$$\psi_r = \psi_{dr} = L_m i_{ds} \text{ and } \omega_{sl} = \frac{\sigma i_{qs}}{i_{ds}}. \tag{2.29}$$

The corresponding torque equation is similar to (2.25).

2.3.3 Direct Torque Control

After the vector control technique, in the mid 1980's, a new control technique was developed for the voltage-fed pulse width modulation (PWM) drives. This technique is termed as direct torque and flux control (DTFC) or direct self-Control (DSC) [80, 81]. This control technique provides faster torque response as compared to the scalar and the vector control strategies.

Fig. 2.12 shows the principle of DTC technique. The reference stator flux $\hat{\psi}_{sref}$ and torque command T_{ref} are compared with the estimated values and the corresponding error signals are applied to hysteresis controllers. The hysteresis controller for the flux errors gives two level digital output as:

$$\left.\begin{aligned} H_{s\psi} =& 1, \quad \text{if } e_\psi > H_{sb\psi}, \\ H_{s\psi} =& -1, \quad \text{if } e_\psi < -H_{sb\psi} \end{aligned}\right\} \tag{2.30}$$

where $H_{sb\psi}$=hysteresis bandwidth. The estimated flux $\hat{\psi}_s$ follows the command flux $\hat{\psi}_{sref}$ in a zigzag path due to hysteresis band. On the other hand the torque control loop has three

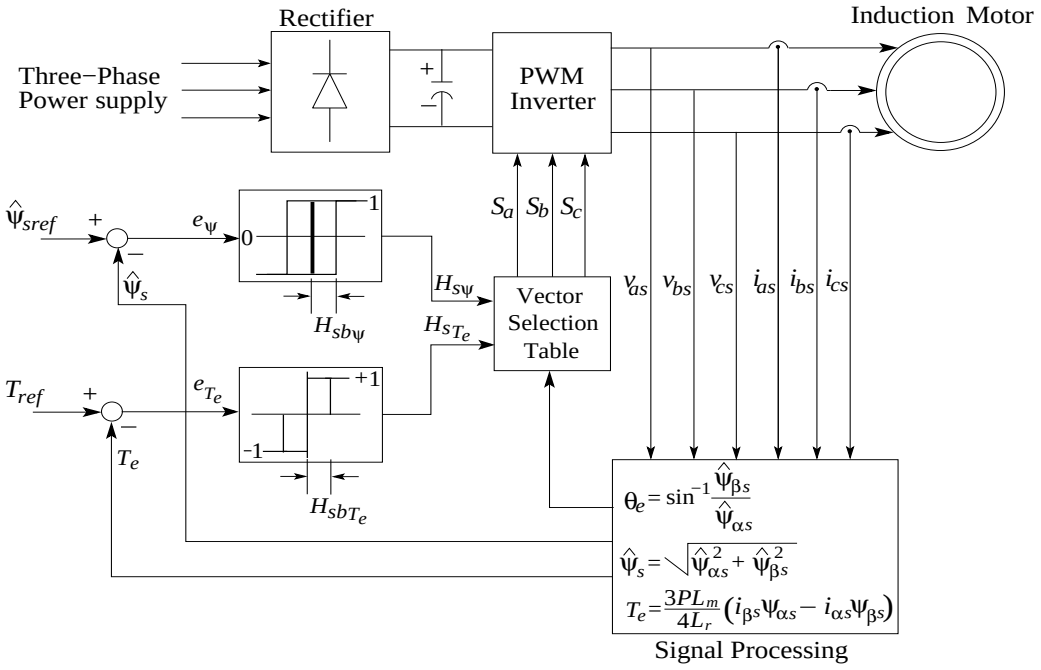

Figure 2.12: Direct torque control of IM.

level digital output as:

$$\left.\begin{aligned} H_{sT_e} &= 1, && \text{if } e_{T_e} > H_{sbT_e}, \\ H_{sT_e} &= -1, && \text{if } e_{T_e} < -H_{sbT_e}, \\ H_{sT_e} &= 0, && \text{if } -H_{sbT_e} < e_{T_e} < +H_{sbT_e}. \end{aligned}\right\} \tag{2.31}$$

The stator flux and angle information are estimated using (2.10). The corresponding sector is determined from this angle in which stator flux ψ_s resides. On the basis of hysteresis controller output and sector information, a suitable voltage vector is chosen from a look-up table [6]. This voltage vector is given to the inverter which generates the corresponding power signals to control the motor. Since both feedback signals (flux and torque) are estimated from stator currents and voltage signals, hence DTC represents inherent sensorless control.

2.4 Control Techniques Comparison

The V/f control for IM is a simple and low cost technique as it does not require any feedback. This control technique has the following limitations:

- It is limited for low precision control applications like pumps and fans.
- It is not an automatic feedback control. Whenever load is changed, one has to adjust the voltage correspondingly, hence motor response is delayed.
- The torque response of the motor is coupled with the flux of the motor and hence

gives sluggish response. The controlled torque response can not be achieved from V/f control technique.

As compared to the V/f control, the vector control technique for IM is a closed-loop control and it controls the IM similar to a dc motor. The torque response of the IM using this control is decoupled inherently and it is controlled in an indirect manner. It provides a precision control and has applications in distributed paper-making machines, rolling mills, manufacturing assembly, hybrid electric vehicle. The vector control technique has the underneath limitations:

- It is a feedback control hence it is costly as compared to the V/f control.
- The parameter variation affect the IM control.
- The PI tuning of three controllers is a tedious task.

As compared to the vector control, the DTC control is less complex. It does not requires speed information and provides a faster torque response. However, it has following limitations:

- Starting of the motor using DTC is difficult as at low speed, estimation errors in stator resistance dominates stator voltages.
- For precise torque control, current sensors must be of high quality and hence cost is increased as compare to the vector control.
- The torque and flux responses using DTC are not smooth, ripples are higher as compare to the vector control.

2.5 IM Controller Under Study

Vector control technique for IM yields decoupled torque response than the V/f control. It is a cheaper scheme compared to the DTC one, which requires accurate current sensors that are costly. The IVC is more popular than the direct one owing to high performance and simplicity in the design. In this thesis, stability analysis and controller design are carried out for IVCIM considering synchronous reference frame IM model (2.20), as will be shown later.

2.6 Chapter Summary

In this chapter, reference frame theory and IM modeling have been discussed. Further, different control techniques V/f, vector and direct torque schemes have been presented. The limitations of these control schemes have been addressed. Although DTC scheme is an

advanced technique of controlling IM, IVC is preferred in industries due to cost effectiveness and smoother torque response. In the next chapter, the rotor resistance variation effect on IVCIM is studied in detail to avoid detuning and bifurcation phenomenon.

Chapter 3

A Numerical Bifurcation Analysis of IVCIM

3.1 Introduction

IVCIM [1, 2, 6, 56, 57] is widely used in industries for its high torque performance. The parameters of an IM may vary with temperature [7], aging, estimation error (due to malfunctioning of assessment algorithms [11, 12]) and other environmental reasons. The IVCIM dynamics is sensitive to variations in the motor parameters, such as rotor resistance, stator resistance, mutual inductance, inertia and mechanical load torque. Such variations may deteriorate steady-state as well as the dynamic performance of the drive system and may induce bifurcations [9, 82] in the motor dynamics that leads to large stator current, stalling or even permanent damage of the motor. Accurate prediction of such bifurcations can be utilized for (i) assessing the stability and robustness, (ii) obtaining the limiting control gains while tuning [13], (iii) protection against limiting variations in rotor resistance and its estimation [9], (iv) avoiding comparatively dangerous bifurcations [83], (v) synthesis of efficient controllers for different applications [84].

The effect of rotor resistance variation on the stability of IVCIM has been reported in [8]. In this work, it is shown that the IVCIM drive is globally asymptotically stable for any given constant load torque if the rotor resistance is ideally known or the variation is small enough. The outer speed-loop design rule is also obtained to ensure local asymptotic stability for any value of the rotor resistance. An offline tuning process for the speed-loop is developed in [85] to ensure global stability for maximum variation in the rotor resistance. In [9], a SNB is observed due to mismatch in rotor resistance under certain load conditions. The occurrence of such bifurcation is found to be independent of outer speed-loop proportional-integral (PI) gains. On the contrary, the occurrence of HB [13, 14], codimension-two BTB and ZHB [15] are found to be dependent on the speed-loop control gains and loading condition. In [15], a computational tool AUTO has been used to study BTB and ZHB.

However, these studies [8, 9, 13–15] are mainly based on lower-order IM model neglecting the stator current dynamics and less comprehensive for the loading condition. For example, in [14], the rotor resistance estimation error seems to improve the stability of

IVCIM system in presence of load. Such negligence may affect the bifurcation points and its behavior. It also appears that prediction and avoidance method of HB at loading condition has not been investigated so far.

In this chapter, a bifurcation study on PI controlled IVCIM is carried out by using a full-order IM model that fills the gaps mentioned above. A general IVCIM (considering variable reference current dynamics) [5, 16, 17] is considered for the purpose. Bifurcation conditions of IVCIM are determined based on linearized model around the equilibrium point. Experimental validation of HB with loading condition is also presented. Owing to detailed analysis using a higher-order model, the following new observations are made: (i) Computing bifurcation points is iterative since the equilibrium point depends on the bifurcation parameter. (ii) SNB may happen at underestimation of rotor resistance, (ii) HB is more prominent than the SNB at higher loading, (iii) Higher proportional and lower integral gain in the speed-loop leads to avoidance of HB and ZHB. The results can be effectively used for predicting bifurcation behavior and in setting limits on PI controller gains while tuning.

The structure of this chapter is organized as follows: Section 3.2 presents the general IVCIM model comprising of higher-order model (HOM), lower-order model (LOM) and linearization around the equilibrium point. Bifurcation analysis of SNB and HB, BTB and ZHB along with developed algorithm is provided in Section 3.3. Further, this bifurcation analysis is extended for Classical IVCIM system in Section 3.4. Simulation and experiment results are presented in Section 3.5 and Section 3.6, respectively. In the end, relevant conclusions are pointed out in Section 3.7.

3.2 General IVCIM

A general IVCIM drive system [5, 16, 17] for speed regulation, is shown in Fig. 3.1. The rotor speed is regulated by a PI speed control loop. The output of this controller is used to generate the reference torque and flux components of the current. These references are compared with the motor currents and applied to the current controllers that govern the input voltage of the IM.

3.2.1 Higher-Order Model (HOM)

Following the IVCIM system in Fig. 3.1, the slip speed is given by

$$\omega_{sl} = \alpha\sigma L_m T_{re} \text{ and } T_{re} = \left(K_{p\omega} + K_{i\omega}\int dt\right)(\omega_{ref} - \omega_r) \tag{3.1}$$

where $K_{p\omega}$ and $K_{i\omega}$ are the speed controller gains and $\alpha = \frac{\hat{\sigma}}{\sigma}$ is a measure of slip speed tuning (also called tuning gain) parameter for bifurcation. The perfect tuning is indicated by the matched condition $\alpha = 1$. In this work, variation in R_r is only considered assuming L_r

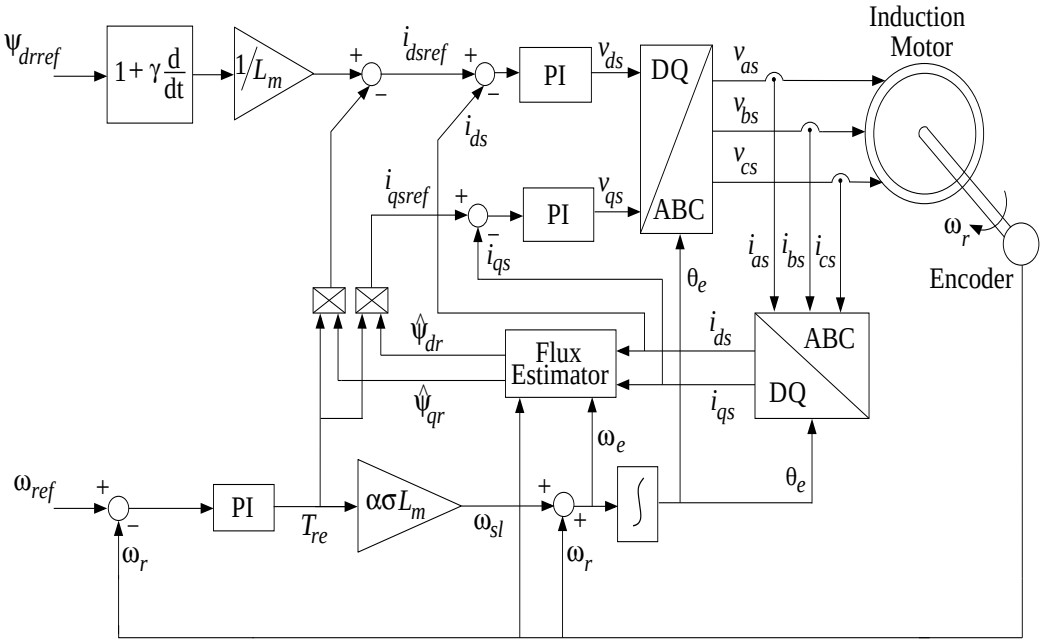

Figure 3.1: Indirect vector control of induction motor.

is constant, i.e., $\hat{\sigma} = \hat{R}_r/L_r$.

The stator reference current components can be written following Fig. 3.1 as:

$$i_{dsref} = \frac{\psi_{drref} + \gamma\dot{\psi}_{drref}}{L_m} - \psi_{qr}T_{re} \text{ and } i_{qsref} = \psi_{dr}T_{re} \tag{3.2}$$

where ψ_{drref} is the reference flux, ψ_{dr} and ψ_{qr} are the direct and quadrature components of the rotor fluxes. Note that, the rotor fluxes in (3.2) are actually the estimates (see Fig. 3.1), although the estimation error dynamics is neglected.

The stator voltages, following Fig. 3.1, can be written as

$$\left.\begin{aligned} v_{ds} &= \left(K_{pd} + K_{id}\int dt\right)(i_{dsref} - i_{ds}) \\ v_{qs} &= \left(K_{pq} + K_{iq}\int dt\right)(i_{qsref} - i_{qs}) \end{aligned}\right\} \tag{3.3}$$

where K_{pd} and K_{pq} are the proportional constants for the direct and quadrature current components, respectively; K_{id} and K_{iq} are the integral constants for the direct and quadrature components, respectively.

The full-order IM model [6, Page 65](2.20) is used here. The state variables of the IVCIM are defined as: $x_1 = i_{ds}$, $x_2 = i_{qs}$, $x_3 = \psi_{dr}$, $x_4 = \psi_{qr}$, $x_5 = (\omega_{ref} - \omega_r)$, $x_6 = \left(K_{p\omega} + K_{i\omega}\int dt\right)(\omega_{ref} - \omega_r)$, $x_7 = \int (i_{dsref} - i_{ds})dt$, $x_8 = \int (i_{qsref} - i_{qs})dt$, where i_{ds} and i_{qs} are the direct and quadrature components of the stator current. Following Fig. 3.1,

(3.1) and (3.2), the state-space model of the IVCIM system can be described as:

$$\begin{aligned}
\dot{x}_1 &= -ax_1 + [\omega_{ref} - x_5 + \alpha\sigma L_m x_6]x_2 + b\sigma x_3 + cK_{pd}\left(L_m^{-1}\psi_{drref}\right. \quad (3.4)\\
&\quad \left. + L_m^{-1}\gamma\dot{\psi}_{drref} - x_4x_6 - x_1\right) + b(\omega_{ref} - x_5)x_4 + cK_{id}x_7\\
\dot{x}_2 &= -[\omega_{ref} - x_5 + \alpha\sigma L_m x_6]x_1 - ax_2 - b(\omega_{ref} - x_5)x_3 + b\sigma x_4 \quad (3.5)\\
&\quad + cK_{pq}\left[x_3x_6 - x_2\right] + cK_{iq}x_8\\
\dot{x}_3 &= \sigma L_m x_1 - \sigma x_3 + \alpha\sigma L_m x_4x_6 \quad (3.6)\\
\dot{x}_4 &= \sigma L_m x_2 - \sigma x_4 - \alpha\sigma L_m x_3x_6 \quad (3.7)\\
J\dot{x}_5 &= -K_m\left[K_t(x_2x_3 - x_1x_4) - T_L\right] + B_m(\omega_{ref} - x_5) \quad (3.8)\\
J\dot{x}_6 &= -K_{p\omega}[K_m\left[K_t(x_2x_3 - x_1x_4) - T_L\right] - B_m(\omega_{ref} - x_5)] + JK_{i\omega}x_5 \quad (3.9)\\
\dot{x}_7 &= L_m^{-1}\psi_{drref} + L_m^{-1}\gamma\dot{\psi}_{drref} - x_4x_6 - x_1 \quad (3.10)\\
\dot{x}_8 &= x_3x_6 - x_2 \quad (3.11)
\end{aligned}$$

Note that, the model (3.4)-(3.11) additionally includes the stator current dynamics (i_{ds} and i_{qs}) as compared to the reported ones in [9, 13–15]. Hence, we will refer this as HOM.

3.2.2 Equilibrium Point

For linearization of the nonlinear dynamics (3.4)-(3.11), its equilibrium point is obtained next. Let, x_i^e, $i = 1, \cdots, 8$, indicate the values of the states at the equilibrium point. For determining the equilibrium point, the following assumptions are considered.

1. The reference flux ψ_{drref} is taken as constant.
2. At equilibrium ω_r reaches ω_{ref}, i.e. $x_5^e = 0$.
3. T_L is considered as constant.

Let us start with

$$x_5^e = 0. \quad (3.12)$$

Then, from (3.10)

$$x_6^e = \frac{1}{x_4^e}\left(\frac{\psi_{drref}}{L_m} - x_1^e\right). \quad (3.13)$$

Alternatively, from (3.11), one gets

$$x_6^e = \frac{x_2^e}{x_3^e}. \quad (3.14)$$

Then, from (3.6), one obtains

$$x_3^e = L_m x_1^e(1 - \alpha) + \alpha\psi_{drref}. \quad (3.15)$$

Now, using (3.12) and (3.14) in (3.7), one gets

$$x_4^e = L_m x_2^e(1 - \alpha). \quad (3.16)$$

Then using (3.12), (3.15) and (3.16) into (3.8), one obtains

$$x_2^e = \frac{B_m\omega_{ref} + K_m T_L}{\alpha K_m K_t \psi_{drref}}. \tag{3.17}$$

Further, from (3.13) and (3.14), one can write

$$\frac{1}{x_4^e}\left(\frac{\psi_{drref}}{L_m} - x_1^e\right) = \frac{x_2^e}{x_3^e}. \tag{3.18}$$

Now, by putting the values of x_3^e, x_4^e and x_2^e from (3.15), (3.16) and (3.17) in (3.18), one obtains the following relation:

$$\begin{aligned}&(1-\alpha)L_m^2(x_1^e)^2 - (1-2\alpha)L_m\psi_{drref}x_1^e - \alpha\psi_{drref}^2 \\ &+ \frac{(1-\alpha)L_m^2(B_m\omega_{ref} + K_m T_L)^2}{(\alpha K_m K_t \psi_{drref})^2} = 0.\end{aligned} \tag{3.19}$$

By following (3.12)-(3.19), x_7^e and x_8^e can also be determined from (3.4) and (3.5). If α is tuned (i.e., $\alpha = 1$), (3.19) yields a real solution for x_1^e as

$$x_1^e = \frac{\psi_{drref}}{L_m}. \tag{3.20}$$

Whereas if α is detuned (i.e., $\alpha \neq 1$), the equilibrium point is not unique. Then

$$x_1^e = \frac{-m \pm \sqrt{m^2 - 4ln}}{2l}, \tag{3.21}$$

with

$$\begin{aligned}l = (1-\alpha)L_m^2, \;\; m = -(1-2\alpha)L_m\psi_{drref}, \\ n = \frac{(1-\alpha)L_m^2(B_m\omega_{ref} + K_m T_L)^2}{(\alpha K_m K_t \psi_{drref})^2} - \alpha\psi_{drref}^2.\end{aligned} \tag{3.22}$$

Clearly, (3.21) has real solutions if, $m^2 - 4ln \geq 0$, which can be written as

$$\psi_{drref}^2 - 4\left(\frac{L_m(1-\alpha)(B_m\omega_{ref} + K_m T_L)}{\alpha K_m K_t \psi_{drref}}\right)^2 \geq 0. \tag{3.23}$$

Therefore, existence of real x_1^e can be expressed, following (3.23), as:

$$\begin{aligned}&\frac{2L_m(B_m\omega_{ref} + K_m T_L)}{2L_m(B_m\omega_{ref} + K_m T_L) + K_m K_t \psi_{drref}^2} \leq \alpha \\ &\leq \frac{2L_m(B_m\omega_{ref} + K_m T_L)}{2L_m(B_m\omega_{ref} + K_m T_L) - K_m K_t \psi_{drref}^2}.\end{aligned} \tag{3.24}$$

Here, (3.24) yields a range for the estimated rotor resistance so that equilibrium point exists. Also, the boundaries of this range provides the bifurcation points above and below the

Table 3.1: Comparison of equilibrium point

State equilibrium	Classical IVCIM [9, 13–15]			General IVCIM [5, 16, 17]		
	Relation with α	Stability haracteristic		Relation with α	Stability characteristic	
		α<1	α>1		α<1	α>1
x_1^e (i_{ds})	Constant	Constant	Constant	Quadratic	Becomes non-real after crossing a lower limit	Becomes non-real after crossing an upper limit
x_2^e (i_{qs})	Cubic	Similar to x_6^e	Similar to x_6^e	Nonlinear	Increases	Decreases
x_3^e (ψ_{dr})	Nonlinear	Increases	Decreases	Nonlinear	Decreases	Decreases
x_4^e (ψ_{qr})	Nonlinear	Increases	Increases	Nonlinear	Increases	Increases
x_5^e (ω_{ref}-ω_r)	Constant	Constant	Constant	Constant	Constant	Constant
x_6^e (T_{re})	Cubic	Decreases	Increases	Nonlinear	Existence depends on x_1^e	Existence depends on x_1^e

nominal value of $\alpha = 1$ as shown in Section 3.3 later.

Table 3.1 shows a comparison between equilibrium point of classical IVCIM [9, 13–15] and the general one. It can be seen that the equilibrium point (3.12)-(3.19) yields new features with respect to variation in α. Due to consideration of i_{ds}, i_{qs} and flux dynamics effect (3.2) on the reference currents, the behavioral shift in equilibrium point from those obtained in classical one is prominent as shown in Table 3.1. Therefore, the present equilibrium point for $\alpha \neq 1$ exhibits different behavior than the model corresponding to the models of classical IVCIM, e.g. in [9, 13–15].

3.2.3 Lower-Order Model (LOM)

Determining the characteristic equation corresponding to 8^{th} order HOM is complex. In the operating frequency range of the fast current-loop controllers (larger bandwidth), the effect of PI (having bi-proper transfer function) is same as the proportional one. Moreover, for considerable K_{pd} and K_{pq} gains (zero location moving towards the origin), the effect of integrator dynamics is small. Hence, the dynamics involving K_{id} and K_{iq} are neglected. Certain extents on the effect of these integrator dynamics are further elaborated through the comparison of HOM and LOM dynamics in Fig. 3.2(c) (Section 3.3) and nonlinear simulation results in Section 3.5. Note that, the LOM is having 6 states and still includes the stator currents (i_{ds} and i_{qs}) as its states.

3.2.4 Linearization

The linearization procedure is presented in Chapter A. The nonlinear IVCIM model is linearized at the equilibrium point as

$$\dot{x} = Gx \tag{3.25}$$

where $G = G_{LOM}$ or G_{HOM} represents the Jacobian matrix for the LOM or the HOM, as the case is. Further,

$$G_{HOM} = \begin{bmatrix} G_{LOM} & H_{12} \\ H_{21} & \mathbf{0}_{2\times 2} \end{bmatrix} \tag{3.26}$$

where $G_{LOM} = \begin{bmatrix} G_{Lo1} & G_{Lo2} \end{bmatrix}$. The corresponding matrices are given as

$$G_{Lo1} = \begin{bmatrix} -a - cK_{pd} & \omega_{ref} + \alpha\sigma L_m x_6^e & b\sigma \\ -(\omega_{ref} + \alpha\sigma L_m x_6^e) & -a - cK_{pq} & cK_{pq}x_6^e - b\omega_{ref} \\ \sigma L_m & 0 & -\sigma \\ 0 & \sigma L_m & -\alpha\sigma L_m x_6^e \\ \frac{K_m K_t x_4^e}{J} & -\frac{K_m K_t x_3^e}{J} & -\frac{K_m K_t x_2^e}{J} \\ \frac{K_{p\omega} K_m K_t x_4^e}{J} & -\frac{K_{p\omega} K_m K_t x_3^e}{J} & -\frac{K_{p\omega} K_m K_t x_2^e}{J} \end{bmatrix},$$

$$G_{Lo2} = \begin{bmatrix} b\omega_{ref} - cK_{pd}x_6^e & -x_2^e - bx_4^e & \alpha\sigma L_m x_2^e - cK_{pd}x_4^e \\ b\sigma & x_1^e + bx_3^e & cK_{pq}x_3^e - \alpha\sigma L_m x_1^e \\ \alpha\sigma L_m x_6^e & 0 & \alpha\sigma L_m x_4^e \\ -\sigma & 0 & -\alpha\sigma L_m x_3^e \\ \frac{K_m K_t x_1^e}{J} & -\frac{B_m}{J} & 0 \\ \frac{K_{p\omega} K_m K_t x_1^e}{J} & K_{i\omega} - \frac{K_{p\omega} B_m}{J} & 0 \end{bmatrix},$$

$$H_{12} = \begin{bmatrix} cK_{id} & 0 & 0 & 0 & 0 & 0 \\ 0 & cK_{iq} & 0 & 0 & 0 & 0 \end{bmatrix}^T, \quad H_{21} = \begin{bmatrix} -1 & 0 & 0 & -x_6^e & 0 & -x_4^e \\ 0 & -1 & x_6^e & 0 & 0 & x_3^e \end{bmatrix}.$$

Remark 1: In the above (particularly in (3.2)), the flux estimation error dynamics is neglected. This is a standard assumption in literature, e.g. see [5, 11, 16, 17, 86, 87]. Further, it may be noted that the error dynamics directly affect the i_{dsref} and i_{qsref} in (3.2) that can be modeled as perturbation to the nominal system. Since stability boundaries are of interest in the present study within which the system is exponentially stable, the above negligence only leads to quantitative change in the behavior [88, Chapter 9]. In addition, both the equilibrium point of the states (3.12)-(3.19) and the Jacobian matrix in (3.26) are independent of i_{dsref} and i_{qsref} that shows the behavioral aspects studied later is independent of the error dynamics. However, depending on the degree of stability, the error dynamics effect may vary [13].

Remark 2: The linearized model (3.25) depends on the external input T_L and hence its stability behavior as well. Although the analysis is carried out considering constant T_L ("frozen"parameter [88]), a time-varying T_L may lead to quantitative change in the stability behavior considering the same exponential stability of the system [13, 88].

3.3 Bifurcation Analysis of General IVCIM

The basic bifurcation concept and examples are shown in Chapter A. Bifurcation analysis of the general IVCIM in Fig. 3.1 is carried out through the characterization of the linearized model (3.25). In this regard, the difference between the behavior of HOM and LOM is also studied. The following bifurcation definitions adopted from [88–90] are used for the purpose.

Definition 1 *With variation in system parameter(s),*

1. *if a single real eigenvalue crosses the imaginary axis then SNB occurs.*
2. *if a pair of complex eigenvalues crosses the imaginary axis satisfying transversality condition then HB occurs.*
3. *if two real eigenvalues simultaneously cross the imaginary axis then BTB occurs.*
4. *if a pair of complex eigenvalues along with a real one cross the imaginary axis then ZHB or fold-Hopf bifurcation (FHB) occurs.*

In addition, transversality condition [89] is required for ensuring a change in sign of the real part of a complex eigenvalue when crossing through the HB point. The corresponding condition is $\frac{\mathrm{d}(Re(\lambda(\alpha_H)))}{\mathrm{d}\alpha} \neq 0$, where α_H indicates the HB point. The detail of transversality condition is given in Chapter A.

A 2.2 kW IM with parameters given in Table 3.2 [11] is considered for the bifurcation study. The reference signals and controller parameters are taken, in general, if otherwise not mentioned, as: $\omega_{ref} = 100$ rad/sec, $\psi_{drref} = 0.55$ Wb, $K_{p\omega} = 0.2$, $K_{i\omega} = 20$, $K_{pd} = K_{pq} = 60$ and $K_{id} = K_{iq} = 2 \times 10^4$.

Note that, the IVCIM (3.4)-(3.11) for $\alpha \neq 1$ always has two equilibrium points within the range (3.24). By checking the eigenvalues of G_{HOM}, one obtains the stable equilibrium point from (3.21) as:

$$x_1^e = \begin{cases} \frac{-m+\sqrt{m^2-4ln}}{2l} & \text{if } \alpha < 1 \\ \frac{-m-\sqrt{m^2-4ln}}{2l} & \text{if } \alpha > 1 \end{cases} \tag{3.27}$$

At the limiting points of (3.24), the two equilibrium points collide with each other and then disappear, which represents a SNB behavior [91].

Table 3.2: IM Parameters for analysis

Notation	Value	Notation	Value
P	4	Ω_b (rated speed)	1430 rpm
R_s	0.877 Ω	R_r	1.47 Ω
L_s	0.165 H	L_r	0.165 H
L_m	160.8 mH	J	0.015 kgm^2

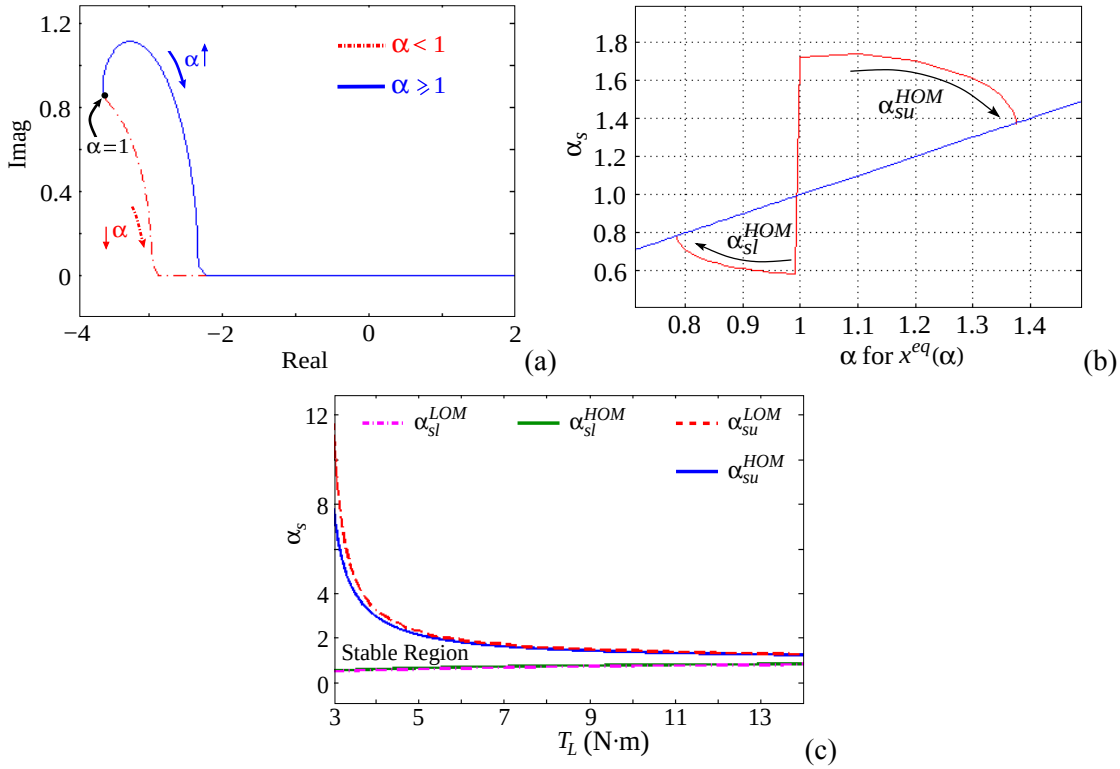

Figure 3.2: (a) Variation of eigenvalue. (b) Variation in α_s. (c) Bifurcation curves for α_s with T_L.

3.3.1 Saddle-Node Bifurcation (SNB)

The α value that corresponds to SNB (following Definition 1) is denoted as α_s. For the HOM, α_s corresponding to lower and upper limit of (3.24) are denoted as α_{sl}^{HOM} and α_{su}^{HOM}, respectively. Similarly, SNB points of LOM are denoted as α_{sl}^{LOM} and α_{su}^{LOM}.

Note that, the equilibrium point (3.12)-(3.19) is dependent on α and thereby (3.25) as well. Therefore, determination of α_s is, in general, iterative. Let the stable equilibrium point $x^{eq}(\alpha)$ obtained at $\alpha = \alpha_{eq}$, where α_{eq} represents the value of α at which the system is linearized.

First, we consider demonstrating the variation of dominant eigenvalue of G_{HOM} at $\alpha_{eq} = 1$. This is shown in Fig. 3.2(a), which depicts the occurrence of SNB with $\alpha_{sl}^{HOM} = 0.581$ and $\alpha_{su}^{HOM} = 1.721$ since one eigenvalue crosses through the origin. Note that $\alpha_s \neq \alpha_{eq}$ and hence is conservative. How α_s is affected by varying α_{eq} is determined.

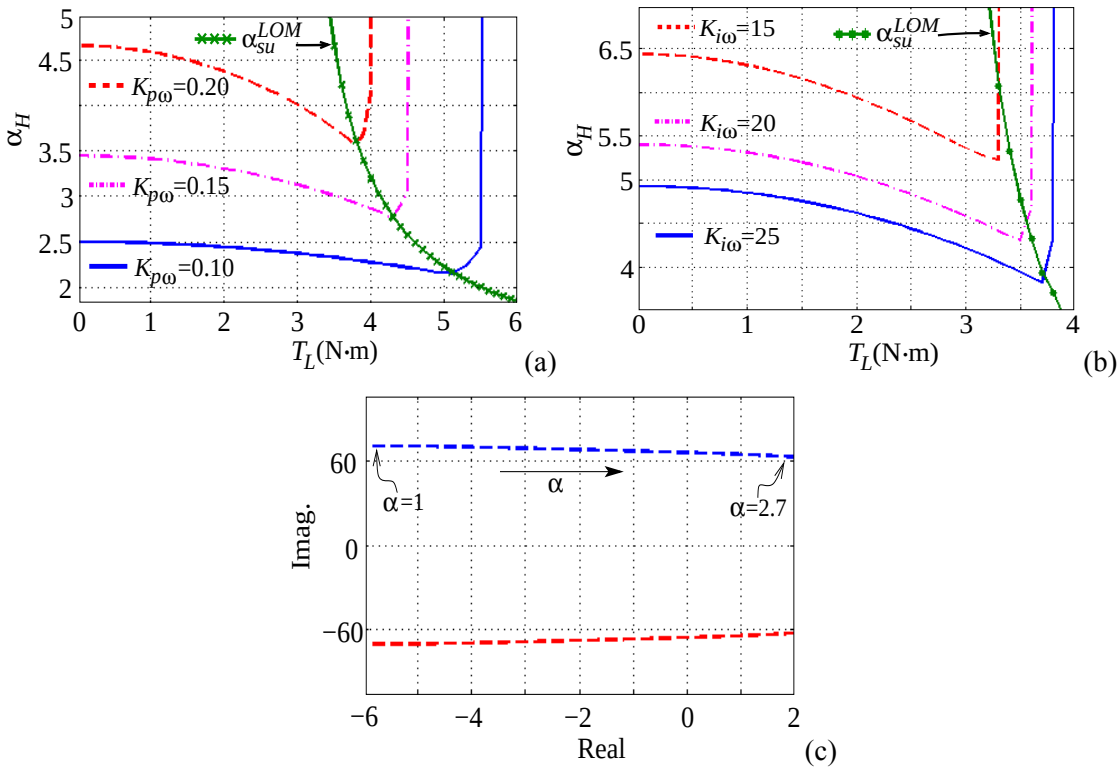

Figure 3.3: (a) Variation of α_H for $K_{i\omega} = 30$. (b) Variation of α_H for $K_{p\omega} = 0.2$. (c) Variation of eigenvalues w.r.t. α.

The effect is shown in Fig. 3.2(b). It is obtained that the two α values become equal at $\alpha_{eq} = \alpha_{sl}^{HOM} = 0.7857$ and $\alpha_{eq} = \alpha_{su}^{HOM} = 1.3752$. These α_s are exactly the same where the equilibrium point vanishes as per (3.24). Moreover, $x^{eq}(\alpha)$ does not depend on $K_{p\omega}$ and $K_{i\omega}$ as observed in [9] as well.

Now, consider the characteristic equation of (3.25) for the LOM as

$$H(\lambda) = \lambda^6 + p_5\lambda^5 + p_4\lambda^4 + p_3\lambda^3 + p_2\lambda^2 + p_1\lambda + p_0 \tag{3.28}$$

where $p_0, \cdots, p_5$, are the coefficients that can be obtained from G_{LOM}. Following the Definition 1, SNB condition is

$$p_0(\alpha) = 0 \tag{3.29}$$

where $p_0(\alpha)$ is a 4^{th} order polynomial for $T_L \neq 0$. An iterative procedure, Algorithm 1, is used to obtain a solution of α satisfying (3.29). The convergence and accuracy of the algorithm rely on the parameters ε_1 and ε_2. The convergence is slow for smaller ε_1 though the accuracy on computing α may improve since the error is $max(\varepsilon_1, \varepsilon_2)$. Moreover, these two parameters can be chosen independently with sign of ε_2 decides whether upper or lower limit of SNB is attained.

Next, the impact of loading T_L on α_s is studied. The bifurcation loci in the parameter space of $T_L - \alpha_s$ is shown in Fig. 3.2(c). It is observed that as T_L is increased, the gap between the upper (>1) and the lower (<1) limit is reduced. For $T_L < 3$ N·m, α_s is quite

Algorithm 1 Algorithm for computing bifurcation parameter α

choose $K_{p\omega}$, $K_{i\omega}$, K_{pd} and K_{pq}
assign $\alpha_{eq} = 1$, μ>0, $\varepsilon_1 > 0$, ε_2
loop:
calculate x_1^e to x_6^e using (3.12)-(3.19)
while $\mu > \varepsilon_1 || imag(x_1^e = 0)$ **do**
    obtain α_s from (3.29)
    compute $\mu = |\alpha_s - \alpha_{eq}|$
    $\alpha_{eq} = \alpha_{eq} + \varepsilon_2$
    goto *loop*.
    close;
end while

large which is of less practical significance and hence not shown. It can also be noticed that both LOM and HOM depict similar behavior, but LOM one is conservative at smaller T_L. Aforementioned observations thus lead to the following. - In the IVCIM (3.4)-(3.11), the following occurs:

- For a given loading condition, boundary points of (3.24) are the SNB points.
- SNB appears for underestimation ($\alpha < 1$) as well as overestimation ($\alpha > 1$) of rotor resistance from the nominal one ($\alpha = 1$).

3.3.2 Hopf Bifurcation (HB)

The α value corresponding to HB is denoted as α_H. Since it is difficult to obtain α_H using the HOM, α_H corresponding to the LOM is only considered. The HB condition can be obtained by applying Routh-Hurwitz criterion on (3.28) as

$$f(\alpha_H, K_{p\omega}, K_{i\omega}, T_L) = v_4 v_5 - p_0 v_3 = 0 \tag{3.30}$$

where p_i, $i = 0, 1, \cdots, 5$, are defined in (3.28) and

$$\left.\begin{aligned} v_1 =& \frac{p_4 p_5 - p_3}{p_5},\ v_2 = \frac{p_2 p_5 - p_1}{p_5},\ v_3 = \frac{v_1 p_3 - v_2 p_5}{v_1},\ \ v_4 = \frac{v_1 p_1 - p_0 p_5}{v_1}, \\ v_5 =& \frac{v_2 v_3 - v_1 v_4}{v_3}. \end{aligned}\right\} \tag{3.31}$$

Unlike the SNB, it is well known that HB depends on the choice of the speed-loop gains [13, 14]. Our observation with this study is also the same. Algorithm 1 is again used to obtain α_H by solving (3.30) instead of (3.29).

Variation of α_H for different choices of $K_{p\omega}$ and $K_{i\omega} = 30$ is shown in Fig. 3.3(a). It is detected that as $K_{p\omega}$ is increased, α_H occurs at a higher value and hence improves the stability of the IVCIM system. Next, effect of different choices of $K_{i\omega}$ for $K_{p\omega} = 0.2$ is considered. The corresponding result is shown in Fig. 3.3(b). In this case, increase in $K_{i\omega}$

has negative impact on stability. It can also be seen that there exists breakaway points after which, α_H increases drastically.

A variation of α_{su}^{LOM} is also shown in Fig. 3.3(a)-(b). Breakaway points in the α_H variations can be seen. These are the points where $\alpha_{su}^{LOM} = \alpha_H$. It happens because succeeding a particular T_L, the SNB dominates over HB and hence α_H occurs above α_s. However, this α_H is not of practical interest since stability is already lost due to the SNB. A certain discrepancy in breakaway points is also observed in Fig. 3.3(b). It occurs since LOM is used. Note that, importance of Fig. 3.3(a)-(b) is that for a given T_L, one can determine suitable speed-loop gains to avoid the occurrence of HB. Moreover, since SNB is more dangerous (it leads to larger oscillation phenomenon as compared to HB), the appearance of HB for lower T_L might work as a warning feature to avoid SNB.

A numerical verification of transversality condition for HB at a particular load through eigenvalue crossing is shown in Fig. 3.3(c). It can be seen that as α changes from 1 to 2.7 at $T_L = 4$ N·m, a pair of complex eigenvalues crosses to the right half plane at $\alpha_H = 2.27$ that satisfies the so-called transversality condition of the HB.

Next, variation in α_H with respect to T_L and α is determined. This is shown in Fig. 3.4. It is spotted that initially for $\alpha = 1$ as T_L is increased, α_H occurs comparatively at higher value. Further increment in α causes α_H to be smaller. It is also observed that α_H jumps to a higher value after the breakaway point. This phenomenon occurs because SNB dominates over HB as shown by the region (ii) in Fig. 3.4. The highlighted line in portion (i) in Fig. 3.4 shows the region where $\alpha_H = \alpha_{eq}$, hence these are the actual HB points. - In the IVCIM

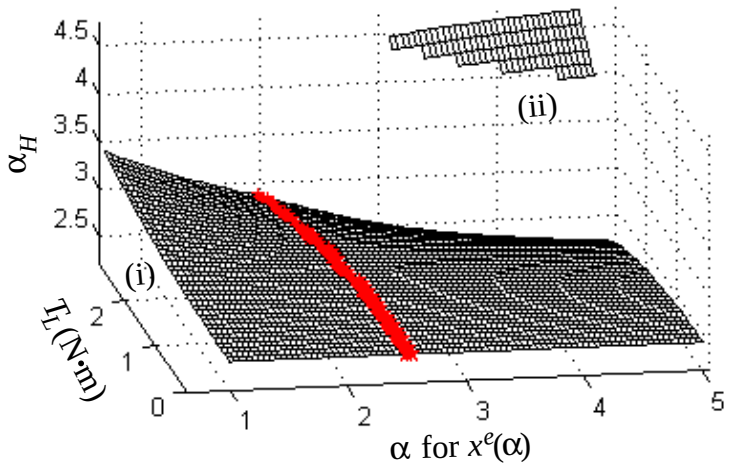

Figure 3.4: Variation of α_H with T_L for different α, $K_{p\omega} = 0.1$ and $K_{i\omega} = 30$: (i) α_H below α_s, (ii) α_H above α_s.

(3.4)-(3.11), the following occurs:

- HB depends on loading condition.
- At lower T_L, HB dominates SNB.

- For higher T_L, the SNB occurs before HB.
- Increment in $K_{p\omega}$ and decrement in $K_{i\omega}$ may avoid HB.

3.3.3 Bogdanov–Takens Bifurcation (BTB)

Since IVCIM is of higher order, complex bifurcation phenomenon other than SNB and HB may be observed, e.g. BTB, ZHB. The BTB condition, following Definition 1, is given as:

$$p_0 = 0 \text{ and } p_1 = 0, \tag{3.32}$$

where p_0 and p_1 are given in (3.28). The α value corresponding to BTB is denoted as α_{BTB}. Here, (3.24) is further used to determine equilibrium point at SNB following Hypothesis 1 in order to exploit the condition $p_0 = 0$, i.e. $m^2 - 4ln = 0$ in (3.27). At this point, the equilibrium state of x_1 is

$$x_1^e = -m/2l \tag{3.33}$$

Here, m and l depend on α_{eq}, which further depends on T_L as in (3.24). The lower and upper limits in (3.24) correspond to $\alpha_{eq} \leq 1$ and $\alpha_{eq} \geq 1$, respectively. Hence for each T_L, the equilibrium point is unique for $p_1 = 0$. Now, for determining BTB, at a given T_L, (3.33) is used to evaluate $p_1 = 0$, which ensures satisfaction of (3.32). First, $p_1 = 0$ is evaluated by determining equilibrium point at $\alpha_{eq} \leq 1$. The corresponding variation of $p_1 = 0$ is shown in Fig. 3.5(a). A BTB point can be detected if solution of $p_0 = 0$ and $p_1 = 0$ crosses each other. It is observed that for large $K_{p\omega} = 10$ and $K_{p\omega} = 100$, $p_1 = 0$ solution crosses α_{su}^{LOM} ($p_0 = 0$) solution. Whereas at the equilibrium point for $\alpha_{eq} \geq 1$, $p_1 = 0$ solution always asymptotic to α_{su}^{LOM} ($p_0 = 0$) solution as shown in Fig. 3.5(b). This leads to the following. - In the IVCIM (3.4)-(3.11), BTB occurs only for $\alpha < 1$ at particular loading condition and speed-loop gains.

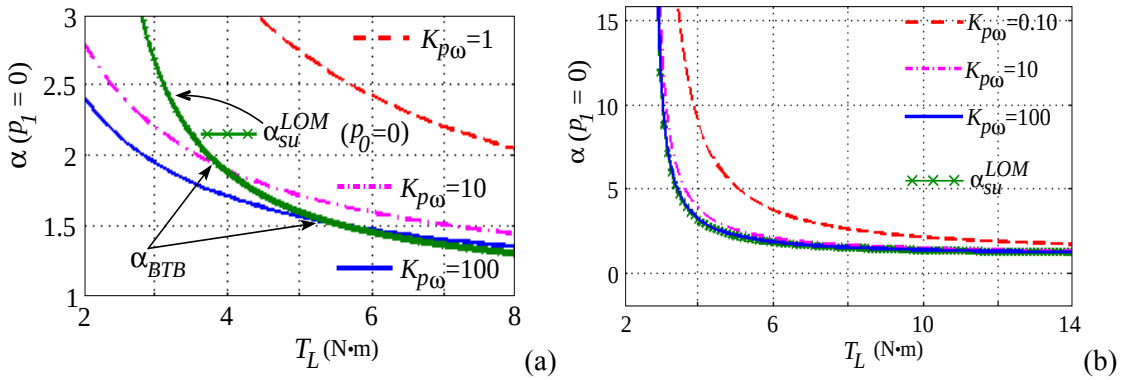

Figure 3.5: Variation of α for BTB with $K_{i\omega} = 30$ at: (a) $\alpha < 1$, (b) $\alpha > 1$.

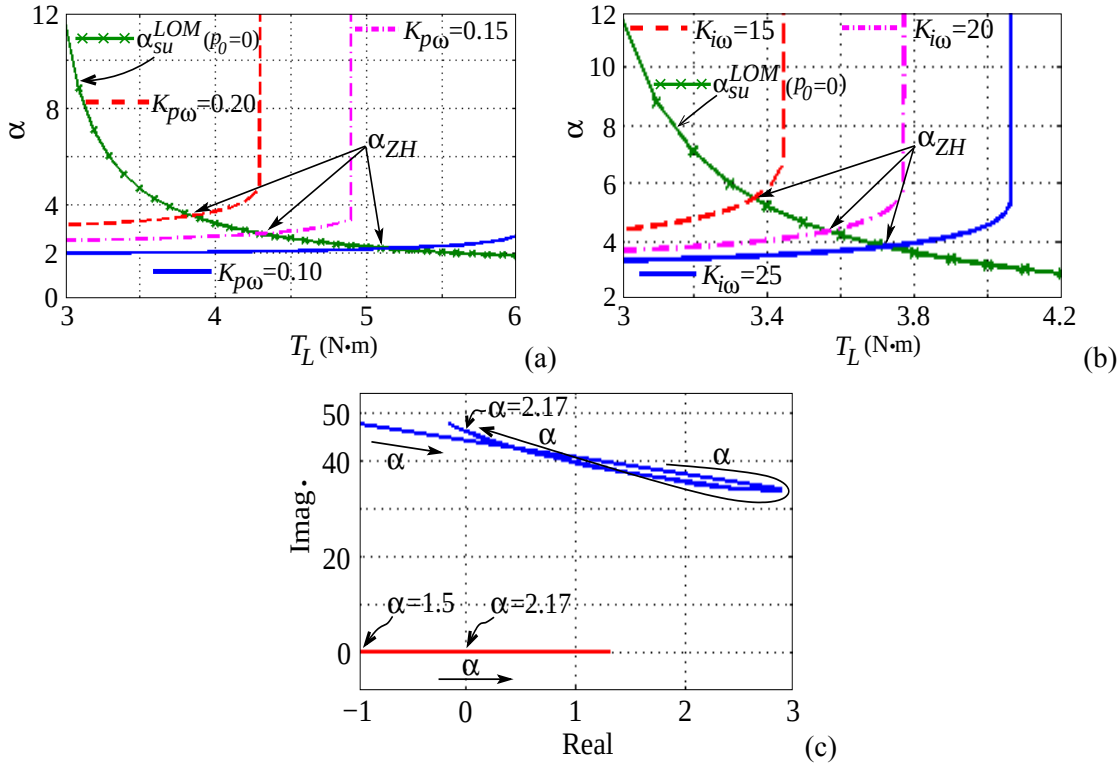

Figure 3.6: (a) Variation of α for $K_{i\omega} = 30$. (b) Variation of α for $K_{p\omega} = 0.2$. (c) Variation of eigenvalues w.r.t. α.

3.3.4 Zero-Hopf Bifurcation (ZHB)

The α value for ZHB is denoted as α_{ZH}. Using the Routh-Hurwitz criterion, the ZHB condition is:

$$p_0 = 0 \text{ and } v_2 v_3 - v_1 p_1 = 0 \tag{3.34}$$

where v_1, v_2 and v_3 are given in (3.31). In this regard, note that, the solution of $v_2 v_3 - v_1 p_1$=0 depends on $K_{p\omega}$ and $K_{i\omega}$, whereas the other one in (3.34) does not. The cross-section points of the two solutions for different $K_{p\omega}$ and $K_{i\omega}$ are the ZHB points as shown in Fig. 3.6(a)-(b). It can be observed that ZHB occurs at particular T_L depending on $K_{p\omega}$ and $K_{i\omega}$. As $K_{p\omega}$ is increased or $K_{i\omega}$ is decreased, ZHB occurs at higher α. It is interesting to see that ZHB points are the same as the breakaway points in Fig. 3.3(a)-(b). The corresponding eigenvalue behavior at a particular $T_L = 5.04$ N·m is shown in Fig. 3.6(c). For $T_L = 5.04$, first HB occurs at $\alpha = 2.15$ with the crossing of a pair of complex eigenvalue to the right-half complex plane. As α is increased to 2.17, a real eigenvalue along with a pair of complex eigenvalue cross imaginary axis from the right to the left-half complex plane, depicting occurrence of ZHB. This leads to the following hypothesis. - In the IVCIM (3.4)-(3.11), the following occurs:

- ZHB occurs at a particular loading condition.

- Increment in $K_{p\omega}$ and decrement in $K_{i\omega}$ may help to avoid ZHB.

The below results for the motor parameters from [1, 2] are shown in Fig. 3.7. It can be observed that the bifurcation behavior demonstrated occur for broader set of IVCIM.

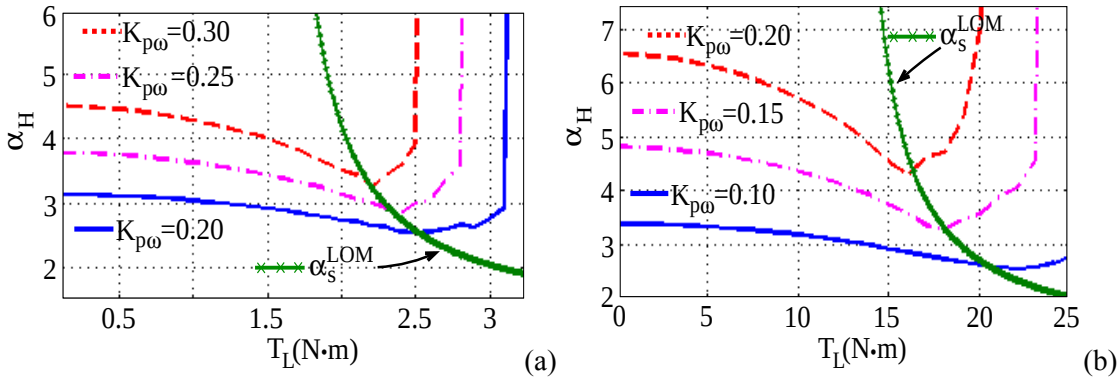

Figure 3.7: (a) Variation of α_H at $K_{i\omega}$=40 for the IM in [1]. (b) Variation of α_H at $K_{i\omega}$=30 for the IM in [2].

3.4 Bifurcation Analysis of Classical IVCIM

The classical IVCIM [6, Page 368] is shown in Fig. 3.8. The general IVCIM in Fig. 3.1 can be converted into the classical IVCIM by considering the reference currents to be independent of the flux dynamics, i.e., $i_{dsref} = \frac{\psi_{drref}}{L_m}$ and $i_{qsref} = \frac{T_{re}}{K_t \psi_{drref}}$. By using above substituton in (2.20) and (3.2), the reference currents and slip speed are given as:

$$i_{dsref} = \frac{\psi_{drref}}{L_m}, \quad i_{qsref} = dT_{re} \quad \text{and} \quad \omega_{sl} = \frac{\alpha\sigma L_m i_{qsref}}{\psi_{drref}} \tag{3.35}$$

where $d = \frac{1}{K_t \psi_{drref}}$.

After combining (2.20), (3.3) and (3.35) with the state variable definition of the general

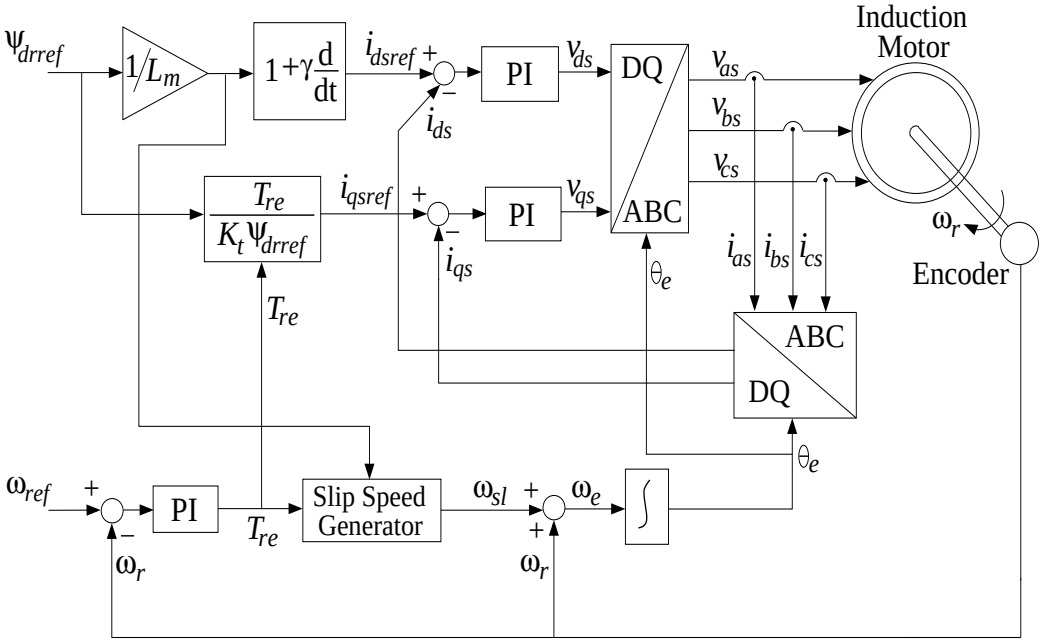

Figure 3.8: Indirect vector control of induction motor.

IVCIM, the state-space model of the classical IVCIM system is given as

$$\left.\begin{aligned}
\dot{x}_1 =& -ax_1 + [\omega_{ref} - x_5 + \alpha\sigma L_m (K_t\psi_{drref}^2)^{-1}x_6]x_2 + b\sigma x_3 + b(\omega_{ref} - x_5)x_4 \\
&+ cK_{pd}\left(L_m^{-1}\psi_{drref} - x_1\right) + cK_{id}x_7 \\
\dot{x}_2 =& -[\omega_{ref} - x_5 + \alpha\sigma L_m (K_t\psi_{drref}^2)^{-1}x_6]x_1 - ax_2 - b(\omega_{ref} - x_5)x_3 + b\sigma x_4 + \\
&cK_{pq}\left[(K_t\psi_{drref})^{-1}x_6 - x_2\right] + cK_{iq}x_8 \\
\dot{x}_3 =& \sigma L_m x_1 - \sigma x_3 + \alpha\sigma L_m (K_t\psi_{drref}^2)^{-1}x_6 x_4 \\
\dot{x}_4 =& \sigma L_m x_2 - \sigma x_4 - \alpha\sigma L_m (K_t\psi_{drref}^2)^{-1}x_6 x_3 \\
J\dot{x}_5 =& -K_m\left[K_t(x_2x_3 - x_1x_4) - T_L\right] + B_m(\omega_{ref} - x_5) \\
J\dot{x}_6 =& -K_{p\omega}[K_m\left[K_t(x_2x_3 - x_1x_4) - T_L\right] - B_m(\omega_{ref} - x_5)] + JK_{i\omega}x_5 \\
\dot{x}_7 =& L_m^{-1}\gamma\dot{\psi}_{drref} + L_m^{-1}\psi_{drref} - x_1 \\
\dot{x}_8 =& (K_t\psi_{drref})^{-1}x_6 - x_2.
\end{aligned}\right\} \tag{3.36}$$

In this section, the bifurcation for this classical one is presented. The state equilibriums

are determined as:

$$\left.\begin{aligned} &x_1^e = \psi_{drref}/L_m, \;\; \alpha L_m^2 \zeta r K_t \psi_{drref} (x_2^e)^3 - \left(\frac{K_m T_L}{J} + \frac{B_m \omega_{ref}}{J}\right) \\ &\quad (\alpha^2 L_m^2 r^2 K_t^2 \psi_{dref}^2)(x_2^e)^2 + \alpha L_m^2 r \zeta (x_1^e)^2 K_t \psi_{dref} x_2^e - \left(\frac{K_m T_L}{J} + \frac{B_m \omega_{ref}}{J}\right) = 0, \\ &x_3^e = \frac{L_m x_1^e + \alpha r L_m^2 x_2^e x_6^e}{1 + \alpha^2 r^2 L_m^2 (x_6^e)^2}, \;\; x_4^e = \frac{L_m x_2^e - \alpha r L_m^2 x_1^e x_6^e}{1 + \alpha^2 r^2 L_m^2 (x_6^e)^2}, \;\; x_5^e = 0, \\ &x_6^e = K_t \psi_{drref} x_2^e \end{aligned}\right\} \tag{3.37}$$

where $r = \frac{1}{K_t \psi_{drref}^2}$ and $\zeta = \frac{K_m K_t}{J}$. The remaining x_7^e and x_8^e can also be determined from (3.36).

Using the Cardano's formula [92], the solution of cubic equation in (3.37) is obtained as

$$u = \sqrt[3]{\frac{h \pm \sqrt{h^2 + 4g^3/27}}{2}} \tag{3.38}$$

where $g = \left(q_3 - \frac{q_2^2}{3q_1}\right)/q_1$, $h = \left(q_4 + \frac{2q_2^3}{27q_1^2} - \frac{q_2 q_3}{3q_1}\right)/q_1$ and $x_2^e = u - \frac{\zeta_2}{3\zeta_1}$. Here, q_1, q_2, q_3 and q_4 are the coefficients of the cubic polynomial in (3.37). By using the relation of x_2^e and u, one obtains six roots of x_2^e. However, out of these roots, three are the same. Hence, for each T_L, one can obtain three values of x_2^e. The existing condition of these roots can be determined from (3.38), which is further used to obtain the bifurcation condition.

3.4.1 SNB

Following (3.38), let us define

$$y = h^2 + 4g^3/27. \tag{3.39}$$

It is observed that for a specific T_L, as α is varied, y becomes zero, further negative and becomes positive as pass through zero again. When y becomes zero, three equilibrium points exist. At such originating value (α) of three equilibrium points of which two are equal implies two equilibrium points. It is observed numerically that for a T_L at which y becomes zero, classical IVCIM has an SNB point ($\alpha = \alpha_s$). Further, when y becomes negative, three different equilibrium points exist, whereas for the remaining region, classical IVCIM has a unique equilibrium point. Such behavior of equilibrium point with variation in α for a $T_L = 3$ N·m is shown in Fig. 3.9. It is observed that as α is varied, y becomes zero at $\alpha = 3.165$ and 3.294, respectively. These values of α yields the SNB points.

Note that, (3.39) is independent of variation in x_i^e, $i = 1, \cdots, 8$, as well as the outer-speed loop gains $K_{p\omega}$ and $K_{i\omega}$. Bifurcation curves that depict the change in equilibrium points with variation in T_L are shown in Fig. 3.10. In these curves, SNB points are represented as lower and upper boundaries. This curve is the same as obtained in [9]. Here, both curves α_s and α_s^{LOM} ($p_0 = 0$) are determined at the equilibrium point as determined from (3.38).

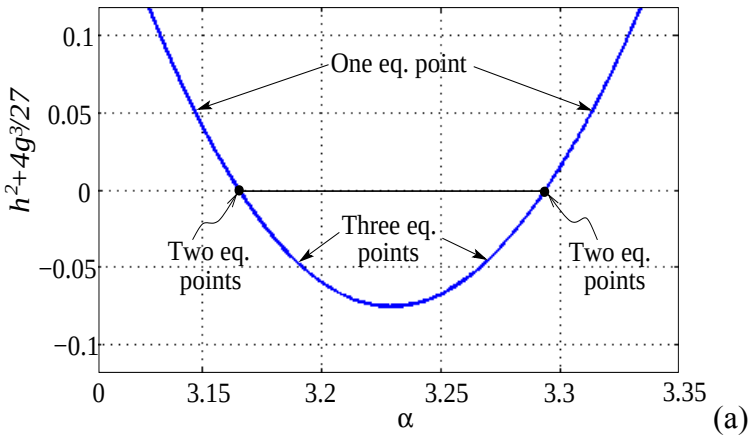

Figure 3.9: Variation in equilibrium points with α at $T_L = 3$ N·m.

At underestimation of rotor resistance $\alpha < 1$, SNB points are not detected. For numerical characterization of such bifurcation, variation of two dominant eigenvalues for $T_L = 3$ N·m and variation in α is shown in Fig. 3.11. It is observed that, at $\alpha_s = 3.34$, one of the eigenvalues crosses through origin that validates the SNB.

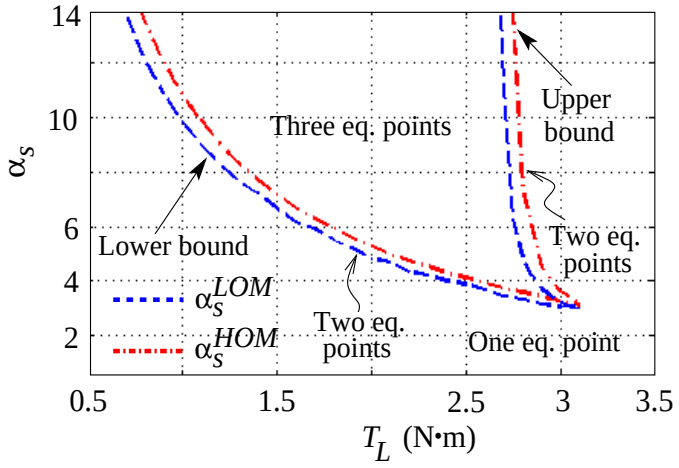

Figure 3.10: Bifurcation curves indicating change in equilibria with T_L.

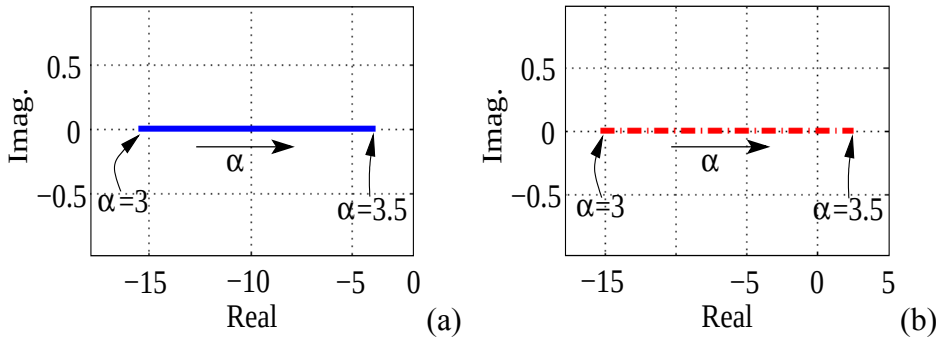

Figure 3.11: Variation of eigenvalues w.r.t. α for $T_L = 3$ N·m: (a) Dominant eigenvalue 1, and (b) Dominant eigenvalue 2.

3.4.2 HB

The HB points are determined at given loading conditions using the same procedure as discussed in Section 3.3. The results corresponding to different $K_{p\omega}$ and $K_{i\omega}$ are shown in Fig. 3.12(a)-(b). The plot of α_s^{LOM} (corresponding to SNB) is also shown there. It is observed that HB occurs at higher α_H with increase in $K_{p\omega}$, whereas it is other way for $K_{i\omega}$. Moreover, for higher T_L and $K_{p\omega}$, HB is more prominent. Such variation of α_H with T_L is in contradiction to the study in [14], where it is shown that α_H increases with T_L. A numerical verification of transversality condition at a particular load for HB through eigenvalue variation is shown in Fig. 3.13. It is seen that as α varies from 1.8 to 3.5 for $T_L = 2$ N·m, a pair of eigenvalues crosses to the right-half plane at $\alpha_H = 2.68$.

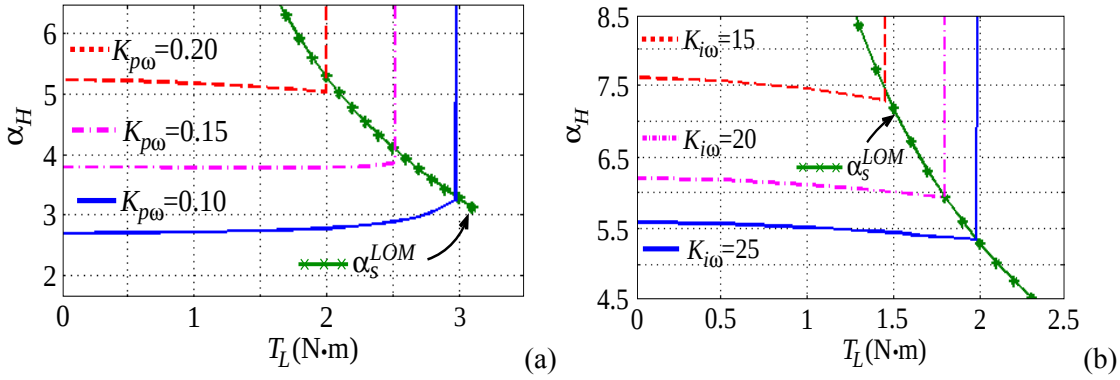

Figure 3.12: (a) Variation of α_H for $K_{i\omega} = 30$. (b) Variation of α_H for $K_{p\omega} = 0.2$.

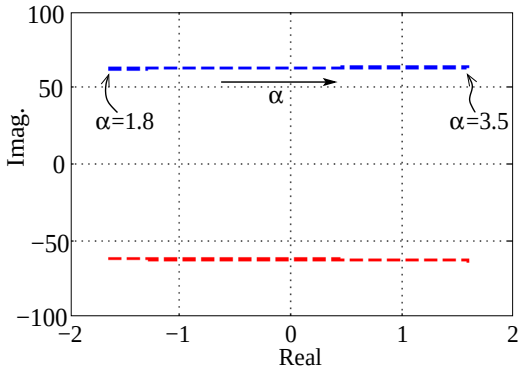

Figure 3.13: Variation of a pair of eigenvalues w.r.t. α when $T_L = 2$ N·m.

A comparison between present analysis approach of higher-order model and existing lower-order model [9, 13–15] (neglected stator current dynamics) at $T_L = 0$ N·m is shown in Table 3.3. The obtained results from Fig. 3.12 and Table 3.3 are matched with the simulation results (as shown later) which depicts that using the higher-order model, more accurate bifurcation points can be achieved.

Table 3.3: Comparison of HB points at $T_L = 0$ N·m

Lower-order model [9, 13–15] (Neglected stator current dynamics)				**Higher-order model**			
$K_{i\omega} = 30$		$K_{p\omega} = 0.2$		$K_{i\omega} = 30$		$K_{p\omega} = 0.2$	
$K_{p\omega}$	α_H	$K_{i\omega}$	α_H	$K_{p\omega}$	α_H	$K_{i\omega}$	α_H
0.1	7.02	15	-40.68	0.1	2.69	15	7.6
0.15	12.96	20	196.33	0.15	3.79	20	6.2
0.2	28.76	25	43.67	0.2	5.23	25	5.58

3.4.3 BTB

BTB condition for the classical IVCIM is determined similar to general one and it is shown in Fig. 3.14. It is observed that the BTB is almost indpendent of $K_{p\omega}$ and $K_{i\omega}$ variation and occurs at $\alpha_{BT} = 4.65$ and $T_L = 2.26$ N·m. The result is in agreement to that obtained in [15, 93].

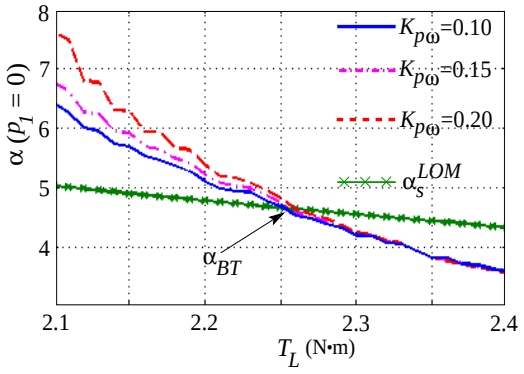

Figure 3.14: Variation of α with T_L for BTB at $K_{i\omega} = 30$.

3.4.4 ZHB

For the classical IVCIM, ZHB condition is similar to the general one. The corresponding result is shown in Fig. 3.15(a). Similar to the generalized case, the occurrence of ZHB depends on $K_{p\omega}$. It can be seen that, for higher value of $K_{p\omega}$, ZHB occurs at higher α. It is also observed that breakaway points in Fig. 3.12(a) are matched with α_{ZH} points. A numerical verification of such bifurcation at a particular load is shown in Fig. 3.15(b). For $T_L = 2.89$N·m, first HB occurs at $\alpha = 3.13$ with the crossing of a pair of complex eigenvalue to the right-half complex plane. As α is increased to 3.45, a real eigenvalue approaches zero along with a pair of complex eigenvalue approaches imaginary axis crossing from the right-half complex plane to the left-half one, depicting occurrence of ZHB.

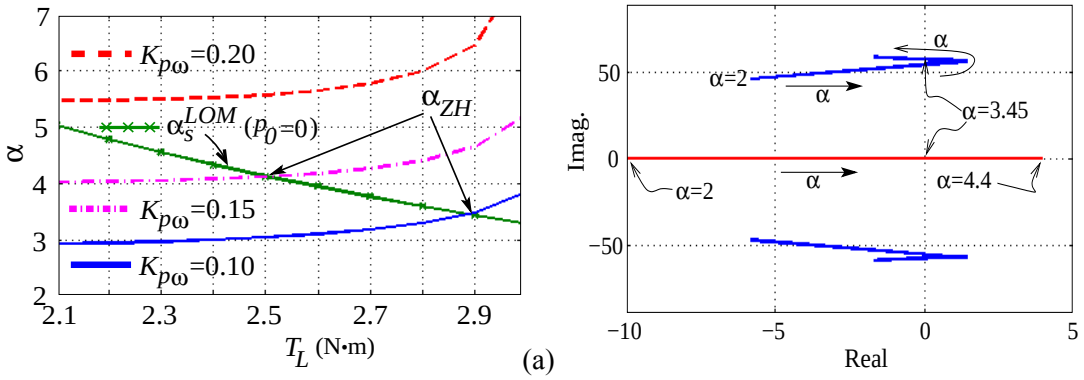

Figure 3.15: Variation of α with T_L for ZHB at $K_{i\omega} = 30$. Variation of eigenvalues w.r.t. α when $T_L = 2.89$ N·m.

3.5 Simulation Results

For verifying the analysis in Section 3.3 and Section 3.4, the IVCIM in Fig. 3.1, is simulated with the motor parameters as given in Table 3.2. First, the occurrence of SNB is verified. For this, α is varied (i) above the tuned condition ($\alpha = 1$) and (ii) below $\alpha = 1$. A step load of $T_L = 10$ N·m is applied at 4 sec for $\alpha = 1.39$ and $\alpha = 0.76$. The corresponding current responses are shown in Fig. 3.16(a)-(b), respectively. It can be seen that after the transient period, the currents exhibit oscillatory behavior of high amplitude.

Next, consider verification of the HB. At $\alpha = \alpha_H = 2.43$, $T_L = 2$ N·m is applied at 7.2 sec and it is increased in step to 3 N·m at 27 sec. The corresponding behavior is shown in Fig. 3.16(c). It is detected that as T_L reaches 3 N·m, HB is initiated. Further, HB behavior is studied at higher T_L. For this, T_L is increased in step to 2 N·m at 4 sec and then to 5 N·m at 12 sec. Corresponding result at $\alpha = \alpha_H = 2.145$ is shown in Fig. 3.16(d). Next, $K_{p\omega}$ is increased to 0.2 and T_L is changed in step from 2 N·m at 4 sec to 3 N·m at 18 sec. The corresponding behavior is shown in Fig. 3.16(e). Now, HB occurs at a higher value of $\alpha = \alpha_H = 4.14$. Similarly, effect of $K_{i\omega}$ has been verified but not shown here. Next, verification of ZHB corresponding to the result in Fig. 3.6(a) is shown in Fig. 3.16(f). It is observed that due to ZHB, oscillation magnitude is higher than that for the HB as in Fig. 3.16(c)-(e).

Similar to the general IVCIM, simulation is also carried out for classical IVCIM. First, the occurrence of SNB is verified. For this, a step load of $T_L = 3$ N·m is applied at 10 sec for $\alpha = 3.43$. The corresponding current behavior is shown in Fig. 3.16(g). It is observed that after the transient period, i_{qs} is large. Next, verification of the HB analysis is considered. First, α_H behavior for increment in $K_{p\omega}$ is analyzed. For this, at 4 sec, simultaneous step changes in α from 1 to 2.71 (α_H) and in T_L from 0 to 2 N·m are applied. The corresponding behavior is shown in Fig. 3.16(h) that shows HB. Further, $K_{p\omega}$ is increased to 0.2 and the corresponding result is shown in Fig. 3.16(i). It is observed that now HB does not occur at 4 sec. However, as α is increased to 5.2 at 10 sec, HB reappears. Further, $K_{i\omega}$ is decreased

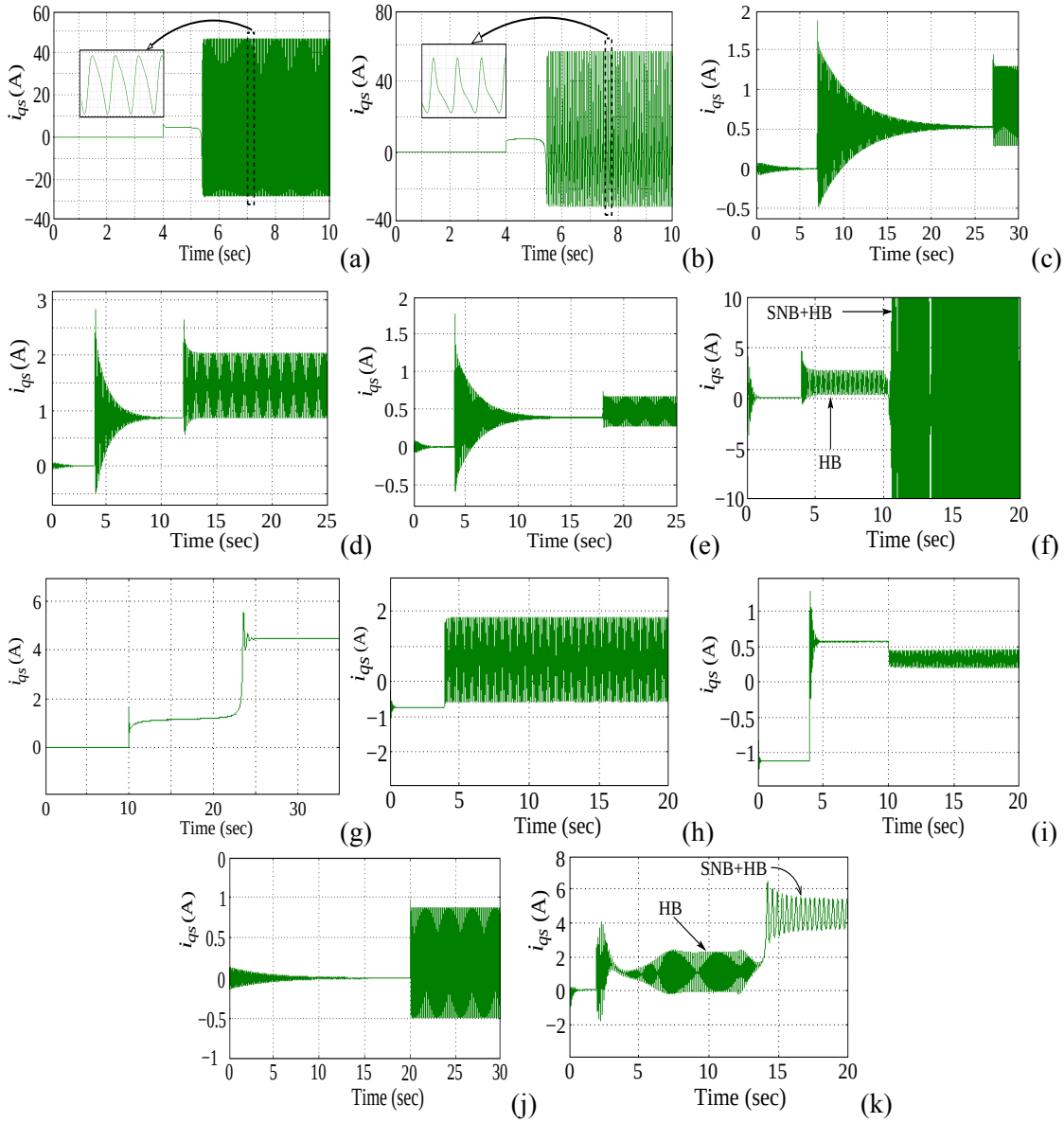

Figure 3.16: Simulation response of i_{qs} at: (a) $\alpha = 1.39$, (b) $\alpha = 0.76$, (c) $K_{p\omega} = 0.1$, $K_{i\omega} = 30$ and $\alpha = 2.43$, (d) $K_{p\omega} = 0.1$, $K_{i\omega} = 30$ and $\alpha = 2.145$, (e) $K_{p\omega} = 0.2$ and $K_{i\omega} = 30$, (f) $K_{p\omega} = 0.1$, $K_{i\omega} = 30$ and step change in α from 2.1 at 4 sec to 2.4 at 10 sec for $T_L = 5.12$ N·m, (g) $\alpha = 3.43$, (h) $K_{p\omega} = 0.1$, $K_{i\omega} = 30$, $\alpha = 2.71$ for $T_L = 2$ N·m, (i) $K_{p\omega} = 0.2$, $K_{i\omega} = 30$, step change in α from 2.71 at 4 sec to 5.2 at 10 sec for $T_L = 2$ N·m, (j) $K_{p\omega} = 0.2$, $K_{i\omega} = 25$ and $\alpha = 5.5$, and (k) $K_{p\omega} = 0.1$, $K_{i\omega} = 30$ and step change in α from 3.4 at 2 sec to 3.7 at 12 sec for $T_L = 2.90$ N·m, respectively.

to 25 and $\alpha = 5.5$ is applied initially at 0 sec, $T_L = 0$ N·m. The corresponding result is shown in Fig. 3.16(j). It is observed that, at such high α, HB does not occur. After 20 sec, $T_L = 1.5$ N·m is applied and then HB occurs. This result corroborates the result in Fig. 3.12(b). Here, it is noticed that larger T_L causes HB to occur at a smaller α. Verification of ZHB corresponding to the result in Fig. 3.15(a) is shown in Fig. 3.16(k). A high current oscillation is observed due to ZHB.

Table 3.4: Experimental IM Parameters

Notation	Value	Notation	Value
P	4	Ω_b (rated speed)	1410 rpm
R_s	5.12 Ω	R_r	2.26 Ω
L_s	0.332 H	L_r	0.338 H
L_m	0.320 H	J	0.085 kgm^2

3.6 Experimental Results

A KIRLOSKAR make 2.2 kW IM is used for experimental validation of some of the bifurcations (It may be noted that BTB and ZHB are difficult to validate). The experimental setup is shown in Fig. 3.17. The corresponding motor parameters are given in Table 3.4. The load is emulated by a shunt type dc generator coupled to the IM. The speed is sensed by an infrared based sensor which is placed on an 18 slotted circular disk. The control operation is implemented in dSPACE 1103 development board using SPWM3 block. The obtained PWM pulses are amplified from 5 to 15 volts using optocoupler 6N137 and CD4504 ICs corresponding to driver circuit (SKYPER 32 R) requirement of SEMIKRON make three phase rectifier- inverter stack. The rectifier circuit consists of an SKD160/18 diode bridge and two dc link capacitor of 4700μF. The switching frequency of the IGBT (SKM75GB12T4) based inverter is taken as 5 kHz. Three LA 25-NP sensors are used to feedback the stator currents to dSPACE ADCs. The controller and feedback signals are sampled at 10 kHz. The experiment is conducted without any external filter and controller saturation blocks. Since in the present analysis, certain dynamics (inverter, motor losses, controller response delay, motor response delay, dc generator dynamics etc.) have not been considered, a numerical discrepancy is expected.

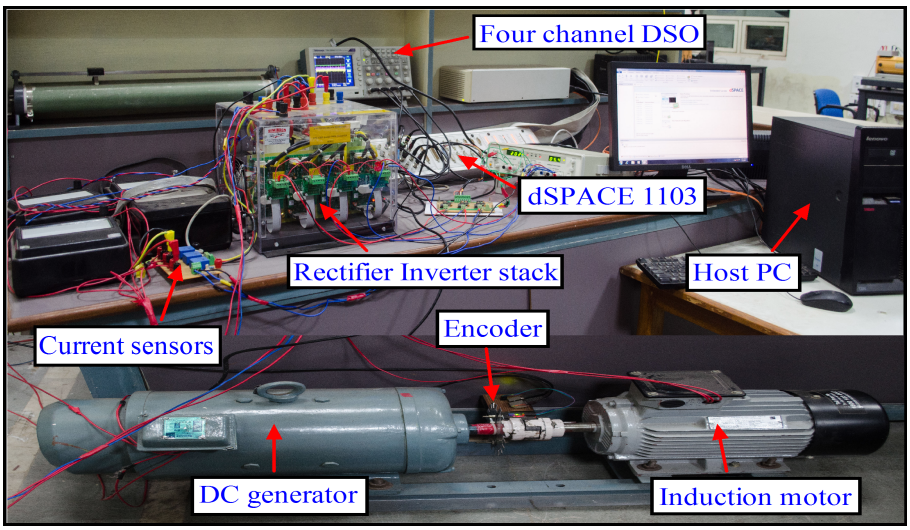

Figure 3.17: Experimental setup.

The bifurcation results obtained in Section 3.3 and 3.4 are verified to exist for this motor as well. First, bifurcation behaviors are studied for the general IVCIM. The SNB points are determined using (3.24), for $T_L = 6.5$ N·m, as $\alpha_s = 0.77$ and 1.40. The speed-loop gains are taken as $K_{p\omega} = 0.9$ and $K_{i\omega} = 2$. These values (higher $K_{p\omega}$ and lower $K_{i\omega}$) are chosen according to the numerical study (Fig. 3.3) and behavior of the IVCIM for different $K_{p\omega}$ and $K_{i\omega}$ to avoid a possible HB. The α in the control loop is changed using the variable array tool in dSPACE 1103 control desk. The corresponding i_{qs} variation for $\alpha < 1$ and $\alpha > 1$ is shown in Fig. 3.18(a)-(b) and Fig. 3.18(c), respectively. First, experiment for $\alpha < 1$ is implemented. For this, an equivalent T_L of 6.5 N·m is applied at 7.5 sec and correspondingly i_{qs} is increased. Now, α is changed as $1 \rightarrow 0.5 \rightarrow 0.2$ at 14.5 and 23.5 sec, respectively. The i_{qs} behavior for such changes in α is shown in Fig. 3.18(a). It is observed that at $\alpha = 0.2$, i_{qs} shows a large transient. Next, α is changed from 1 to 0.1 at 10 sec. As observed in Fig. 3.18(b), i_{qs} becomes more than the double resembling SNB and the motor stalls for not sustaining the high torque demand. For $\alpha > 1$ case, α is changed as $(1 \rightarrow 1.5 \rightarrow 2.5 \rightarrow 3)$. As α is changed to 1.5, a stable transient in i_{qs} is observed. Then a $T_L = 6.5$ N·m is applied at steady-state (at 11.5 sec), which leads to increase in i_{qs}. Next, as α is changed from 2.5 to 3 (at 27 sec), i_{qs} becomes almost double resembling SNB. Eventually the motor stalls.

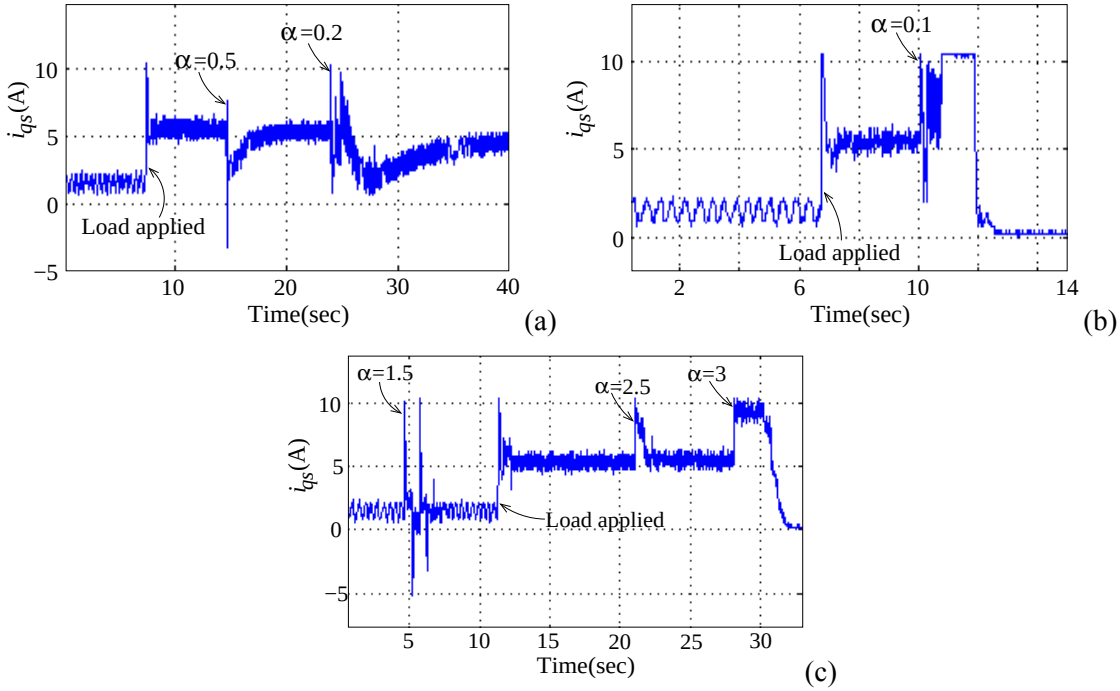

Figure 3.18: Experimental response of i_{qs} for general IVCIM at $K_{p\omega} = 0.9$, $K_{i\omega} = 2$ for change in α as: (a) $1 \rightarrow 0.5 \rightarrow 0.2$, (b) $1 \rightarrow 0.1$, and (c) $1 \rightarrow 1.5 \rightarrow 2.5 \rightarrow 3$.

Next, HB point is determined as $\alpha_H = 1.46$ for $K_{p\omega} = 0.1$ and $K_{i\omega} = 30$. Owing to instability problem in experimenting with large $K_{i\omega}$, a smaller value ($K_{i\omega} = 2$) is used. The behavior of i_{qs} with change in α is shown in Fig. 3.19(a). It is observed that i_{qs} is increased by a small amount when an equivalent step of $T_L = 2$ N·m is applied at 8 sec. As α is

changed to 1.5 (at 17.5 sec), i_{qs} starts oscillating confirming occurrence of HB.

Similar to general IVCIM, experiments are also carried out for the classical one with the same speed-loop gains. Numerical analysis for the classical one yields $\alpha_s = 3.1$. Initially α is changed as $1 \rightarrow 1.5 \rightarrow 2.5 \rightarrow 3$. An equivalent T_L of 6.5 N·m is applied at 13 sec. The corresponding result is shown in Fig. 3.19(b). It is observed that when α is changed from 2.5 to 3 (at 33 sec), i_{qs} increases to a high value and the motor stalls due to SNB.

The HB point for the classical IVCIM is obtained as $\alpha_H = 1.70$ for $K_{p\omega} = 0.1$ and $K_{i\omega} = 30$ at $T_L = 2$ N·m. However, in experiment, HB behavior is obtained at $\alpha_H = 1.8$ for $K_{p\omega} = 0.1$ and $K_{i\omega} = 2$ as shown in Fig. 3.19(c).

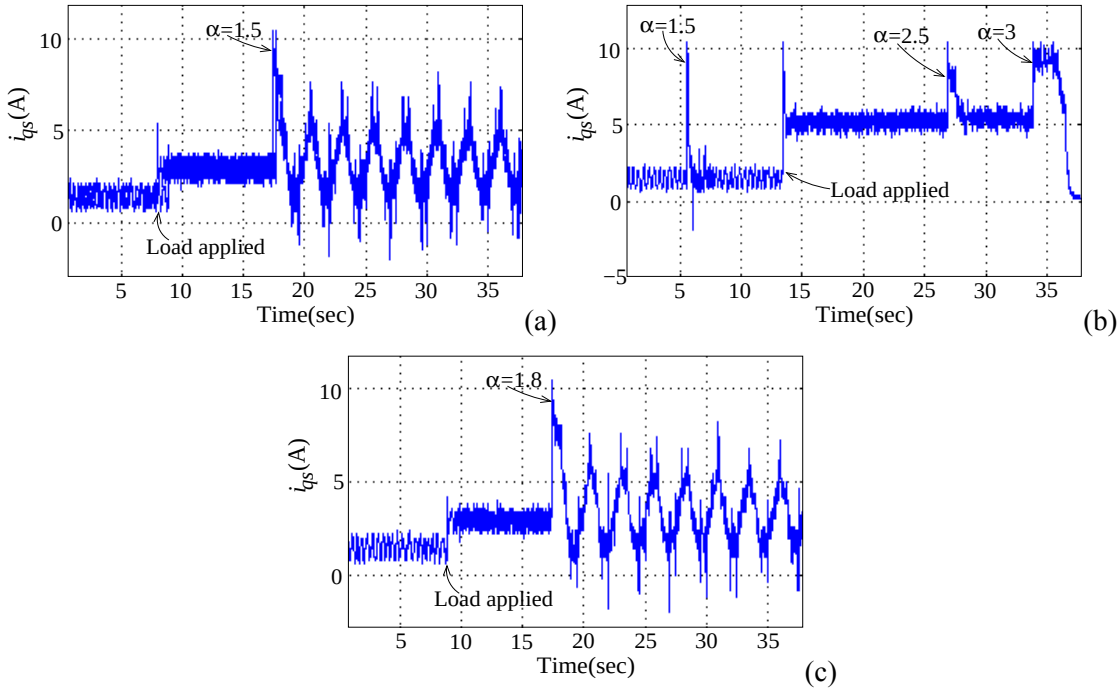

Figure 3.19: Experimental response of i_{qs}. (a) Generalized case: $K_{p\omega} = 0.1$, $K_{i\omega} = 2$ for change in α as $1 \rightarrow 1.5$. (b) Classical case: $K_{p\omega} = 0.9$, $K_{i\omega} = 2$ for change in α as $1 \rightarrow 1.5 \rightarrow 2.5 \rightarrow 3$. (c) Classical case: $K_{p\omega} = 0.1$, $K_{i\omega} = 2$ for change in α as $1 \rightarrow 1.8$.

From these results, it is found that SNB leads to high stator current and the motoring operation eventually stalls. On the other hand, even though stator current oscillations due to HB have smaller amplitude, the motor performance is still affected. Since HB does not arise in Fig. 3.18 and Fig. 3.19(b), even for higher α, tuning to a higher $K_{p\omega}$ may be used to avoid HB, but one has to be careful that the same should not lead to SNB.

3.7 Chapter Summary

In this chapter, bifurcation behavior in IVCIM has been studied numerically. It has been observed that choosing an appropriate equilibrium point is also a concern for determining a bifurcation point in IVCIM. For the purpose, an algorithm has been used to obtain more

accurate bifurcation points. A new SNB phenomenon has been observed at underestimation of rotor resistance. Further, effect of loading on HB has been evaluated. Complex bifurcation phenomenon such as BTB and ZHB has also been studied with variations of outer speed-loop gain. Validation of numerical analysis with simulation and experiment results (for SNB and HB) has also been presented. The rotor resistance variation also affects the dynamic performance of the motor. A proper PI tuning can minimize such effect and improve the motoring performance.

In the next chapter, a performance based PI tuning scheme is proposed for IVCIM where load torque and rotor resistance variations are treated as disturbances.

Chapter 4

Concurrent Speed and Current-Loop PI Tuning for IVCIM

4.1 Introduction

An improper rotor resistance estimation or a variation may lead to poor dynamic performance of the motor and may create bifurcation or chaos in IVCIM control operation [9, 18]. An approach for minimizing this effect have been relied on the robust stability based design of PI speed-loop controller [94]. However, this work has a limitation as the design does not consider dynamic performance and may cause instability as observed in [1]. Other PI speed-loop design methods also have been reported in [9, 13, 95]. These designs are based on the avoidance of the bifurcation phenomenon. On the other hand, in the absence of a suitable PI design method, a hit and trial based technique is also applied in literature [1, 96]. However, this method has limitations of desired initial gains, time-consuming and may lead to unpredictable behavior. Apart from the PI based speed-loop controller, several other linear and nonlinear control schemes have been proposed in [2, 97–101]. Although the nonlinear ones yield high performance but may induce complexity in implementation. Whereas among the linear ones, owing to simplicity, low-cost design and nominal performance, PI controllers are popular [1, 3, 19]. In recent work, a reduced order IM model based speed-loop compensator design is proposed in [3]. This controller has been tested with the stationary reference frame inner-loop compensator. However, the designed controller is based on robust stability that may affect the IVCIM performance.

The available current-loop control schemes are based on synchronous reference frame control (SRFC), stationary reference control (SRC), hysteresis control [102–107]. Among these methods, SRFC technique is often preferred to the advantages of operating on dc quantities, zero steady-state error, and the negligible cross coupling. Such performance depends on the efficient regulation of controller gains [108]. The tuning rules for inner current controller have been discussed in [1, 109]. These rules are based on approximated model of IM and rely on inner-loop sampling frequency. In a recent work [110], an SRC based cascaded combination of a PI controller and a compensator has been designed for satisfying specified decoupling performance. In this scheme, no feedforward terms

are employed, and the design criterion is simple based on gain margin (GM) and phase margin (PM) criterion. However, this robust stability based design involves a comparatively complicated structure than the conventional SRFC. In addition, since GM and PM of a multi-input multi-output (MIMO) system is involved in this design, the trade-offs of different performances, e.g., decoupling and robustness, are hard to obtain. In brief, although several control design techniques are available for IVCIM, a performance based PI controller design method, which inherits the robustness against the rotor resistance and load torque variations does not exist in literature. In addition, it is also of importance to devise a design procedure that can easily be facilitated to design controllers using advanced methods, e.g., H_∞ control [111].

On the other hand, for the controller design of finite dimensional linear time-invariant systems, static output feedback (SOF) technique has been used extensively in [112–116]. This technique has the following advantages: (i) a simple closed-loop controller structure can be framed, (ii) the design problem can be combined with an H_∞ control approach, (ii) when it is impossible to measure all the states, SOF may provide an alternative and effective control system structure. In this work, SOF based PI controller design method is proposed for IVCIM. For this, first, IVCIM state-space model is linearized around the equilibrium point. The linearized model is framed into SOF decentralized H_∞ controller design problem in which rotor resistance and load torque perturbations are considered as disturbances. The PI gains are tuned using an iterative linear matrix inequality (ILMI) based algorithm which ensures fast convergence and efficient design. A comparison between existing and proposed design technique is shown using simulation and experimental results.

The remaining of the chapter is organized as follows. Section 4.2 presents the IVCIM model equations which comprise of decoupled and concurrent control techniques. The control problem formulation and design algorithm are also presented in this Section. Comparison of the proposed method with existing one through simulation and experimental results is presented in Section 4.3 and Section 4.4, respectively. In the end, relevant discussions and conclusions are pointed out in Section 4.5.

4.2 IVCIM Model

The classical IVC scheme for IM is shown in Fig. 3.8. Since the rotor resistance variation perturbs the motor states from the desired regulation points, it is treated as disturbance, as the control problem is chosen. The corresponding perturbed slip speed is given as

$$\omega_{sl} = \frac{(\sigma + \delta) L_m T_{re}}{K_t \psi_{drref}^2} \tag{4.1}$$

where δ is the perturbation in σ due to variation in rotor resistance.

Corresponding to (4.1), the new perturbed IVCIM model following (3.36) is obtained as

$$\left.\begin{aligned}
\dot{x}_1 =& -ax_1 + [\omega_{ref} - x_5 + (\sigma+\delta)L_m(K_t\psi_{drref}^2)^{-1}x_6]x_2 + b\sigma x_3 \\
&+ b(\omega_{ref} - x_5)x_4 + cK_{pd}\left(L_m^{-1}\psi_{drref} - x_1\right) + cK_{id}x_7 \\
\dot{x}_2 =& -[\omega_{ref} - x_5 + (\sigma+\delta)L_m(K_t\psi_{drref}^2)^{-1}x_6]x_1 - ax_2 \\
&- b(\omega_{ref} - x_5)x_3 + b\sigma x_4 + cK_{pq}\left[(K_t\psi_{drref})^{-1}x_6 - x_2\right] + cK_{iq}x_8 \\
\dot{x}_3 =& \sigma L_m x_1 - \sigma x_3 + (\sigma+\delta)L_m(K_t\psi_{drref}^2)^{-1}x_6x_4 \\
\dot{x}_4 =& \sigma L_m x_2 - \sigma x_4 - (\sigma+\delta)L_m(K_t\psi_{drref}^2)^{-1}x_6x_3 \\
J\dot{x}_5 =& -K_m\left[K_t(x_2x_3 - x_1x_4) - T_L\right] + B_m(\omega_{ref} - x_5) \\
J\dot{x}_6 =& -K_{p\omega}[K_m\left[K_t(x_2x_3 - x_1x_4) - T_L\right] - B_m(\omega_{ref} - x_5)] + JK_{i\omega}x_5 \\
\dot{x}_7 =& L_m^{-1}\gamma\dot{\psi}_{drref} + L_m^{-1}\psi_{drref} - x_1 \\
\dot{x}_8 =& (K_t\psi_{drref})^{-1}x_6 - x_2.
\end{aligned}\right\} \quad (4.2)$$

The above state-space model is nonlinear and embodies the PI controller gains. In order to design the controllers, one requires linearizing the system around the equilibrium point. The corresponding control problem formulation is presented next.

4.2.1 Decoupled Controller Design

The decoupled control scheme is comprised of separate inner and outer control loop design. First, inner loop PI controller is designed. The obtained gain values from the inner loop are used in the outer loop controller design.

Inner loop Design

Let the outer speed-loop dynamics are negligible and motor speed is in steady-state ($\omega_r = \omega_{ref}$). The corresponding control diagram is shown in Fig. 4.1. Now, (6.9) is inherently linearized and its equilibrium point is determined by following the vector control principle [6] as

$$x_1^e = \frac{\psi_{drref}}{L_m},\ \ x_2^e = i_{qsref},\ \ x_3^e = \frac{\sigma L_m(\sigma x_1^e + \omega_{sl}x_2^e)}{\sigma^2 + \omega_{sl}^2},\ \ x_4^e = \frac{\sigma L_m(\sigma x_2^e - \omega_{sl}x_1^e)}{\sigma^2 + \omega_{sl}^2} \quad (4.3)$$

where x^e=$[x_1^e, \cdots, x_6^e]$ is the equilibrium point. Here, x_5^e and x_6^e are the states equilibrium points corresponding to current-loop integrator dynamics as considered $x_5 = \int (i_{dsref} - i_{ds})dt$, $x_6 = \int (i_{qsref} - i_{qs})dt$. These x_5^e and x_6^e can be determined using (6.9) and (4.3).

Note that, i_{qsref} is generated due to applied load torque T_L and it is taken as $\left\|i_{qsref}\right\| = \frac{T_L}{K_t\psi_{drref}} < i_{qsmax}$ [117].

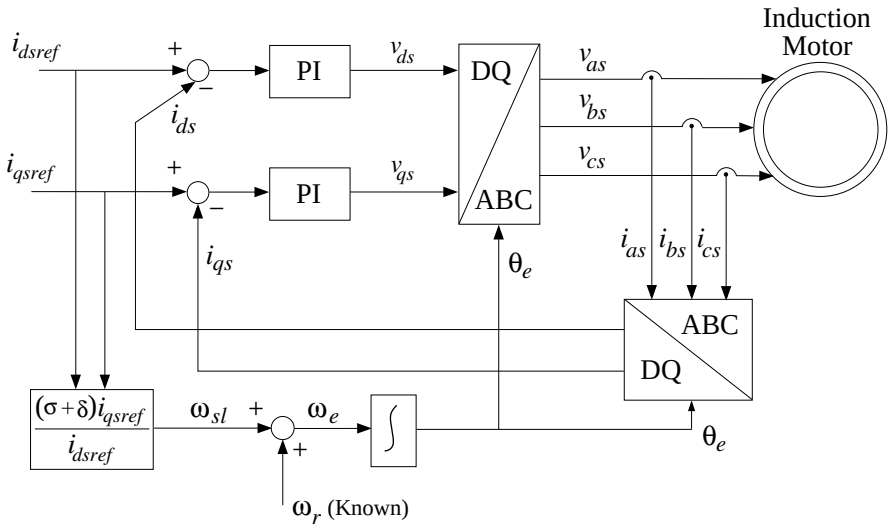

Figure 4.1: Inner-loop control of induction motor drive system.

The linearized model can be written as

$$\Delta\dot{x} = A_m \Delta x \tag{4.4}$$

where Δx=$[\Delta x_1, \cdots, \Delta x_6]^T$ represent the linearized states, A_m is the corresponding system matrix, which is comprised of states associated with system parameters, perturbation term δ and controller gains K_{pd}, K_{id}, K_{pq} and K_{iq}.

Considering the disturbance input to the system is through the variations in rotor resistance δ that can be modeled as

$$\Delta w = \begin{bmatrix} \delta\Delta x_1 & \delta\Delta x_2 & \delta\Delta x_3 & \delta\Delta x_4 \end{bmatrix}^T \tag{4.5}$$

Now, (4.4) can be written as a combination of system states with disturbance and controller gains terms:

$$\Delta\dot{x} = A\Delta x + R\Delta w + K\Delta x \tag{4.6}$$

where A represents the corresponding system matrix, R is the disturbance matrix and K is the control input matrix. These are given as

$$A = \begin{bmatrix} -a & \omega_{ref} + \frac{\sigma x_2^e}{x_1^e} & b\sigma & b\omega_{ref} & 0 & 0 \\ -\omega_{ref} - \frac{\sigma x_2^e}{x_1^e} & -a & -b\omega_{ref} & b\sigma & 0 & 0 \\ \sigma L_m & 0 & -\sigma & \frac{\sigma x_2^e}{x_1^e} & 0 & 0 \\ 0 & \sigma L_m & -\frac{\sigma x_2^e}{x_1^e} & -\sigma & 0 & 0 \\ -1 & 0 & 0 & 0 & 0 & 0 \\ 0 & -1 & 0 & 0 & 0 & 0 \end{bmatrix},$$

$$R = \begin{bmatrix} 0 & \frac{\sigma x_2^e}{x_1^e} & 0 & 0 \\ -\frac{\sigma x_2^e}{x_1^e} & 0 & 0 & 0 \\ 0 & 0 & 0 & \frac{\sigma x_2^e}{x_1^e} \\ 0 & 0 & -\frac{\sigma x_2^e}{x_1^e} & 0 \\ 0 & 0 & 0 & 0 \\ 0 & 0 & 0 & 0 \end{bmatrix} \text{ and}$$

$$K = \begin{bmatrix} -cK_{pd} & 0 & 0 & 0 & 0 & 0 \\ 0 & 0 & 0 & 0 & cK_{id} & 0 \\ 0 & -cK_{pq} & 0 & 0 & 0 & 0 \\ 0 & 0 & 0 & 0 & 0 & cK_{iq} \\ 0 & 0 & 0 & 0 & 0 & 0 \\ 0 & 0 & 0 & 0 & 0 & 0 \end{bmatrix}.$$

The K matrix can be written as a cascade combination of input and output matrices in the following way

$$K = B_2 F C_2 \tag{4.7}$$

where

$$B_2 = \begin{bmatrix} -c & 0 & 0 & 0 & 0 & 0 \\ 0 & -c & 0 & 0 & 0 & 0 \end{bmatrix}^T,$$

$$F = \begin{bmatrix} K_{pd} & K_{id} & 0 & 0 \\ 0 & 0 & K_{pq} & K_{iq} \end{bmatrix} \text{ and}$$

$$C_2 = \begin{bmatrix} 1 & 0 & 0 & 0 & 0 & 0 \\ 0 & 0 & 0 & 0 & -1 & 0 \\ 0 & 1 & 0 & 0 & 0 & 0 \\ 0 & 0 & 0 & 0 & 0 & -1 \end{bmatrix}.$$

Now, following [116], the control input Δu is defined as

$$\Delta u = F \Delta y \tag{4.8}$$

where $\Delta y = C_2 \Delta x$ measured output is so chosen that it transforms the PI controller design problem into a SOF controller design problem.

Following (4.1), (4.3), (4.7) and (4.8), the linearized closed-loop system (4.6) can be represented in SOF form as:

$$\left.\begin{aligned} \Delta \dot{x} &= A\Delta x + B_1 \Delta w + B_2 \Delta u \\ \Delta y &= C_2 \Delta x + D_{21} \Delta w + D_{22} \Delta u \\ \Delta z &= C_1 \Delta x + D_{11} \Delta w + D_{12} \Delta u \end{aligned}\right\} \tag{4.9}$$

where B_1 is the disturbance input matrix, B_2 is the control input matrix, C_1 and C_2 are

the output performance and feedback matrices, respectively, D with subscript notations [11 and 21] are the corresponding disturbance matrices, and D with subscript notations [12 and 22] are the direct feedthrough matrices. $\Delta z = \begin{bmatrix}\Delta x_1 & \Delta x_2 & \Delta x_3 & \Delta x_4\end{bmatrix}^T$ represents the desired performance output. The input disturbance matrix B_1 is same as R. The desired output matrix C_1 is given by

$$C_1 = \begin{bmatrix} 1 & 0 & 0 & 0 & 0 & 0 \\ 0 & 1 & 0 & 0 & 0 & 0 \\ 0 & 0 & 1 & 0 & 0 & 0 \\ 0 & 0 & 0 & 1 & 0 & 0 \end{bmatrix} \tag{4.10}$$

Finally,

$$D_{11} = 0, \;\; D_{12} = 0, \;\; D_{21} = 0 \text{ and } \; D_{22} = 0. \tag{4.11}$$

In the above control configuration, one requires to design F, which is a static feedback gain matrix. The corresponding controller design problem is shown in Fig. 4.2 where F is having a restricted structure (in the form of a block-diagonal one) than the usual full matrix and $D = D_{21}$. The design of such a restricted feedback matrix is treated in decentralized control theory framework. We adopt the same with the objective that one has to design F such that the effect of Δw on Δz is minimized. The ILMI algorithm as given in Subsection 4.2.3 is used to design F.

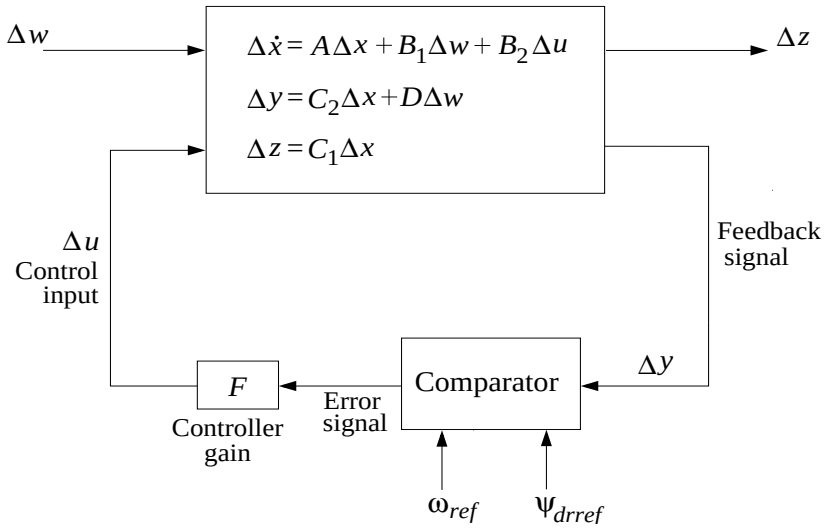

Figure 4.2: SOF controller design problem.

Outer-loop Design

For the outer-loop design, first, the closed-loop IVCIM system (6.9) is linearized around equilibrium point. The inner-loop design parameters are considered as known from previous design method. The state definitions $x_1, \cdots, x_8$ are considered same as used for the IVCIM model (3.4)-(3.11) in **Chapter 3**. The equilibrium for these states are given by (at $\delta = 0$,

$\omega_r = \omega_{ref}$):

$$\begin{aligned} x_1^e &= \frac{\psi_{drref}}{L_m},\ \ x_2^e = \frac{B_m\omega_{ref} + K_m T_L}{K_m K_t \psi_{drref}},\ \ x_3^e = \psi_{drref},\ \ x_4^e = x_5^e = 0, \\ x_6^e &= K_t \psi_{drref} x_2^e. \end{aligned} \tag{4.12}$$

Note that, x_7^e and x_8^e depends on the inner-loop control parameters and can be determined from (6.9).

Corresponding to the involvement of outer speed-loop dynamics, the load torque T_L is treated as the disturbance, therefore, the disturbance matrix (4.5) is now modified as

$$\Delta w = \begin{bmatrix} \delta\Delta x_1 & \delta\Delta x_2 & \delta\Delta x_3 & \delta\Delta x_4 & \delta\Delta x_6 & \Delta T_L \end{bmatrix}^T \tag{4.13}$$

Now, by following (4.6), (4.8), (4.12) and (4.13), the closed-loop linearized model can be written in SOF form as (4.9). The corresponding system matrices are given as

$$A = G_d + G_m \tag{4.14}$$

where $G_d = \begin{bmatrix} G_1 & G_2 \\ G_3 & \mathbf{0}_{2\times 2} \end{bmatrix}$, G_1, G_2 and G_3 are defined in (4.18),

$$G_m = \begin{bmatrix} G_{m1}^T & G_{m2}^T & G_{m3}^T \end{bmatrix}^T,\ G_{m1} = \begin{bmatrix} -cK_{pd} & \mathbf{0}_{1\times 5} & cK_{id} & 0 \end{bmatrix}, \tag{4.15}$$

$$G_{m2} = \begin{bmatrix} 0 & -cK_{pq} & \mathbf{0}_{1\times 3} & \frac{cK_{pq}}{K_t\psi_{drref}} & 0 & cK_{iq} \end{bmatrix},\ G_{m3} = \begin{bmatrix} \mathbf{0}_{6\times 8} \end{bmatrix}, \tag{4.16}$$

$$B_1 = \begin{bmatrix} 0 & \frac{L_m x_6^e}{K_t\psi_{drref}^2} & 0 & 0 & \frac{L_m x_2^e}{K_t\psi_{drref}^2} & 0 \\ -\frac{L_m x_6^e}{K_t\psi_{drref}^2} & 0 & 0 & 0 & -\frac{L_m x_1^e}{K_t\psi_{drref}^2} & 0 \\ 0 & 0 & 0 & \frac{L_m x_6^e}{K_t\psi_{drref}^2} & \frac{L_m x_4^e}{K_t\psi_{drref}^2} & 0 \\ 0 & 0 & -\frac{L_m x_6^e}{K_t\psi_{drref}^2} & 0 & -\frac{L_m x_3^e}{K_t\psi_{drref}^2} & 0 \\ 0 & 0 & 0 & 0 & 0 & \frac{K_m}{J} \\ 0 & 0 & 0 & 0 & 0 & 0 \\ 0 & 0 & 0 & 0 & 0 & 0 \\ 0 & 0 & 0 & 0 & 0 & 0 \end{bmatrix}$$

$$B_2 = \begin{bmatrix} 0 & 0 & 0 & 0 & 0 & 1 & 0 & 0 \end{bmatrix}^T,$$

$$C_1 = \begin{bmatrix} 1 & 0 & 0 & 0 & 0 & 0 & 0 & 0 \\ 0 & 1 & 0 & 0 & 0 & 0 & 0 & 0 \\ 0 & 0 & 1 & 0 & 0 & 0 & 0 & 0 \\ 0 & 0 & 0 & 1 & 0 & 0 & 0 & 0 \\ 0 & 0 & 0 & 0 & 1 & 0 & 0 & 0 \\ 0 & 0 & 0 & 0 & 0 & 1 & 0 & 0 \end{bmatrix},$$

$$C_2 = \begin{bmatrix} \zeta x_4^e & -\zeta x_3^e & -\zeta x_2^e & \zeta x_1^e & 0 & 0 & 0 & 0 \\ 0 & 0 & 0 & 0 & 0 & 0 & 1 & 0 \end{bmatrix}$$

where $\zeta = \frac{K_m K_t}{J}$.

The feedback control matrix is defined as

$$F = \begin{bmatrix} K_{p\omega} & K_{i\omega} \end{bmatrix} \tag{4.17}$$

and

$$D_{11} = 0, \;\; D_{12} = 0, \;\; D_{21} = \begin{bmatrix} 0 & 0 & 0 & 0 & 0 & \frac{K_m}{J} \\ 0 & 0 & 0 & 0 & 0 & 0 \end{bmatrix} \;\text{ and }\; D_{22} = 0.$$

Now, similar to the inner-loop design, the ILMI algorithm in Subsection 4.2.3 is used to design above outer-loop controller gain F in (4.17).

4.2.2 Concurrent Inner and Outer-Loop Design

Due to inherent coupling among the loops through the motor dynamics, any inner-loop perturbation may affect the outer-loop control performance. Such perturbation becomes more prominent in the presence of rotor resistance variation. Therefore, a concurrent design is proposed here. A decentralized controller design structure is framed for the design shown later.

Considering the disturbance input to the system is through the variations in rotor resistance δ and load torque T_L as modeled in (4.13). Now, similar to decoupled outer-loop design, using the equilibrium point (4.12), for the concurrent design, the closed-loop IVCIM system (6.9) with SOF (4.8) can be represented as (4.9). The corresponding plant matrix A is given by:

$$A = \begin{bmatrix} G_1 & G_2 \\ G_3 & \mathbf{0}_{2\times 2} \end{bmatrix} \tag{4.18}$$

where

$$G_1 = \begin{bmatrix} -a & \omega_{ref} - x_5^e + \frac{\sigma L_m x_6^e}{K_t \psi_{drref}^2} & b\sigma & b(\omega_{ref} - x_5^e) \\ x_5^e - \omega_{ref} - \frac{\sigma L_m x_6^e}{K_t \psi_{drref}^2} & -a & -b(\omega_{ref} - x_5^e) & b\sigma \\ \sigma L_m & 0 & -\sigma & \frac{\sigma L_m x_6^e}{K_t \psi_{drref}^2} \\ 0 & \sigma L_m & -\frac{\sigma L_m x_6^e}{K_t \psi_{drref}^2} & -\sigma \\ \frac{K_m K_t x_4^e}{J} & -\frac{K_m K_t x_3^e}{J} & -\frac{K_m K_t x_2^e}{J} & \frac{K_m K_t x_1^e}{J} \\ 0 & 0 & 0 & 0 \end{bmatrix},$$

$$G_2 = \begin{bmatrix} -x_2^e - bx_4^e & x_1^e + bx_3^e & 0 & 0 & -\frac{B_m}{J} & 0 \\ \frac{\sigma L_m x_2^e}{K_t \psi_{drref}^2} & -\frac{\sigma L_m x_1^e}{K_t \psi_{drref}^2} & \frac{\sigma L_m x_4^e}{K_t \psi_{drref}^2} & -\frac{\sigma L_m x_3^e}{K_t \psi_{drref}^2} & 0 & 0 \\ 0 & 0 & 0 & 0 & 0 & 0 \\ 0 & 0 & 0 & 0 & 0 & 0 \end{bmatrix}^T \text{ and}$$

$$G_3 = \begin{bmatrix} -1 & 0 & 0 & 0 & 0 & 0 \\ 0 & -1 & 0 & 0 & 0 & \frac{1}{K_t \psi_{drref}} \end{bmatrix}.$$

The corresponding disturbance and control input matrices are

$$B_1 = \begin{bmatrix} 0 & \frac{L_m x_6^e}{K_t \psi_{drref}^2} & 0 & 0 & \frac{L_m x_2^e}{K_t \psi_{drref}^2} & 0 \\ -\frac{L_m x_6^e}{K_t \psi_{drref}^2} & 0 & 0 & 0 & -\frac{L_m x_1^e}{K_t \psi_{drref}^2} & 0 \\ 0 & 0 & 0 & \frac{L_m x_6^e}{K_t \psi_{drref}^2} & \frac{L_m x_4^e}{K_t \psi_{drref}^2} & 0 \\ 0 & 0 & -\frac{L_m x_6^e}{K_t \psi_{drref}^2} & 0 & -\frac{L_m x_3^e}{K_t \psi_{drref}^2} & 0 \\ 0 & 0 & 0 & 0 & 0 & \frac{K_m}{J} \\ 0 & 0 & 0 & 0 & 0 & 0 \\ 0 & 0 & 0 & 0 & 0 & 0 \\ 0 & 0 & 0 & 0 & 0 & 0 \end{bmatrix} \text{ and} \tag{4.19}$$

$$B_2 = \begin{bmatrix} c & 0 & 0 & 0 & 0 & 0 & 0 & 0 \\ 0 & c & 0 & 0 & 0 & 0 & 0 & 0 \\ 0 & 0 & 0 & 0 & 0 & 1 & 0 & 0 \end{bmatrix}^T.$$

The PI controller is defined as

$$\Delta u = F \Delta y \tag{4.20}$$

where F contains PI gains of all the loop as

$$F = \begin{bmatrix} K_{pd} & K_{id} & 0 & 0 & 0 & 0 \\ 0 & 0 & K_{pq} & K_{iq} & 0 & 0 \\ 0 & 0 & 0 & 0 & K_{p\omega} & K_{i\omega} \end{bmatrix} \tag{4.21}$$

Further, the output matrices are

$C_1 = \begin{bmatrix} \mathbf{I}_{6\times 6} & \mathbf{0}_{6\times 2} \end{bmatrix}$ and

$$C_2 = \begin{bmatrix} -1 & 0 & 0 & 0 & 0 & 0 & 0 & 0 \\ 0 & 0 & 0 & 0 & 0 & 0 & 1 & 0 \\ 0 & -1 & 0 & 0 & 0 & \frac{1}{K_t \psi_{drref}} & 0 & 0 \\ 0 & 0 & 0 & 0 & 0 & 0 & 0 & 1 \\ \frac{K_m K_t x_4^e}{J} & -\frac{K_m K_t x_3^e}{J} & -\frac{K_m K_t x_2^e}{J} & \frac{K_m K_t x_1^e}{J} & -\frac{B_m}{J} & 0 & 0 & 0 \\ 0 & 0 & 0 & 0 & 1 & 0 & 0 & 0 \end{bmatrix} \tag{4.22}$$

Finally,

$$D_{11} = 0, \;\; D_{12} = 0, \;\; D_{21} = \begin{bmatrix} \mathbf{0}_{4\times 5} & \mathbf{0}_{4\times 1} \\ \mathbf{0}_{1\times 5} & \frac{K_m}{J} \\ \mathbf{0}_{1\times 5} & 0 \end{bmatrix} \text{ and } \; D_{22} = 0.$$

Now, the ILMI algorithm as given next is used to design F in (4.21). This yields all the controller gains at one instance of design involving the coupling effect.

4.2.3 Iterative LMI Algorithm

For the present problem, SOF based PI controller design algorithm [112, 115] is followed. Application of such PI design approach has been verified in [115] for the Load Frequency Control problem in Power System. However, it seems not been applied on IVCIM. Referred to the system dynamics (4.9), the effect of the disturbance Δw on Δz can be quantified by the ∞ norm of the closed-loop system $H(F)$ as:

$$\|H(F)\|_\infty = \max_{\Delta w(t)\neq 0} \frac{\|\Delta z(t)\|_2}{\|\Delta w(t)\|_2} \leq \rho \tag{4.23}$$

where $\|.\|_2$ represents the $\mathbf{L}_2$-norm.

In respect to the above, minimizing ρ yields a controller with good disturbance rejection behavior since ρ represents the maximum rms gain of the states $z(t)$ to the disturbance $w(t)$. For this, the below result is well known [112].

Theorem 1 *System (4.9) along with feedback gain F satisfies H_∞ performance of ρ in (4.23) if there exists a $L = L^T > 0$ satisfying*

$$\begin{bmatrix} A_c^T L + L A_c & L B_c & C_c^T \\ B_c^T L & -\rho I & D_c^T \\ C_c & D_c & -\rho I \end{bmatrix} < 0 \tag{4.24}$$

where $A_c = A + B_2 F C_2$, $B_c = B_1 + B_2 F D_{21}$, $C_c = C_1$ and D_c=0.

The above criterion satisfies H_∞ performance (4.23) for the chosen ρ and is a nonlinear matrix inequality for synthesis of F due to multiplication of unknown L and F matrices. In order to design the PI controllers embedded in F, procedures utilizing the benefits of solving LMIs with computational tools available [118] for solving them are adopted.

Note that, (4.24) can be written as:

$$\bar{A}^T \bar{L} + \bar{L}\bar{A} + (\bar{L}\bar{B}F\bar{C})^T + \bar{L}\bar{B}F\bar{C} < 0 \tag{4.25}$$

where $\bar{A} = \begin{bmatrix} A & B_1 & 0 \\ 0 & -\rho I/2 & 0 \\ C_1 & 0 & -\rho I/2 \end{bmatrix}$, $\bar{L} = \begin{bmatrix} L & 0 & 0 \\ 0 & I & 0 \\ 0 & 0 & I \end{bmatrix}$, $\bar{B} = \begin{bmatrix} B_2 \\ 0 \\ 0 \end{bmatrix}$, $\bar{C} = \begin{bmatrix} C_2 \\ D_{21} \\ 0 \end{bmatrix}^T$.

The inequality (4.25) is satisfied if one can achieve

$$\bar{A}^T \bar{L} + \bar{L}\bar{A} - \bar{L}\bar{B}\bar{B}^T\bar{L} + (\bar{B}^T\bar{L} + F\bar{C})^T(\bar{B}^T\bar{L} + F\bar{C}) < 0. \tag{4.26}$$

In (4.26), the $\bar{L}\bar{B}\bar{B}^T\bar{L}$ term is nonlinear since it involves multiplication of the unknown variable $\bar{L}$ with itself. To solve (4.26) from here, one adheres to an iterative process introducing an updating variable $\bar{X}$ in place of $\bar{L}$. For the purpose, note that, for any $\bar{X}$ the following is satisfied.

$$\bar{L}^T\bar{B}\bar{B}^T\bar{L} \geq \bar{X}^T\bar{B}\bar{B}^T\bar{L} + \bar{L}^T\bar{B}\bar{B}^T\bar{X} - \bar{X}^T\bar{B}\bar{B}^T\bar{X}. \tag{4.27}$$

Replacing (4.27) into (4.26), one gets

$$\bar{A}^T \bar{L} + \bar{L}\bar{A} - \bar{X}\bar{B}\bar{B}^T\bar{L} - \bar{L}\bar{B}\bar{B}^T\bar{X} + \bar{X}\bar{B}\bar{B}^T\bar{X} + (\bar{B}^T\bar{L} + F\bar{C})^T(\bar{B}^T\bar{L} + F\bar{C}) < 0. \tag{4.28}$$

The above can be written as an LMI on the variable $\bar{L}$ and F that satisfies (4.26) and thereby (4.24) for any $\bar{X}$. Moreover, $\bar{X} = \bar{L}$ yield the least conservative solution of (4.28) with respect to the bounding (4.27). It may further be considered that there exists a $r < 0$ for which (4.27) is equivalent to

$$\begin{aligned} &\bar{A}^T \bar{L} + \bar{L}\bar{A} - \bar{X}\bar{B}\bar{B}^T\bar{L} - \bar{L}\bar{B}\bar{B}^T\bar{X} + \bar{X}\bar{B}\bar{B}^T\bar{X} + (\bar{B}^T\bar{L} + F\bar{C})^T(\bar{B}^T\bar{L} + F\bar{C}) \\ &- r\bar{L} < 0. \end{aligned} \tag{4.29}$$

The LMI (4.29) is solved iteratively starting with an initial $\bar{X}$ and then updating $\bar{X}$ with the new $\bar{L}$ in each iteration with the relaxation introduced by the use of r. Once r reaches negative value, the feasibility of (4.28) is attained. Using schur complement, (4.29) can be

Table 4.1: Initial Parameters for Algorithm 2

Notation	Value	Notation	Value
ψ_{drref}	0.65 Wb	ω_{ref}	80 rad/sec
B_m	0 N·m/rad/s	T_L	0 N·m

written in LMI form as

$$\begin{bmatrix} \bar{A}^T\bar{L}_i + \bar{L}_i\bar{A} - \bar{X}_i\bar{B}\bar{B}^T\bar{L}_i - \bar{L}_i\bar{B}\bar{B}^T\bar{X}_i + \bar{X}_i\bar{B}\bar{B}^T\bar{X}_i - r_i\bar{L}_i & (\bar{B}^T\bar{L}_i + F\bar{C})^T \\ * & -I \end{bmatrix} < 0. \tag{4.30}$$

Finally, to start with an initial $\bar{X}$ following (4.27), one considers solving for $\bar{L}$ satisfying

$$\bar{A}^T\bar{L}^T + \bar{L}\bar{A} - \bar{L}\bar{B}\bar{B}^T\bar{L} < 0. \tag{4.31}$$

Using Schur complement, (4.31) can be written in LMI form as

$$\begin{bmatrix} \hat{L}A^T + A\hat{L} - B_2{B_2}^T & B_1 & \hat{L}{C_1}^T \\ * & -\rho I & 0 \\ * & * & -\rho I \end{bmatrix} < 0. \tag{4.32}$$

Based on the above development, the below ILMI algorithm is used to design the controller F.

Algorithm 2 Algorithm for designing controller gains

1: Obtain the values A, B_1, B_2, C_1, C_2 and D_{21} of the IVCIM model as per (4.9).
2: Set $i = 0$. Specify a $\rho > 0$ and solve for $L > 0$ satisfying (4.32).
3: Update $i = i + 1$ and $X_1 = L$.
4: Solve for $L = L^T > 0$ and F while minimizing r using gevp program in MATLAB satisfying (4.29).
5: If $r < 0$ or the iteration i reached a limit then go to next step, else go to step 4.
6: If $r < 0$ then assign $F_{final} = F$, $\rho_{final} = \rho$, reduce ρ and go to step 3. Else stop, F_{final} is the required controller gain matrix.

It may be noted that the above algorithm involves LMIs that are convex optimization problems having its local minimum as the global minimum and computational tools are available for directly solving them [118]. Although the algorithm is iterative, it is found to be easily implementable and converges to a solution in minutes for the IVCIM system solved later.

Table 4.2: Controller gains

Description	**Notation and value**
Existing design	
Speed controller [94]	$K_{p\omega} = 3.4$, $K_{i\omega} = 34$
Decoupled design	
Current controller	$K_{pd} = 1.2$, $K_{id} = 783$, $K_{pq} = 0.67$, $K_{iq} = 910$
Speed controller	$K_{p\omega} = 0.18$, $K_{i\omega} = 0.2$
Proposed concurrent design	
Current controller	$K_{pd} = 128.5$, $K_{id} = 1116$, $K_{pq} = 88$, $K_{iq} = 1283$
Speed controller	$K_{p\omega} = 0.8$, $K_{i\omega} = 2.8$

4.3 Simulation Results

For validation of the present design approach, an IVCIM as shown in Fig. 3.8 with the machine parameters given in Table 3.4 is considered. First, the speed-loop (outer-loop) controller gains are designed using existing approach. The design of [94] based on robust stability margin is followed. A damping ratio of $\zeta = 1$ and natural frequency of $\omega_n = 20$ rad/sec are chosen for the design. This yields the gains as $K_{p\omega} = 3.4$ and $K_{i\omega} = 34$.

4.3.1 Decoupled Design

For the decoupled design, the equilibrium point is chosen corresponding to the references as given in Table 4.1. Then A, B_1, B_2, C_1, C_2, D_{21} are obtained following Algorithm 2. For the inner-loop design, ρ is chosen as 1. After 20 iterations, the ILMI algorithm converges and yields the controller gains. These gains are employed into the outer loop design. For the outer loop design, initial value of ρ is chosen as 20. After 80 iterations, the algorithm yields the speed-loop gains. Both the existing and the decoupled design gains are shown in Table 4.2.

4.3.2 Proposed Design

For deigning both the controller gains concurrently, the same ILMI algorithm is used with ρ is taken as 4.5. The algorithm converges after 90 iterations and the corresponding gains are given in Table 4.2. The controllers are obtained as:

$$K_d(s) = 128\left(1 + \frac{8.71}{s}\right), K_q(s) = 88\left(1 + \frac{14.57}{s}\right), K_\omega(s) = 0.8\left(1 + \frac{3.5}{s}\right).$$

4.3.3 Bandwidth Comparison

The badwidth analysis of the designed controller gains is carried out using the bode plot. These plots are obtained using the transfer function model of the IVCIM system. For this, inner current and outer speed loop transfer functions are determined individually. The inner-loop transfer function is determined by following [1] as $C(s)\frac{i_{ds}(s)}{v_{ds}(s)} = C(s)\frac{i_{qs}(s)}{v_{qs}(s)}$ for d and q component of the stator currents. Here $C(s)$ is the PI controller and $\frac{i_{ds}(s)}{v_{ds}(s)} = \frac{i_{qs}(s)}{v_{qs}(s)} = \frac{1}{R_{eq}+sL_{eq}}$, $R_{eq} = R_s + R_r$ and $L_{eq} = L_{ls} + L_{lr}//L_m$. Bode plot for the decoupled inner-and outer speed-loop PI controller design is shown in Fig. 4.3(a)-(b). The current control loop bandwidth for i_{ds} and i_{qs} are obtained as $\simeq$ 132 rad/sec and $\simeq$ 150 rad/sec, respectively. For the speed-loop bandwidth, the transfer function is considered as $C(s)\frac{\omega_r(s)}{T_{re}(s)}$ [3]. Here $\frac{\omega_r(s)}{T_{re}(s)} = \frac{K_m}{Js}$ is the open-loop transfer function neglecting current-loop dynamics. The decoupled designed speed-loop bandwidth is obtained as 6.2 rad/sec. The bode plot for the inner-loop controller using the proposed concurrent design is shown in Fig. 4.4. It depicts a comparatively higher bandwidth as $\simeq$ 6000 rad/sec and $\simeq$ 4130 rad/sec for the i_{ds} and i_{qs}, respectively. An outer loop bandwidth comparison between the proposed and the design of [94] is shown using bode plot in Fig. 4.5. The speed-loop bandwidth as per [94] is obtained as $\simeq$ 110 rad/sec. While the proposed design (being a concurrent one) yields a bandwidth of 25 rad/sec.

4.3.4 Robustness Evaluation

Since the proposed concurrent design accounts for robustness as well, the robust performance is studied through simulation. First, IVCIM model is simulated using the controllers obtained through decoupled design. The corresponding results are shown in Fig. 4.6. As T_L is changed to 6.5 N·m, due to low bandwidth for both the inner-and outer-loop controllers, the shoot as well as the settling time are quite high for both stator currents i_{ds}, i_{qs} and ω_r.

For comparison of both techniques (proposed concurrent and existing [94]), the inner-loop gains are kept as same as obtained from the proposed design. A comparison of the two approaches on speed variation is shown in Fig. 4.7. A step change in ω_{ref} (100-150 rad/sec) is applied at 5 sec. The corresponding IM dynamics behavior with existing design is shown in Fig. 4.7(a)-(c). Since the speed-loop controller gains with the existing one yields very high bandwidth, instability is observed. A similar behavior of such designs has also been observed in [3]. On the other hand, with the proposed controller gains, a smooth transient is observed in Fig. 4.7(d)-(f). From Fig. 4.7, it is depicted that with the proposed design, stator currents i_{ds}, i_{qs} and motor speed ω_r represent better performance than the existing one.

Next, the effect of T_L variation is evaluated. Since the existing design shows instability, T_L perturbation performance is only tested with the proposed designed gains. A variation in σ is considered as $\delta = 0.2\sigma$, which is within the range of $-0.5\sigma < \delta < 0.41\sigma$ in order to

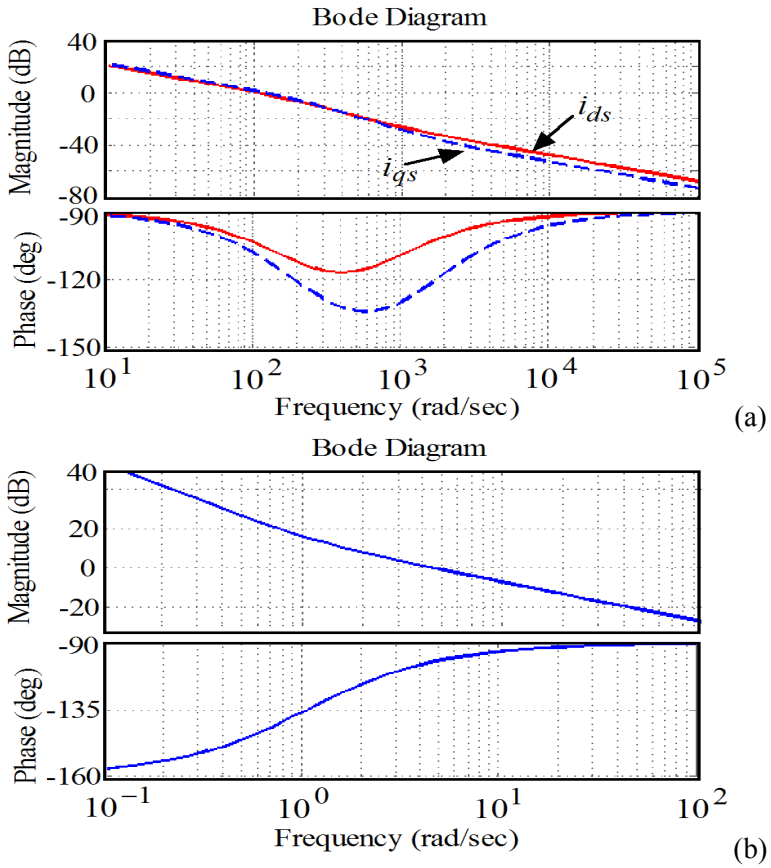

Figure 4.3: Bode bandwidth plot for decoupled inner and outer-loop controllers: (a) Inner-loop. (b) Outer-loop.

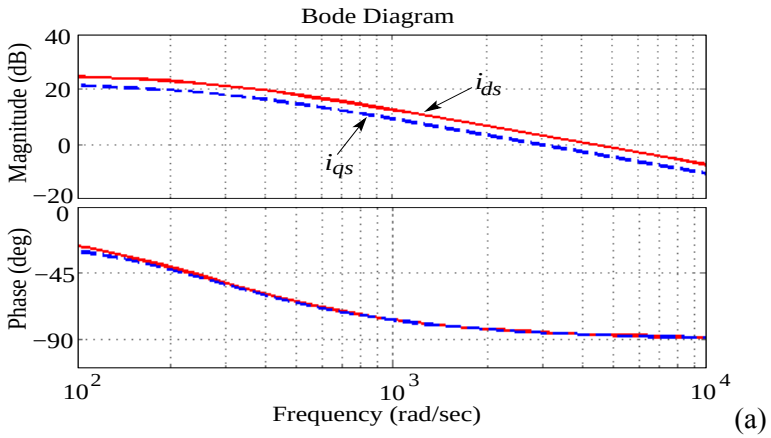

Figure 4.4: Bode bandwidth plot for concurrent inner-loop controller.

maintain minimum-phase condition following [3]. In steady-state, a step $T_L = 6.5$ N·m is applied at 5 sec. The corresponding i_{ds}, i_{qs} and ω_r are shown in Fig. 4.8. It is observed that, for both $\delta = 0$ and $\delta = 0.2\sigma$, transient response (regarding settling time, undershoot and overshoot) in stator currents and motor speed are almost same, which depicts the robustness property that the proposed design inherits.

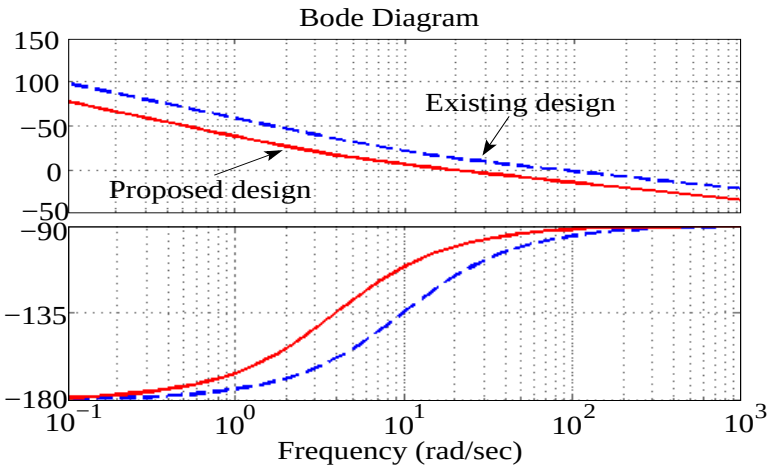

Figure 4.5: Bode bandwidth plot for concurrent outer-loop controller.

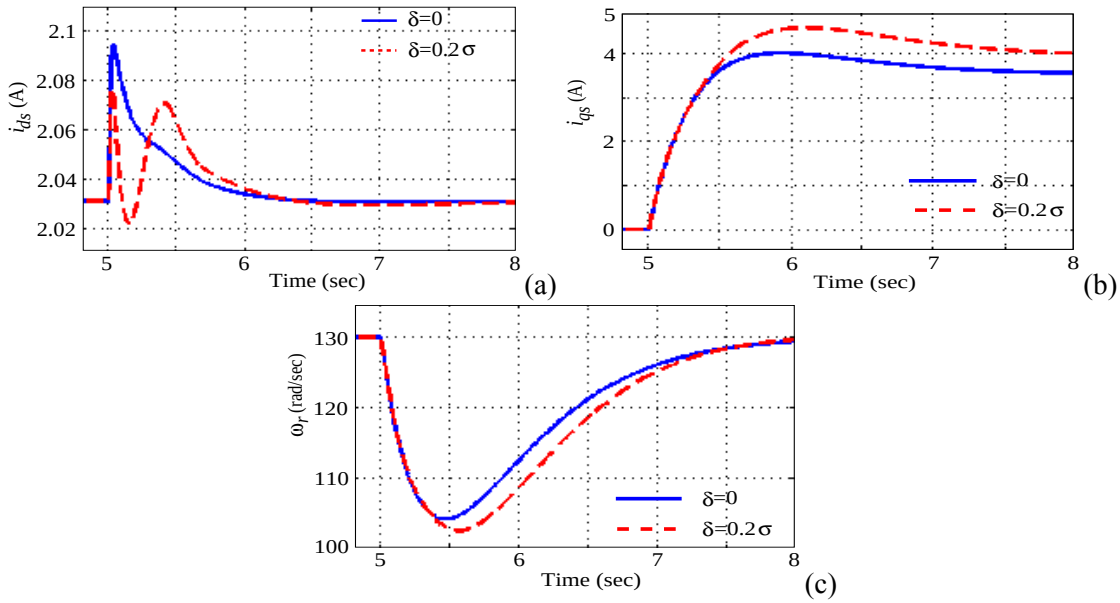

Figure 4.6: Decoupled design simulation results for step change in T_L. (a) i_{ds}. (b) i_{qs}. (c) ω_r.

4.4 Experimental Results

For experimental validation, the same motor as described in Section 4.3 is used. Experiment is first carried with the PI gains as obtained from the decoupled design. The corresponding results for T_L variation is shown in Fig. 4.9 at $\delta = 0$. As T_L is changed in step of about 6.5 N·m at $\omega_r = 130$ rad/sec, a high shoot occurs in both the currents and the ω_r. Also, these states return to steady-state with a large settling time. The magnitude of the shoot and the settling time increases with $\delta = 0.2\sigma$, as observed in Fig. 4.10. Such behavior corroborate the simulation results. Next, experiment is carried out with the proposed design. A T_L of about 6.5 N·m is applied in steady-state ($\omega_r = 130$ rad/sec). The corresponding ω_r and i_{qs}

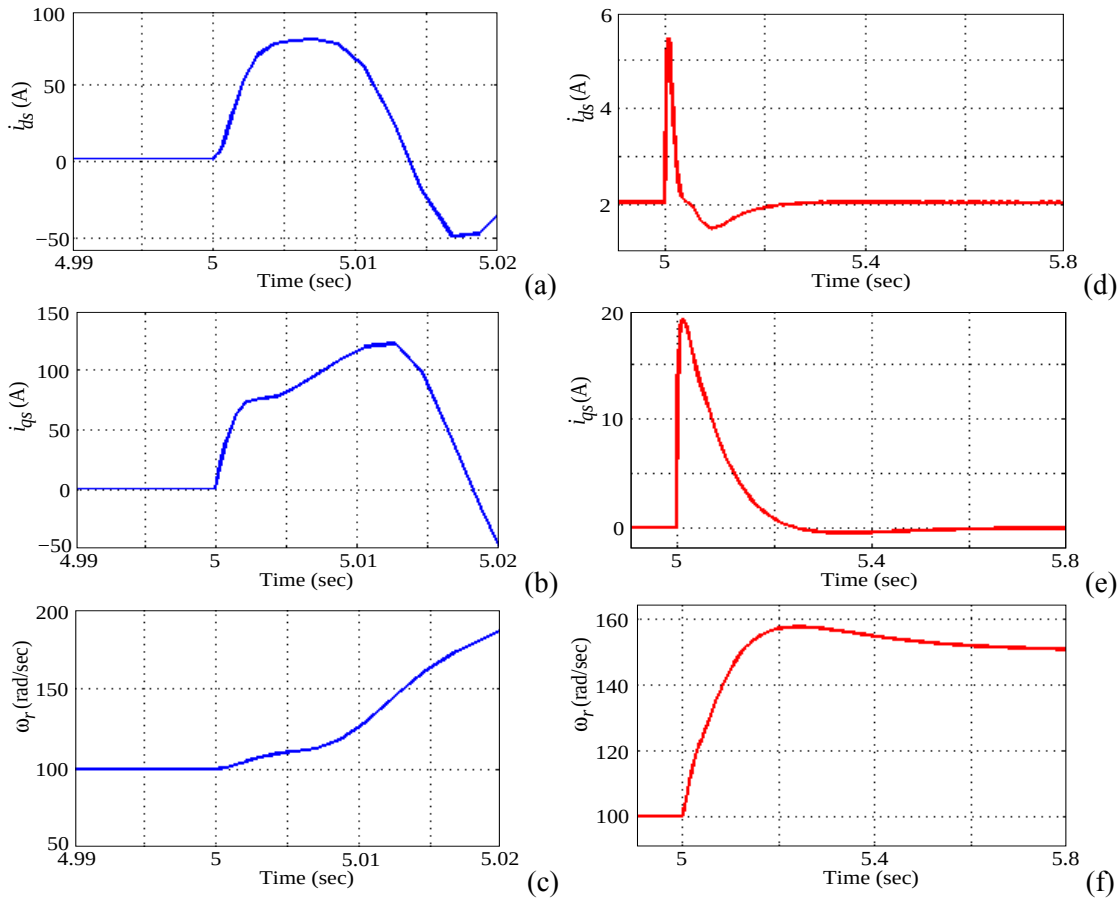

Figure 4.7: Comparison between existing and proposed design for step change in ω_{ref} at $\delta = 0$: (a)-(c) existing design, (d)-(f) proposed design.

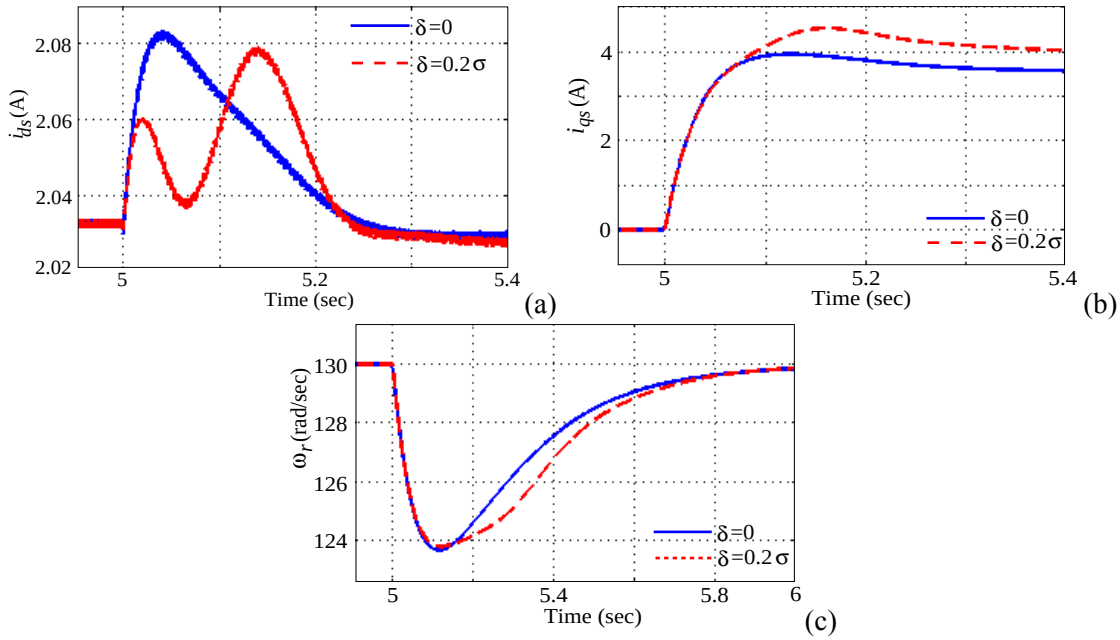

Figure 4.8: Variation of motor speed and stator currents for step change in $T_L = 6.5$ N·m at $\omega_{ref} = 130$ rad/sec for proposed design: (a) i_{ds}. (b) i_{qs}. (c) ω_r.

variation are shown in Fig. 4.11(a)-(b). It is observed that, ω_r and stator currents as shown in Fig. 4.11(a) have smoother transient as compared to the decoupled design. Moreover, at $\delta = 0.2\sigma$, ω_r, i_{ds} and i_{qs} transient performance is similar to $\delta = 0$ as shown in Fig. 4.11(b).

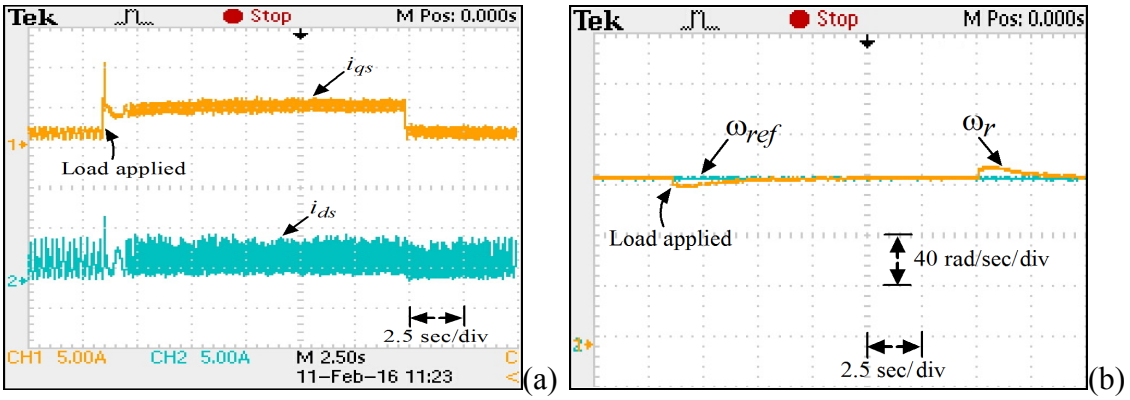

Figure 4.9: Experimental result with decoupled design for variation in T_L at $\omega_{ref} = 130$ rad/sec at $\delta = 0$: (a) Stator currents. (b) Motor speed ω_r.

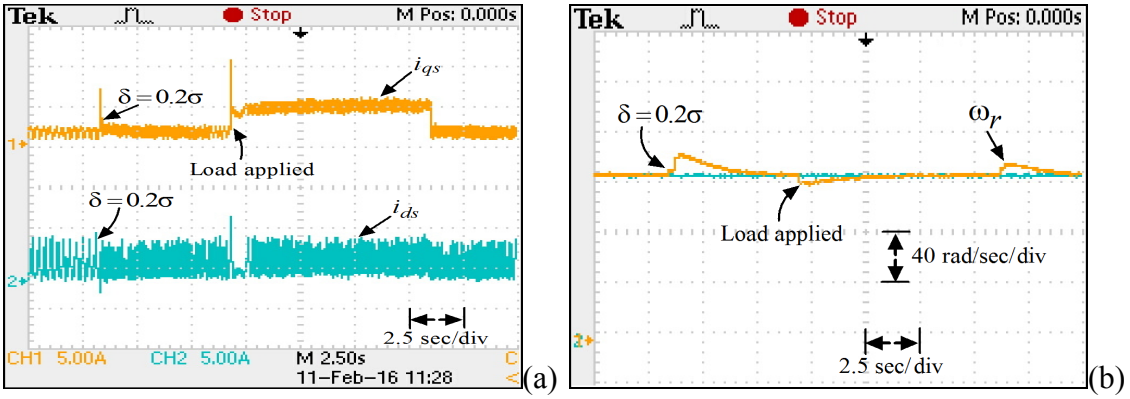

Figure 4.10: Experimental result with decoupled design for variation in T_L at $\omega_{ref} = 130$ rad/sec at $\delta = 0.2\sigma$: (a) Stator currents. (b) Motor speed ω_r.

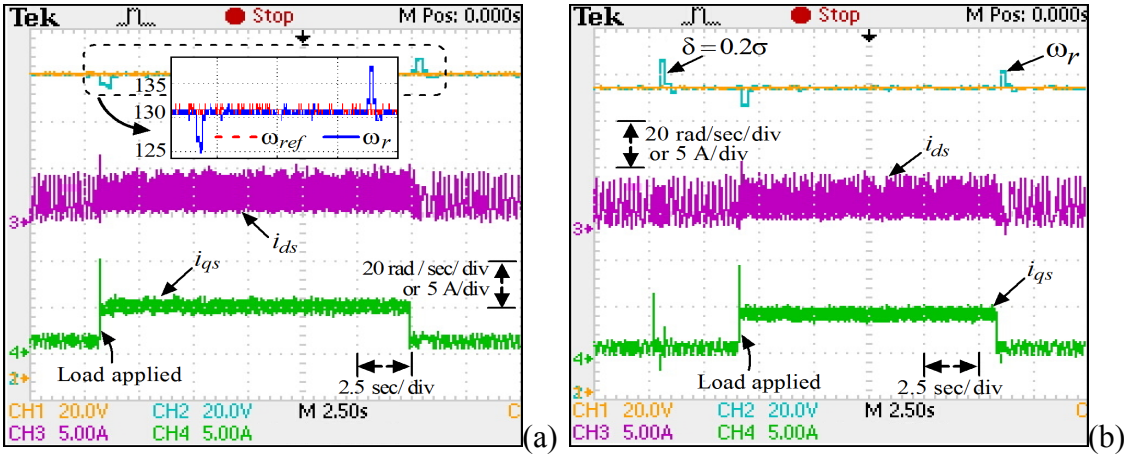

Figure 4.11: Experimental result with proposed concurrent design for variation in T_L at $\omega_{ref} = 130$ rad/sec: (a) $\delta = 0$. (b) $\delta = 0.2\sigma$.

Next, the speed tracking performance of existing [3, 94] and the proposed designs are evaluated experimentally. First, the experiment is carried with the design of [94]. Owing to instability in simulation for the design of [94], the motor is started using the proposed speed-loop gains. As motor reached to $\omega_{ref} = 130$ rad/sec, the proposed gains are changed to the gains corresponding to [94] using variable array tool in dSPACE. As shown in Fig. 4.12(a), initially ω_{ref} is changed in small step from 130 to 150 rad/sec. Corresponding to this change, ω_r and i_{qs} oscillate with large magnitude as observed in Fig. 4.12. Further, as ω_{ref} is reduced to 100 rad/sec, large overshoots in i_{ds} and i_{qs} (Fig. 4.12(b)) are observed and motoring operation is stalled which shows poor tracking performance. Here, existing design lacks the robustness due to high bandwidth (110 rad/sec) control action. For the proposed design approach, ω_{ref} is varied in large step from $100 \rightarrow 150 \rightarrow 100$ rad/sec. The corresponding ω_r variation in Fig. 4.13(a)-(b) shows comparatively smoother tracking for $\delta = 0$ as well as for $\delta = 0.2\sigma$. Comparing Fig. 4.12 and Fig. 4.13(a)-(b), it is observed that the proposed design provides improved robust performance than the existing design approach.

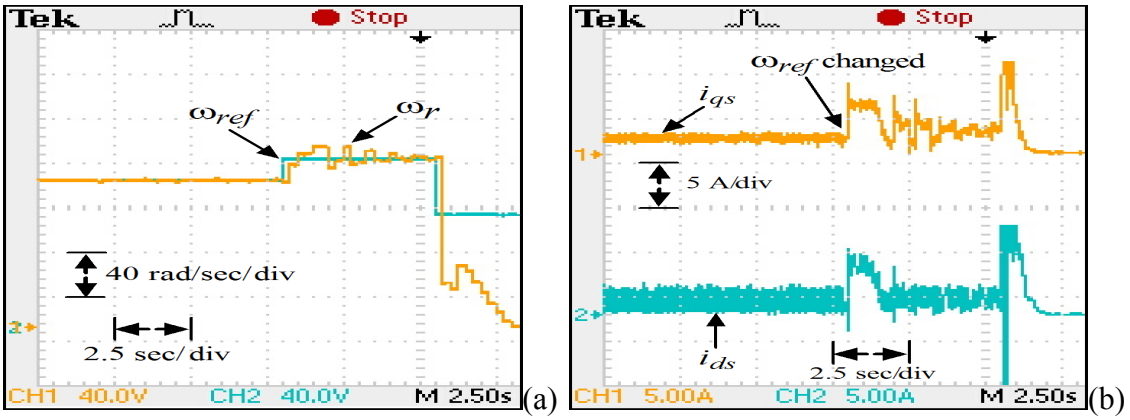

Figure 4.12: Experimental result with existing design for variation in ω_{ref} at $\delta = 0$: (a) Motor speed ω_r. (b) Stator currents i_{ds} and i_{qs}.

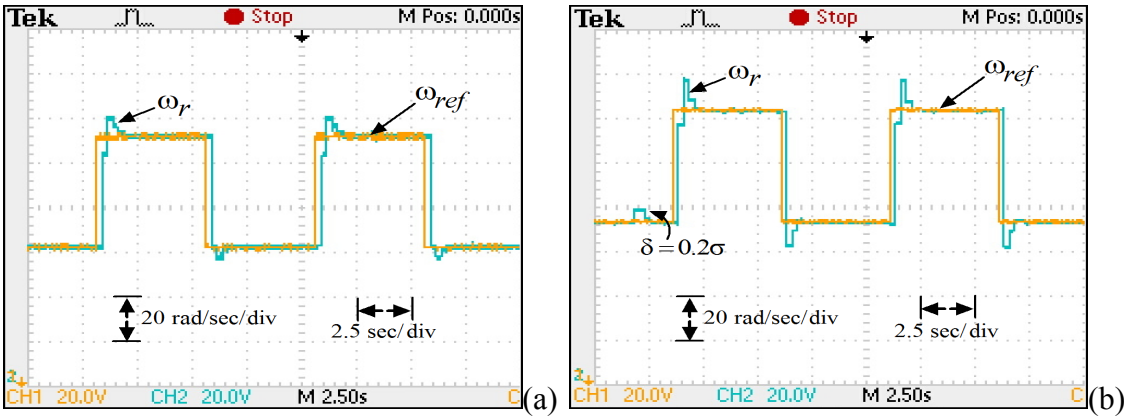

Figure 4.13: Experimental result of ω_r with proposed design for variation in ω_{ref}: (a) $\delta = 0$, (b) $\delta = 0.2\sigma$.

Further, the IM is controlled using the speed-loop controller [3] and the stator currents are regulated using the proposed PI controller that could not start the motor. Hence, first, motor is started using the proposed speed-loop controller and then, at steady-state, it is switched to the existing controller $C_{\omega}(s) = \frac{2(s+90)^2(s+22)}{s(s+210)(s+87)}$ [3]. The IM becomes unstable with this design as observed in Fig. 4.14(a). Whereas, for the proposed design (bandwidth of 25 rad/sec in the speed-loop), a smoother response is observed in Fig. 4.14(b). Further, IM is controlled using lower bandwidth speed-loop gains $K_{p\omega} = 0.5$ and $K_{i\omega} = 1.5$ (bandwidth of 16.5 rad/sec in the speed-loop) and same ω_{ref} variation is applied. The corresponding ω_r, i_{ds} and i_{qs} response are shown in Fig. 4.14(c). It is observed that for these gains, settling time and overshoot for ω_r and i_{ds} are higher than the proposed design. Next, motor is controlled using higher bandwidth gains $K_{p\omega} = 1$ and $K_{i\omega} = 3$ (bandwidth of 33 rad/sec) and the corresponding response is shown in Fig. 4.14(d). It is observed that settling time and overshoot for ω_r are better than the proposed design. However, overshoot for both d and q-axis currents is higher than the proposed one.

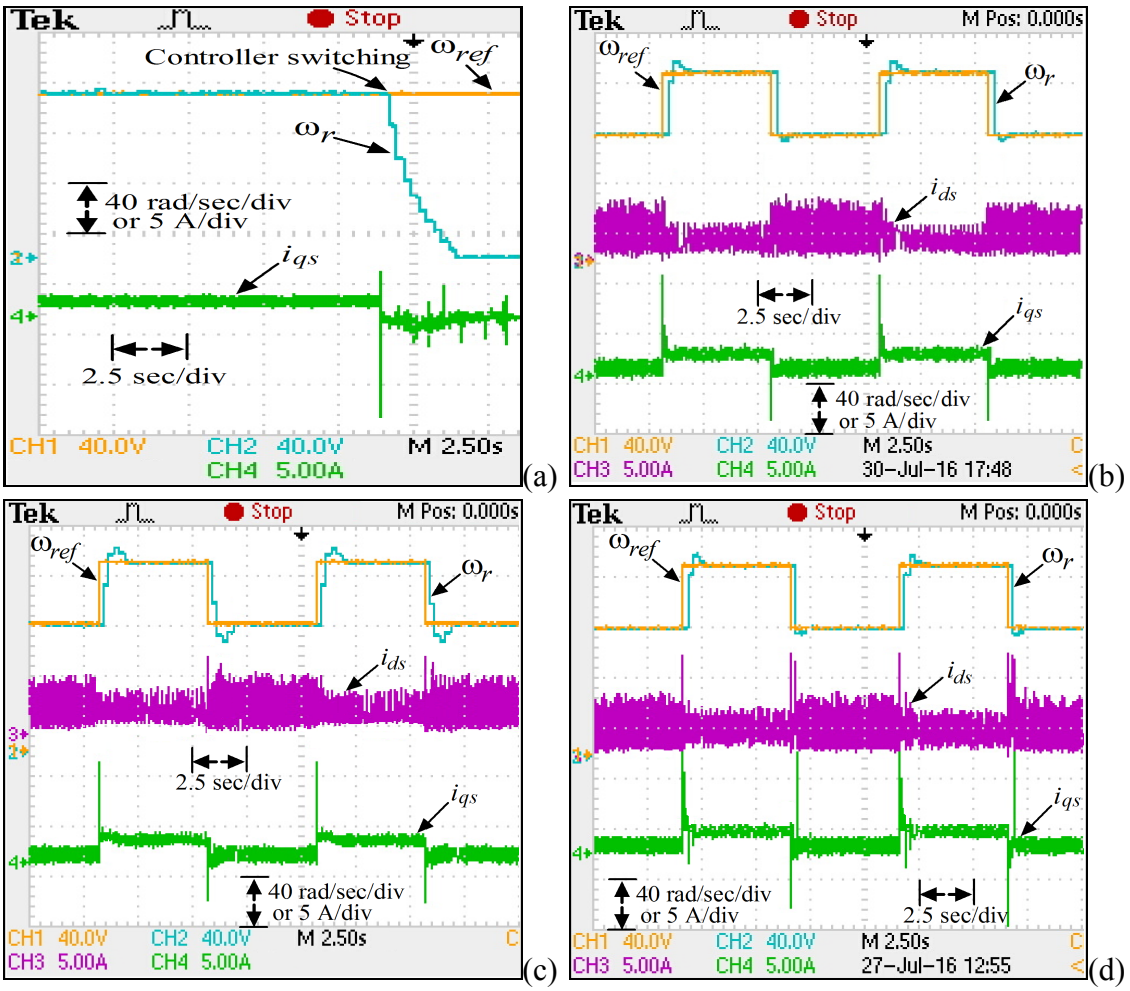

Figure 4.14: Experimental results for variation in ω_{ref} from 100 $\rightarrow$ 150 $\rightarrow$ 100 rad/sec at $\delta = 0$: (a) Existing design of [3]. (b) Proposed design. (c) $K_{p\omega} = 0.5$ and $K_{i\omega} = 1.5$. (d) $K_{p\omega} = 1$ and $K_{i\omega} = 3$.

The tracking performance of i_{ds} and i_{qs} with variation in T_L and ω_{ref} (100 $\rightarrow$ 150 $\rightarrow$ 100 rad/sec) is shown in Fig. 4.15(a)-(b). Both currents shows smooth tracking performance with the proposed design.

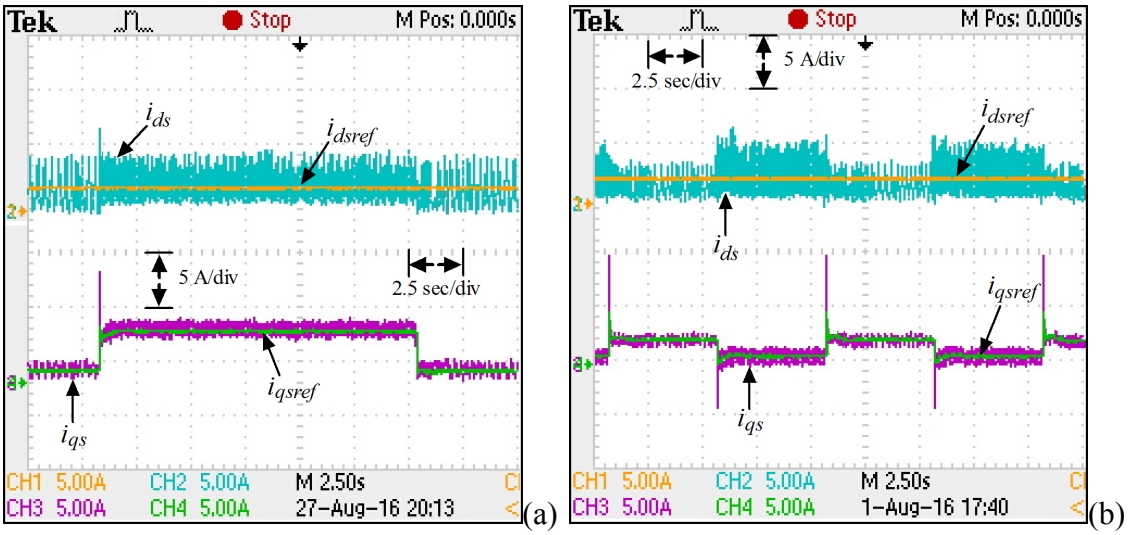

Figure 4.15: Experimental result of current tracking performance for change in: (a) T_L. (b) ω_{ref}.

4.5 Chapter Summary

In this chapter, a concurrent robust PI controller has been designed for the multiple-input and multiple-output IVCIM system. The controller design problem is framed in static output feedback framework in which rotor resistance variation and load torque are considered as disturbances. The combination of robust H_∞ control and ILMI technique is used to design the PI controller gains. The comparison of simulation and experimental results indicates the superior robust performance for the proposed concurrent design.

The stator current dynamics are coupled to each other such that variation in one component affect the other one as observed in Fig. 4.11(a). On the other hand, the bandwidth of the current-control loop should be high enough for faster response, however, the same may increase the coupling (fast i_{qs} response increases transient in i_{ds} [119]). This coupling degrade the smoothness of the torque response of the motor. It can be minimized to certain extant by proper regulation of inner control gains, which requires a systematic design procedure. In the next chapter, the inner-loop PI controllers are designed to minimize the coupling between stator currents subjected to load torque variations.

Chapter 5

Decoupling PI Controller Design for IVCIM

5.1 Introduction

To generate the instantaneous torque using IVC scheme [120], two current components (the direct and quadrature ones) are to be controlled independently. Although SRC is simpler than the SRFC one, the latter one is preferred since it operates on DC quantities and zero steady-state error. These benefits can be achieved if the regulator gains are chosen efficiently [1]. For such regulation, the reference quadrature current is given by the outer speed-loop, which is realized by linear, intelligent control techniques and nonlinear methods [3, 100, 121–124]. However, these components are inherently coupled through the motor dynamics which affects the IM torque response.

The coupled flux and torque dynamics behavior along with rotor resistance variation effect have been studied in [125]. The severity of this coupling on motoring operation depends on the control application. During the low-speed IM operation, the coupling effect can be neglected. Erstwhile, for high-speed operation, fast torque response is difficult to achieve without proper decoupling [126]. For overcoming the coupling effect, many decoupling techniques have been discussed. A complex vector synchronous frame proportional-integral (PI) controller design has been proposed in [127] to enhance the performance of synchronous PI controller. Specifically, parameter variation causes errors in the estimated flux that may lead to the reduction of the torque performance. To overcome this, a modified decoupling control has been proposed in [128]. Additional PI controller has been used to perform the decoupling in [129]. An internal-model-control (IMC) based decoupling has also been reported in [119], where additional integrator dynamics has been used to minimize the coupling. Further, a dynamic controller structure for the current controllers have been used in [126] to achieve decoupling. The rotor time-constant estimation based decoupling has been suggested in [130]. A new adaptive observer based speed estimation technique has been proposed in [131] that may be used for decoupling. Multivariable PI based decoupling scheme has been discussed in [132]. Here, similar to the IMC based decoupling [119], inclusion of integrators have been used for mitigating

the coupling. Despite these modifications, the feedforward decoupling method [21] is still preferred due to its straight-forwardness and faster decoupling ability.

Apart from the above linear decoupling schemes, a sliding mode control based decoupling has been developed in [4, 133]. Due to the lack of antiwindup capability in [4], the proposed controller may saturate at high speed limiting its application to low load conditions for which the coupling is itself weak. Also, it requires low-pass filters to remove the chattering effect. The decoupling is also been attempted in sensorless control scheme [134]. A nonlinear observer is proposed to estimate the motor speed, which is used to compensate the speed dependent cross-coupled terms. A modified IVC scheme based decoupling for current source IM drive has been given in [45]. Besides these decoupling methods, energy efficient model based control (MBC) has been discussed in [135] to improve the torque performance. In this work, the MBC dynamical behavior for load transition has been analyzed in detail and new control strategies have been proposed. Modified PI controller based decoupling methods have been developed in [119, 127, 129, 132]. However, all these methods incorporate additional dynamics and/or induce complexity in the conventional indirect vector controlled induction motor (IVCIM) system. Moreover, the tuning of the PI controller, otherwise used for current regulations, also has an impact on the coupling [4]. Despite the fact that such tuning has limited scope to minimize coupling. However, due to its simplicity and classical performance, it is considered as a better method for decoupling rather than introducing additional dynamics. Typically, for designing a PI controller, frequency response (Bode plot) method is considered as simple. However, the robustness of the system is difficult to assess using such method [136].

The present chapter is on SOF based PI design of the speed as well as the current controllers to achieve decouple transient performance. By this method, the same classical IVCIM structure is retained. The following contributions are made in this chapter: (i) Sensitivity of stator currents on inner-loop controller gains is determined. (ii) The decoupling effect is formulated as a performance criterion for speed and current-loop controller design. (iii) An MIMO SOF based closed-loop structure is formulated for the linearized model of the IVCIM. (iv) An iterative linear matrix inequality (ILMI) based controller design technique is applied to design the PI gains. (v) Simulation and experimental results are presented that corroborates the effectiveness of the proposed controller design technique as compared to the conventional feedforward decoupling one.

The chapter is organized as follows: The classical feedforward decoupler and sensitivity of stator currents are discussed in Section 5.3. Section 5.4 shows the formulation of the coupling minimization problem. Comparison of the proposed method with feedforward one through simulation and experimental results is given in Section 5.5. Finally, conclusions of this chapter are pointed out in Section 5.6.

5.2 System Under Study

The IVCIM system as shown in Fig. 3.8 and model described in (6.9) is considered here. The stator currents i_{ds} (x_1) and i_{qs} (x_2) are coupled to each other and hence, for any variation in respective currents, torque output of the IM is affected. Therefore, a feedforward decoupler is used to compensate the coupled dynamics. However, it introduces additional burden in terms of signal processing and requires exact knowledge of motor parameters. For overcoming this limitation, in this Chapter, a PI controller design scheme is introduced, which yields suitable inner-loop gains that minimizes coupling of the stator currents on load torque variations. This PI design does not require any additional signal processing and arrangements and hence provides an alternative and simple approach to get smoother torque response.

5.3 Inner-loop Feedforward Decoupler

In order to elaborate the coupling problem, consider rewriting the stator current dynamics following (6.9) at $\delta = 0$ as:

$$\left.\begin{aligned}\dot{x}_1 =& -ax_1 + [\omega_{ref} - x_5 + \sigma L_m (K_t \psi_{drref}^2)^{-1} x_6] x_2 + b\sigma x_3 + b(\omega_{ref} - x_5) x_4 \\ &+ c v_{ds} \\ \dot{x}_2 =& -[\omega_{ref} - x_5 + \sigma L_m (K_t \psi_{drref}^2)^{-1} x_6] x_1 - ax_2 - b(\omega_{ref} - x_5) x_3 + b\sigma x_4 \\ &+ c v_{qs}\end{aligned}\right\} \tag{5.1}$$

In the above, both i_{ds} and i_{qs} are dependent on each other, additionally on ψ_{dr}, ψ_{qr} and ω_r. These are coupled through the remaining system dynamics. However, for obtaining a torque response similar to a DC motor, the flux, and torque components of currents are required to be decoupled while regulating the respective currents.

The torque performance can be improved by compensating the coupled terms. However, the perfect compensation of all the connected components requires an accurate update knowledge of the motor parameters. This is almost impossible in practice since induction motor parameters are known to have variations during operation, e.g., the rotor resistance variation [7]. In [126], it has been observed that (i) $\omega_e i_{ds}$ and $\omega_e i_{qs}$ are the dominating components in the respective currents, and (ii) the coupling effect increases as motor speed increases. So, either by removing or minimizing these dominating components, the effect of coupling phenomenon can be reduced. One way to achieve such reduction in coupling is, by introducing a supplementary feedforward controller to the current controller output as shown in Fig. 5.1(a) [103]. In this, a direct feedforward compensation v_{ds}^{comp} and v_{qs}^{comp} corresponding to the dominating components are used.

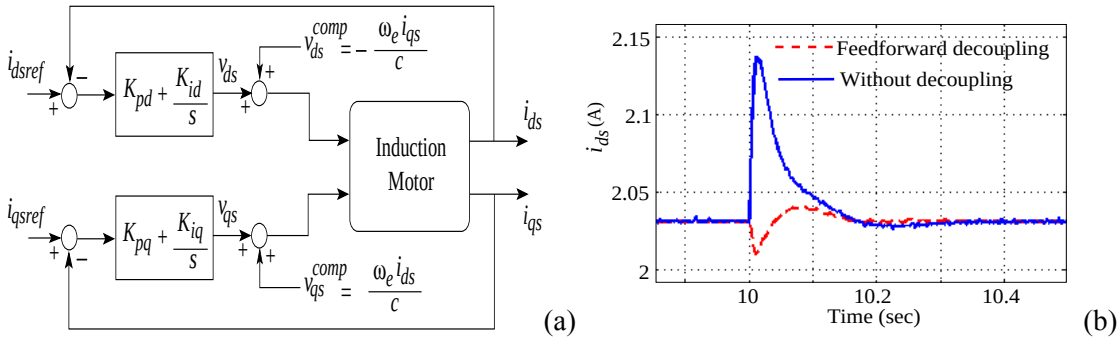

Figure 5.1: (a) Feedforward decoupling of inner-loop. (b) Behavior of i_{ds} for feedforward decoupling scheme.

The compensation voltage signals are:

$$v_{ds}^{comp} = -\frac{\omega_e i_{qs}}{c} = -\frac{x_2[\omega_{ref} - x_5 + \sigma L_m (K_t \psi_{drref}^2)^{-1} x_6]}{c} \tag{5.2}$$

$$v_{qs}^{comp} = \frac{\omega_e i_{ds}}{c} = \frac{x_1[\omega_{ref} - x_5 + \sigma L_m (K_t \psi_{drref}^2)^{-1} x_6]}{c}. \tag{5.3}$$

The effect of such decoupling method for the IM (Parameters are given in Table 3.4) is shown in Fig. 5.1(b). This can be seen that for a change in T_L (6.5 N·m applied at 10 sec), the effect in i_{ds} is considerably reduced by the decoupler.

Note that, the above result is obtained while considering same speed and current-loop controller gains. However, for a different set of these controller gains, the performance of the decoupling scheme varies. Moreover, it may be possible to improve the decoupling by suitable choice of the regulatory PI gains. Since feedforward decoupling scheme introduces complexity in IVCIM and it is more susceptible to parameter variations [126], an alternate method is proposed in this work.

5.3.1 Decoupler Sensitivity

Current controller tuning effect

For IVCIM, the coupling is primarily affected by inner-loop controller tuning. Since cross-couplings exist between the two current loops, controller tuning for the d-axis stator current may affect the q-axis one and vice versa. The sensitivity of the currents with respect to the cross-controller gains are studied here.

The sensitivity expression is determined following procedure in [11]. For the purpose, first, the current-loop integrators and outer speed-loop dynamics are neglected and the linearized model is obtained by replacing $x = x^e + \Delta x$ in (6.9)($\delta = 0$). The linearized closed-loop IVCIM model in SISO form (only i_{ds} as the output) can be written as:

$$\left.\begin{aligned} \Delta \dot{x}_{1-4} &= G \Delta x_{1-4} \\ \Delta y_1 &= C \Delta x_{1-4} \end{aligned}\right\} \tag{5.4}$$

where $\Delta x_{1-4} = \begin{bmatrix}\Delta x_1 & \Delta x_2 & \Delta x_3 & \Delta x_4\end{bmatrix}^T$, $G = \begin{bmatrix} g_{11} & \cdots & g_{14} \\ \vdots & \vdots & \vdots \\ g_{41} & \cdots & g_{44}\end{bmatrix}$, $g_{11} = -a - cK_{pd}$, $g_{12} = \omega_e$, $g_{13} = b\sigma$, $g_{14} = b\omega_{ref}$, $g_{21} = -\omega_e$, $g_{22} = -a - cK_{pq}$, $g_{23} = -b\omega_{ref}$, $g_{24} = b\sigma$, $g_{31} = \sigma L_m$, $g_{32} = 0$, $g_{33} = -\sigma$, $g_{34} = \omega_{sl}$, $g_{41} = 0$, $g_{42} = \sigma L_m$, $g_{43} = -\omega_{sl}$, $g_{44} = -\sigma$, $C = \begin{bmatrix}1 & 0 & 0 & 0\end{bmatrix}$.
With a perturbation ΔK_{pq} in K_{pq}, the above can be written as

$$\left.\begin{aligned}\Delta\dot{x}_{1-4} &= G\Delta x_{1-4} + \Delta G x^e_{1-4} \\ \Delta y_1 &= C\Delta x_{1-4}\end{aligned}\right\} \tag{5.5}$$

where ΔG represents perturbed system matrix as $\Delta G = \begin{bmatrix} M & \mathbf{0}_{2\times2} \\ \mathbf{0}_{2\times2} & \mathbf{0}_{2\times2}\end{bmatrix}\Delta K_{pq}$, ΔK_{pq} is the variation in K_{pq}, $x^e_{1-4} = \begin{bmatrix}x^e_1 & x^e_2 & x^e_3 & x^e_4\end{bmatrix}^T$, $M = \begin{bmatrix}0 & 0 \\ 0 & -c\end{bmatrix}$.

Now, the sensitivity function for Δi_{ds} can be derived from (5.5) as

$$\frac{\Delta i_{ds}}{\Delta K_{pq}} = -\frac{ch_{12}i^e_{qs}}{|Q|} \tag{5.6}$$

where $h_{12} = g_{12}g_{34}g_{43} + g_{13}g_{32}g_{44} + g_{14}g_{33}g_{42} - g_{12}g_{33}g_{44}$
$- g_{13}g_{34}g_{42} - g_{14}g_{32}g_{43}$, $Q = sI - G$.

Similarly, considering the dynamics involving only i_{qs} as the output, the sensitivity function for Δi_{qs} can be determined as

$$\frac{\Delta i_{qs}}{\Delta K_{pd}} = -\frac{ch_{21}i^e_{ds}}{|Q|}, \tag{5.7}$$

where ΔK_{pd} is the variation in K_{pd}, $h_{21} = g_{21}g_{34}g_{43} + g_{23}g_{31}g_{44} + g_{24}g_{33}g_{41} - g_{21}g_{33}g_{44}$
$- g_{23}g_{34}g_{41} - g_{24}g_{31}g_{43}$.

The above sensitivities are studied here for an IM with the parameters given in Table 3.4. For evaluating (5.6), the equilibrium point is determined at $T_L = 5$ N·m (chosen arbitrarily) and $\omega_e \simeq \omega_r$=80 rad/sec. These sensitivity functions are analyzed with the magnitude plot as shown in Fig. 5.2(a). It is observed that the current perturbations can be minimized by tuning the controller with high K_{pd} and K_{pq}. However, due to non-ideality, noises and delay in physical implementation, higher gains may actuate oscillations of large magnitude or instability, hence a systematic design is required. The sensitivity of i_{ds} with feedforward decoupler is shown in Fig. 5.2(b). For this, the equilibrium point is determined at $T_L = 5$ N·m and with $\omega_e = 0$ (perfect compensation is considered). It is observed that high controller gains reduce the current perturbations, however, sensitivity is slightly lower with this decoupling as compared to the without decoupler case. The sensitivity of i_{ds} (without

decoupling) with variation in frequency is shown in Fig. 5.3(a). It is observed that sensitivity is high at low frequency ($\omega = 0.1$ rad/sec). As frequency reaches 20 rad/sec, a small peak is observed due to the cancellation of motor dynamics [119]. Furthermore, it is reduced with increasing frequency and K_{pd}, K_{pq}.

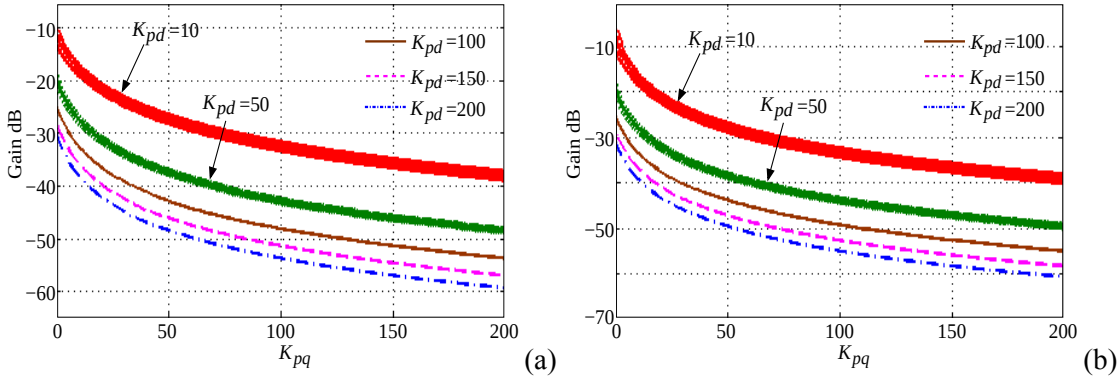

Figure 5.2: Sensitivity of i_{ds} on controller gains: (a) Without decoupler. (b) With decoupler.

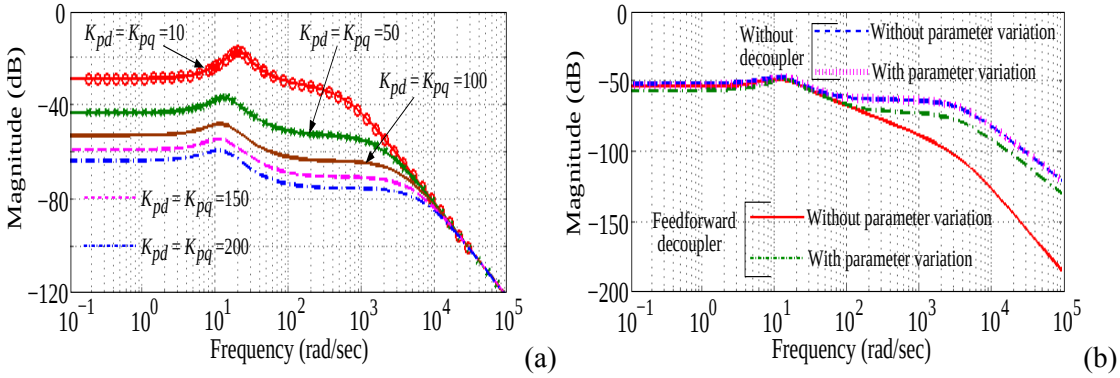

Figure 5.3: Sensitivity of i_{ds} with variation in frequency at $\omega_e = 80$ rad/sec: (a) Varying K_{pd}, K_{pq}. (b) $K_{pd} = K_{pq} = 100$ and 35% overestimation of R_r and L_m.

Note that, h_{12} and Q depend on R_r and L_m. Since an accurate information of these parameters is impossible to get in practice, perturbations may affect the IVCIM performance. The effect of improper parameter estimation on current controller gain sensitivity is also shown in Fig. 5.3(b). It is observed that, in feedforward decoupling, overestimation in compensation signals increase the magnitude. However, it is less affected when decoupler is not used.

Parameter variation effect

In feedforwad decoupling scheme, the compensation terms v_{ds}^{comp} and v_{qs}^{comp} are function of ω_{sl} and c, which depends on R_r and L_m, respectively. Both of these IM parameters may vary with temperature, ageing and other environmental reasons [7]. For determining R_r

variation effect on feedforward decoupling, ΔG in (5.5) is written as:

$$\Delta G = \begin{bmatrix} -E & \mathbf{0}_{2\times 2} \\ \mathbf{0}_{2\times 2} & -E \end{bmatrix} \Delta\omega_{sl} \tag{5.8}$$

where $E = \begin{bmatrix} 0 & -1 \\ 1 & 0 \end{bmatrix}$, $\Delta\omega_{sl} = \frac{\Delta R_r L_m i^e_{qs}}{L_r \psi_{drref}}$, ΔR_r represents perturbation in R_r.
The corresponding sensitivity is obtained as

$$\frac{\Delta i_{ds}}{\Delta\omega_{sl}} = \frac{-h_{11} i^e_{qs} + h_{12} i^e_{ds} + h_{13}\psi^e_{qr} - h_{14}\psi^e_{dr}}{|Q|} \tag{5.9}$$

where $h_{12} = g_{12}g_{34}g_{43} + g_{13}g_{32}g_{44} + g_{14}g_{33}g_{42} - g_{12}g_{33}g_{44} - g_{13}g_{34}g_{42} - g_{14}g_{32}g_{43}$, $h_{13} = g_{12}g_{23}g_{44} + g_{13}g_{24}g_{42} + g_{14}g_{22}g_{43} - g_{12}g_{24}g_{43} - g_{13}g_{22}g_{44} - g_{14}g_{23}g_{42}$, $h_{14} = g_{12}g_{24}g_{33} + g_{13}g_{22}g_{34} + g_{14}g_{23}g_{32} - g_{12}g_{23}g_{34} - g_{13}g_{24}g_{32} - g_{14}g_{22}g_{33}$.
The stator current sensitivity magnitude for R_r variation (20%) is shown in Fig. 5.4(a). It is observed that sensitivity is comparatively larger with decoupler ($\omega_e = 0$). The corresponding sensitivity magnitude variation with change in K_{pd} and K_{pq} is shown in Fig. 5.4(b). It is observed that, initially, the magnitude with decoupler is higher for low frequency (up to 20 rad/sec). However, it is reduced with higher K_{pd}, K_{pq} and frequency, e.g., $K_{pd} = K_{pq} = 100$. A further increment in K_{pd} and K_{pq} reduces the sensitivity magnitude with a marginal value. This shows that the system is quite sensitive to parameter variations.

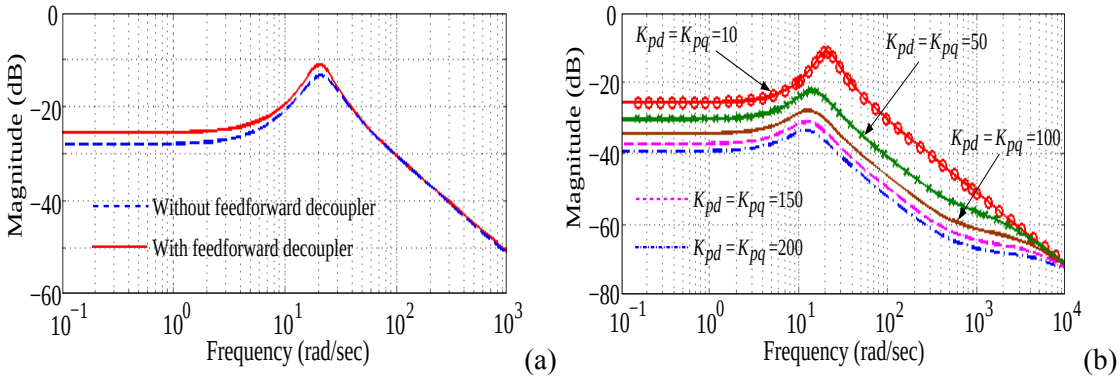

Figure 5.4: Sensitivity of i_{ds} on change in R_r with variation in frequency for feedforward decoupler: (a) $K_{pd} = K_{pq} = 10$. (b) Varying K_{pd}, K_{pq}.

5.4 Coupling Minimization Problem

Considering the disturbance input to the system through the variations in load torque T_L that can be modeled as disturbance $\Delta w = \left[\Delta T_L\right]$, the linearized dynamics of (6.9) using SOF

(4.8) can be represented as:

$$\left.\begin{aligned}\Delta\dot{x} =& A\Delta x + B_1\Delta w + B_2\Delta u\\ \Delta y =& C_2\Delta x\\ \Delta z =& C_1\Delta x\end{aligned}\right\} \tag{5.10}$$

where A is defined in (4.18), $B_1 = \begin{bmatrix}0 & 0 & 0 & 0 & \frac{K_m}{J} & 0 & 0 & 0\end{bmatrix}^T$, B_2 and C_2 are defined in (4.19) and (4.22), respectively.

For minimizing the effect of i_{qs} variation, the dominating nonlinear terms $\omega_e i_{ds}$ and $\omega_e i_{qs}$ are linearized and chosen as the performance variables. Correspondingly, output performance matrix C_1 is obtained as:

$$C_1 = \begin{bmatrix}
\omega_{ref} - x_5^e + \frac{\sigma L_m x_6^e}{K_t \psi_{drref}^2} & 0 & 0 & 0 & 0 & 0 & 0 & 0\\
0 & \omega_{ref} - x_5^e + \frac{\sigma L_m x_6^e}{K_t \psi_{drref}^2} & 0 & 0 & 0 & 0 & 0 & 0\\
0 & 0 & 0 & 0 & x_2^e & 0 & 0 & 0\\
0 & 0 & 0 & 0 & 0 & \frac{\sigma L_m x_2^e}{K_t \psi_{drref}^2} & 0 & 0\\
0 & 0 & 0 & 0 & x_1^e & 0 & 0 & 0\\
0 & 0 & 0 & 0 & 0 & \frac{\sigma L_m x_1^e}{K_t \psi_{drref}^2} & 0 & 0
\end{bmatrix} \tag{5.11}$$

and output feedback matrix C_2 is defined in (4.22).

In the coupling minimization problem, one need to design F (static feedback controller matrix). In this work, the decoupling objective is defined as: to tune F for minimizing the effect of load perturbation Δw on performance variables Δz. Here, F is designed using the Algorithm 2 (As given in **Chapter 4**).

Remark 1: Since the final controller design depends on the convergence of the Algorithm 2, the proposed method may be hindered by possible convergence failure in online implementation, particularly with variation in ψ_{drref} and ω_{ref}. This can be overcome by offline tuning of the controller parameters and then using look-up tables for online implementation.

5.5 Validation and Discussions

5.5.1 Simulation Results

An IVCIM (Fig. 3.8) having the machine parameters in Table 3.4 is used for validating the proposed design. First, the conventional feedforward design is tested. The inner-loop PI design techniques have been discussed in [1, 4, 109]. However, corresponding to higher bandwidth requirement, current controller gains are selected according to the placement of the closed-loop poles and zeros of the IVCIM [4, not the sliding mode controller]. This

design considers i_{ds} and i_{qs} are decoupled. Here, the poles are chosen as 300. Next, zeros are selected to cancel the plant IM poles. The obtained gains are given in Table 5.2. Fig. 5.5 shows the Bode plot of the transfer function $C(s)\frac{i_{ds}(s)}{v_{ds}(s)} = C(s)\frac{i_{qs}(s)}{v_{qs}(s)}$. The bandwidth of the current loops for the designs of [4] and [1] are 380 rad/sec, 400 rad/sec and 45 rad/sec, 45 rad/sec for the d and q current components, respectively. Whereas, the proposed approach provides a bandwidth of 5000 rad/sec for the d current component, which is higher than both the existing designs and represents faster inner-loop response and 38 rad/sec for the q current component.

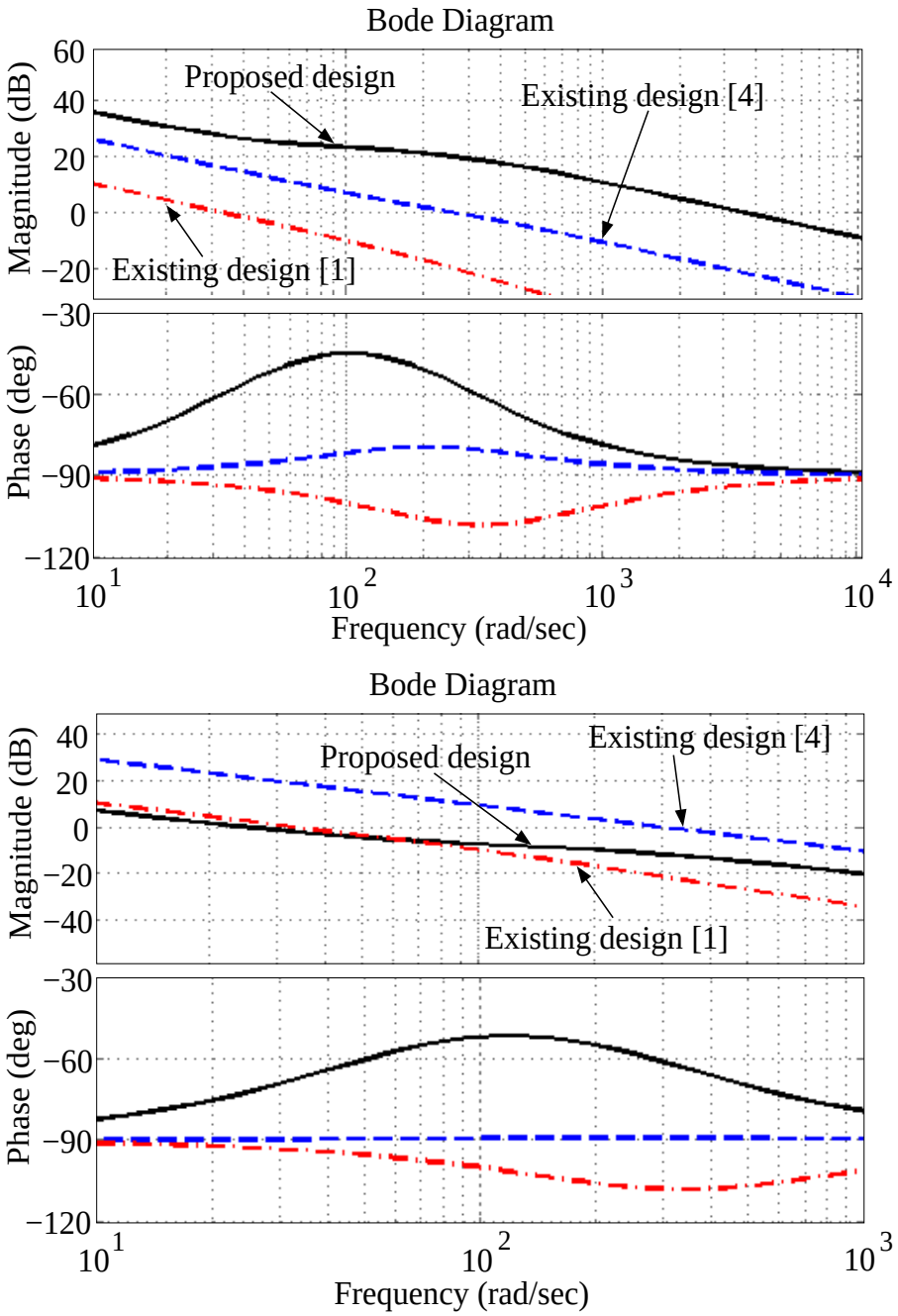

Figure 5.5: Bode plot for inner-loop PI controllers: (a) d current component. (b) q current component.

For the proposed design, first, the parameter ρ in Algorithm 2 is chosen as 12. The reference inputs and the obtained gains are shown in Table 5.1 and Table 5.2, respectively. The controllers are obtained as:

$$K_d(s) = 108\left(1 + \frac{42.92}{s}\right), K_q(s) = 2.2\left(1 + \frac{55.90}{s}\right), K_\omega(s) = 0.4\left(1 + \frac{3}{s}\right).$$

It may be noted that the proposed one yields higher K_{pd}, K_{id} but lower K_{pq}, K_{iq}. However, without systematic design procedure, it is difficult to arrive at such gains. Note that, the same speed-loop gains are used to compare the decoupling performance of the current controller design methods [1, 4].

Table 5.1: Initial Parameters for Algorithm 2

Notation	**Value**	**Notation**	**Value**
ψ_{drref}	0.65 Wb	ω_{ref}	80 rad/sec
B_m	0 N·m/rad/s	T_L	0 N·m

Table 5.2: Controller gains

Description	**Notation and value**
Existing design	
Current controller [4]	$K_{pd} = 8.97$, $K_{id} = 1536$, $K_{pq} = 8.97$, $K_{iq} = 2142$
Current controller [1]	$K_{pd} = 0.53$, $K_{id} = 247$, $K_{pq} = 0.53$, $K_{iq} = 247$
Proposed design	
Current controller	$K_{pd} = 108$, $K_{id} = 4636$, $K_{pq} = 2.2$, $K_{iq} = 123$
Speed controller	$K_{p\omega} = 0.4$, $K_{i\omega} = 1.2$

First, the above two designs are assessed through simulation. The load variation effect on coupling is shown in Fig. 5.6. It is assessed that as T_L is increased from 0 to 6.5 N·m (chosen arbitrarily), i_{ds} of the feedforward decoupling scheme produces a larger shoot. Whereas, in the proposed decoupling, a smaller overshoot occurs in i_{ds}. The outer speed-loop robustness is tested with a step change in ω_{ref} from $100 \rightarrow 150$ rad/sec. The corresponding ω_r response in Fig. 5.7 shows robustness to the sudden variation in ω_{ref}.

Since ω_{sl} and parameter c are susceptible to variations, the feedforward scheme may lead to mismatch in compensation [126]. By considering total 50% variation (35% in R_r, 15% in L_m and L_s), the effect of feedforward decoupling on i_{ds} is shown in Fig. 5.8. It is observed that as T_L is changed at 10 sec, such parameter variation deteriorates i_{ds} current of the feedforward decoupling method. This behavior corroborates the result in Section 5.3. Whereas, the proposed decoupling method yields a smoother i_{ds} current. Moreover, measurement noise also affects the dynamic motoring response. The effect of such noise on i_{ds} behavior for a change in T_L is shown in Fig. 5.9. It is observed that, measurement

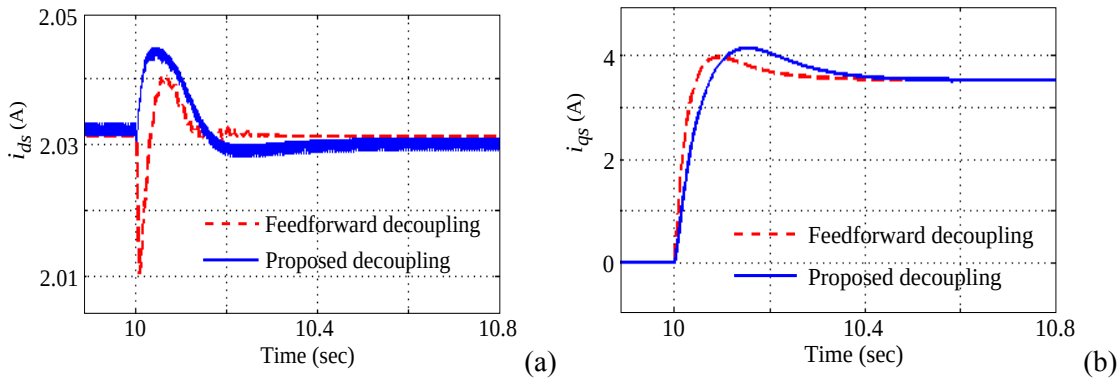

Figure 5.6: Comparison between proposed and feedforward decoupling for a step $T_L = 6.5$ N·m applied at 10 sec: (a) Stator current i_{ds}. (b) Stator current i_{qs}.

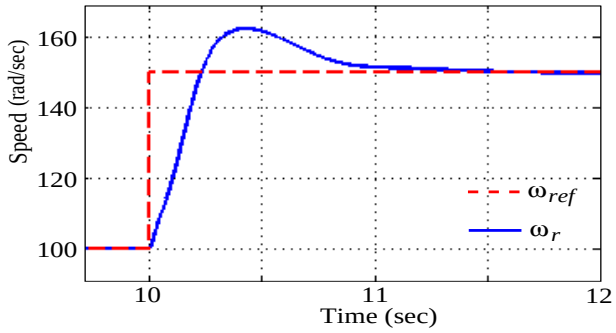

Figure 5.7: ω_r for change in ω_{ref} in step $(100 \rightarrow 150)$.

noise affects i_{ds} current more in the feedforward scheme than with the proposed decoupling design. Here, the measurement noise is considered in the feedback speed signal. The noise parameters are taken as: mean value of 0, variance 0.5 and initial seed as 50000.

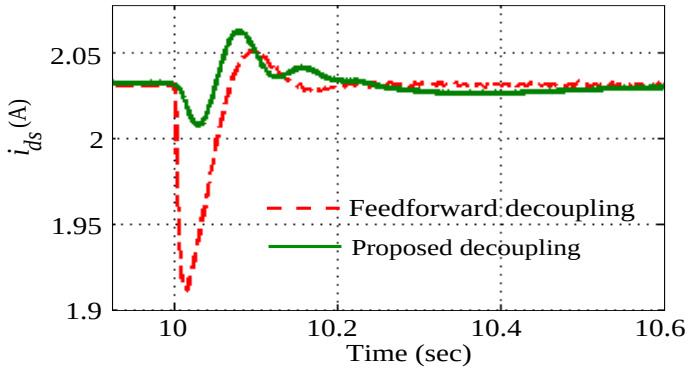

Figure 5.8: Parameter variation effect on behavior of i_{ds}.

Remark 2: The objective of the proposed decoupling technique is on the design of controller gains while minimizing the coupled terms $\omega_e i_{ds}$ and $\omega_e i_{qs}$ effect on the system dynamics. As seen, this technique yields higher K_{pd}, K_{id}, while lesser values for K_{pq}, K_{iq} are obtained. These gains corroborate the result in Section 5.3. The current controller sensitivity expression in equations (5.6) and (5.7) shows that higher proportional gains may

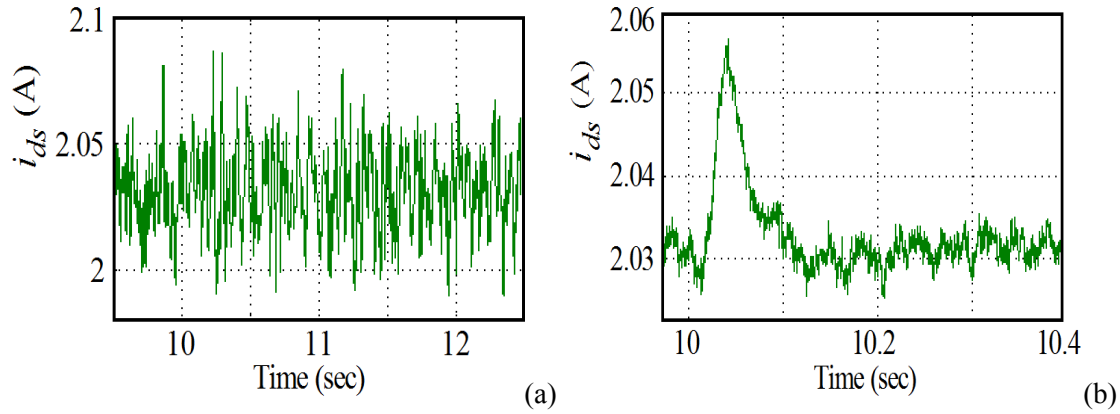

Figure 5.9: Measurement noise affect on i_{ds}: (a) Feedforward decoupling. (b) Proposed decoupling

reduce the perturbation in respective currents. Since the impact of coupled dynamics is more on i_{ds} current, the corresponding controller gains is obtained as higher than that with the i_{qs}. Therefore, when T_L is changed, due to high bandwidth control for i_{ds}, less perturbation occurs in the corresponding current.

5.5.2 Experimental Results

The developments are next validated on an experimental bench as shown in Fig. 3.17. Since inner-loop gains primarily affect the coupling between i_{ds} and i_{qs}, therefore, first, the effect of load variation is tested with the proposed decoupling speed-loop gains and inner-loop gains in [1, 4]. When the motor speed reaches to applied reference speed (130 rad/sec), a step load torque of about 6.5 N·m is exerted. The corresponding experimental result for ω_r, i_{ds} and i_{qs} are shown in Fig. 5.10(a)-(b). It is observed that as T_L is changed, a large overshoot of about 10 A occurs in i_{ds}. Next, the feedforward compensation is implemented with the inner-loop PI gains in [4]. For this, the IM dynamics behavior with a change in T_L is shown in Fig. 5.10(c). Further, same load variation is applied to the proposed decoupling gains as shown in Fig. 5.10(d). It is seen that i_{ds} with the feedforward and proposed design shows a small overshoot of about 6A (zoomed portion), which is much lesser than the i_{ds} in Fig. 5.10(a)-(b). Such behavior confirms the simulation results in Fig. 5.6. Here, i_{ds} response is almost similar in both the feedforward and proposed decoupling. Hence, without additional arrangements (as required in feedforward decoupling), similar decoupling performance is achieved using the proposed method with the same regulating PI controllers.

The experimental result for outer speed-loop control is shown in Fig. 5.11. It is seen that ω_r tracks smoothly even at large step change in ω_{ref}. The current tracking performance of i_{qs} for step change in T_L (6.5 N·m) and ω_{ref} (100 $\rightarrow$ 150 $\rightarrow$ 100) is also shown in Fig. 5.12, which shows smooth current tracking is achieved using proposed design.

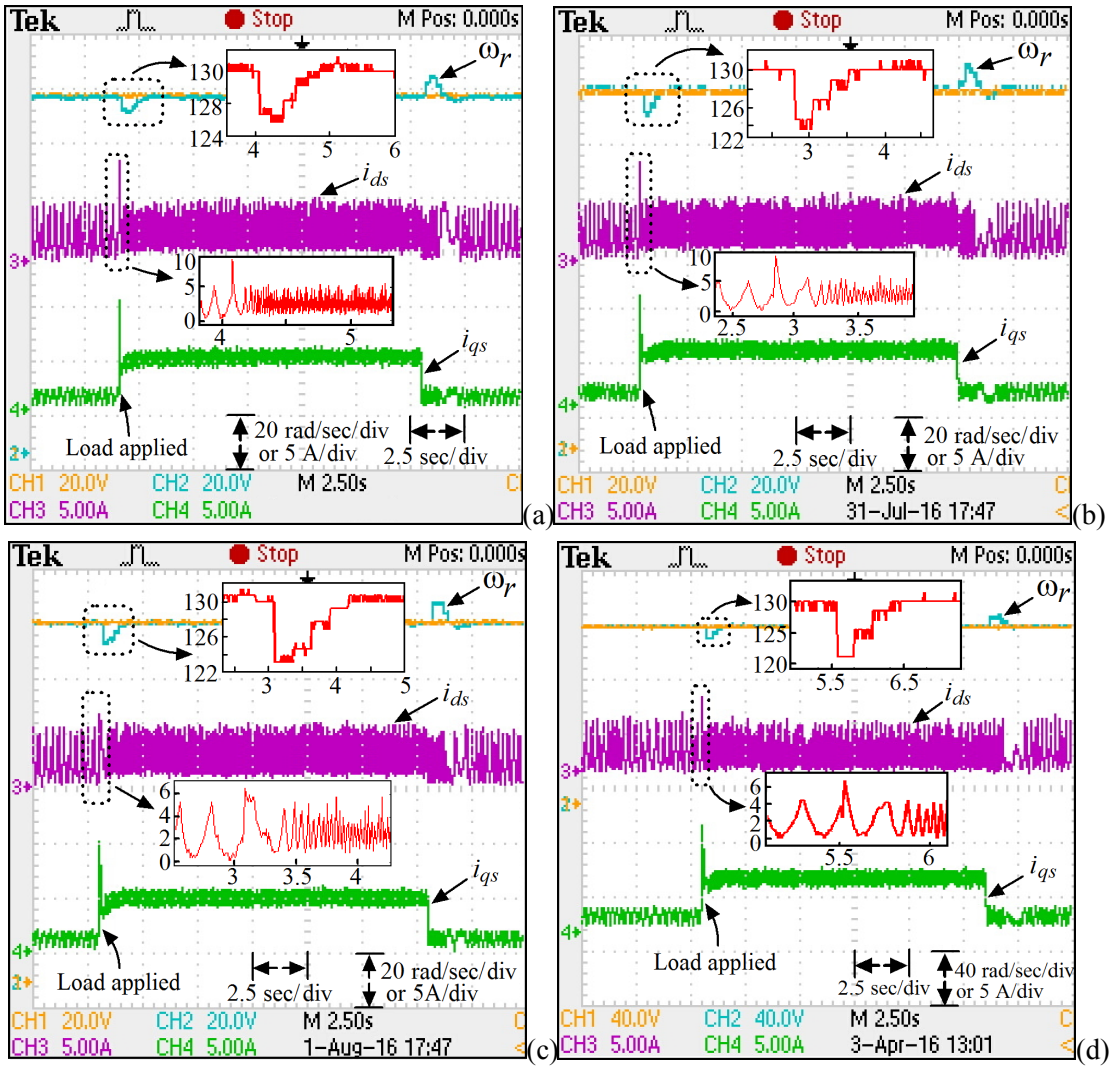

Figure 5.10: Experimental result for variation in T_L: (a) Without decoupling [4]. (b) Without decoupling [1]. (c) Feedforward decoupling. (d) Proposed decoupling.

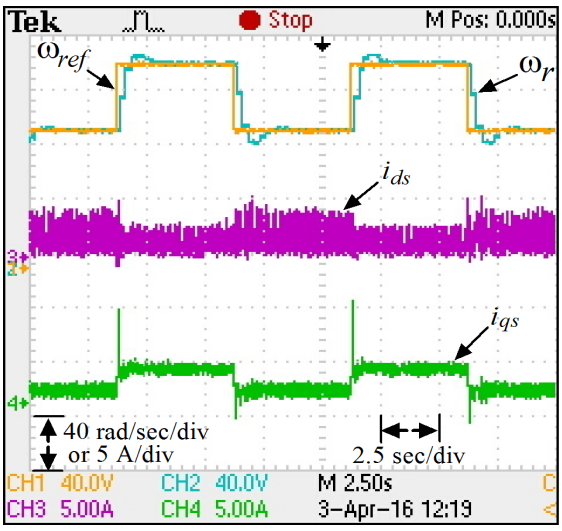

Figure 5.11: Experimental result for change in ω_{ref} in step ($100 \rightarrow 150 \rightarrow 100$).

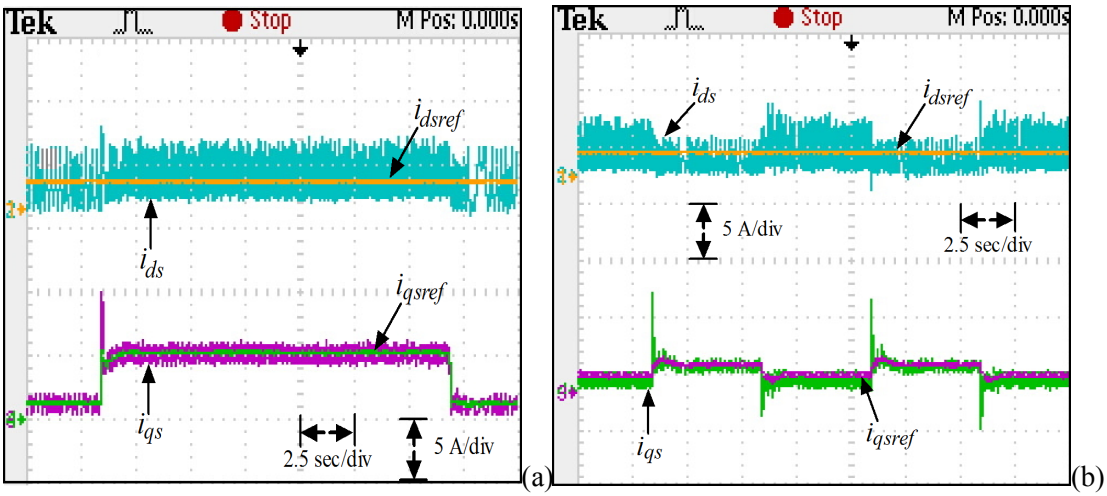

Figure 5.12: Experimental result of current tracking performance for change in: (a) T_L. (b) ω_{ref}.

5.6 Chapter Summary

In this chapter, the inner current control loop is designed to minimize the coupling between torque and flux components of the stator current. The conventionally used feedforward decoupling induce complexity, require more signal processing and increases sensitivity of the currents on parameter variations. The sensitivity of the current controller gains on variation of inner-loop gains determined, which depicts high controller gains improves decoupling. However, high gains may cause instability, therefore, a systematic controller design procedure is applied to minimize coupling. An iterative linear matrix inequality based algorithm is used to design H_∞ proportional integral controller gains which minimizes the coupling between stator current components. The simulation and experimental comparison results to the existing approaches shows that the proposed approach provides an alternative and simpler way to achieve decoupling.

Although PI tuning improves the dynamic performance of the motor. A further performance enhancement requires to use a dynamic controller which can deal with the sharp variations in reference quantities. In the next chapter, a dynamic controller design is structured for IVCIM.

Chapter 6
A Dynamic Controller Design for IVCIM

6.1 Introduction

Indirect vector control (IVC) technique for IM is popular because of its simplicity yet capability to deliver high performance. The scheme requires regulation of two current-loops and one speed-loop. Conventionally, the regulation of the stator currents is considered as decoupled from the speed-loop and can be configured in either of SRFC, SRC or hysteresis control [102, 103, 106]. Among these, SRFC is the simplest and has the advantage of operating on direct current (DC) quantities leading to zero steady-state error and negligible cross coupling [108, 137]. However, these advantages rely on the efficient design of the controllers.

PI and several other linear, nonlinear and intelligent controllers have been designed to regulate the speed-loop of the IVCIM system in [94, 100, 138–142]. Among these, PI controller is conventionally used. Although the controllers in [100, 139–142] improve performance, complexity associated with additional dynamics or structure induces difficulty in implementation and requires more computational power. Recently, a SRC based speed-loop compensator design technique has been proposed in [3]. However, this design relies on robust stability, which may limit its performance on large variation of load torque and motor speed. On the other hand, for the current regulation, PI, sliding mode, neural network, predictive and compensator designs have been discussed in [1, 4, 100, 109, 110, 140]. However, most of the these techniques consider a low-order model of IM, which may affect the IVCIM performance. As far as the PI controller is concerned, it is a low-order (first-order one) for the 5^{th}-order IM dynamics. Hence, its performance is limited.

On the other hand, dynamic controller design has been used in many practical problems and gained popularity due to its simplicity and significant performance [143–145]. In addition, since the stator current is also derived to the IM core and flows into the iron, iron loss problem is occurred. Hence, getting a decoupled and robust torque performance with conventional control schemes is difficult [146, 147]. Various methods (modified speed-loop controllers) are introduced in order to minimize this iron loss problem [148–150]. However, a linear controller design while considering dynamic performance yet maintaining simplicity in design and involving iron loss dynamics still does not exist in literature.

For obtaining high performance, in this work, a dynamic control structure and its design for IVCIM is addressed. A full IM model (7^{th} order) in SRFC with iron loss dynamics is employed for the design. The current controller design is modeled in SRFC. A multiple-input and multiple-output (MIMO) DOF based closed-loop structure is framed for designing the current-loop controller and then sequential design for the speed-loop is invoked. The designed current-loop controller is included in the model while designing the outer speed-loop controller. The rotor resistance variation, uncertainty of states and load torque are considered as disturbances. An ILMI based H_∞ control design technique is employed for the design. A Performance comparison of the proposed and the conventional PI controller is demonstrated through simulation and experiment results. The obtained results show improved dynamic performance of the IVCIM while employing the proposed controller.

The structure of this chapter is organized as follows: Section 6.2 presents the DOF control structure for IVCIM comprising of inner-loop, outer-loop design, iron loss and uncertainty model. A performance evaluation of the designed controller with simulation and experimental results is shown in Section 6.5. At the end, relevant conclusions and discussions are pointed out in Section 6.6.

6.2 The Proposed Dynamic Controller

A block diagram of IVCIM drive system for speed regulation is shown in Fig. 6.1. The vector control operation is achieved by one speed, $C_\omega(s)$, and two current, $C_d(s)$ and $C_q(s)$, controllers. Conventionally, individual PI controllers are used for $C_\omega(s)$, $C_d(s)$ and $C_q(s)$.

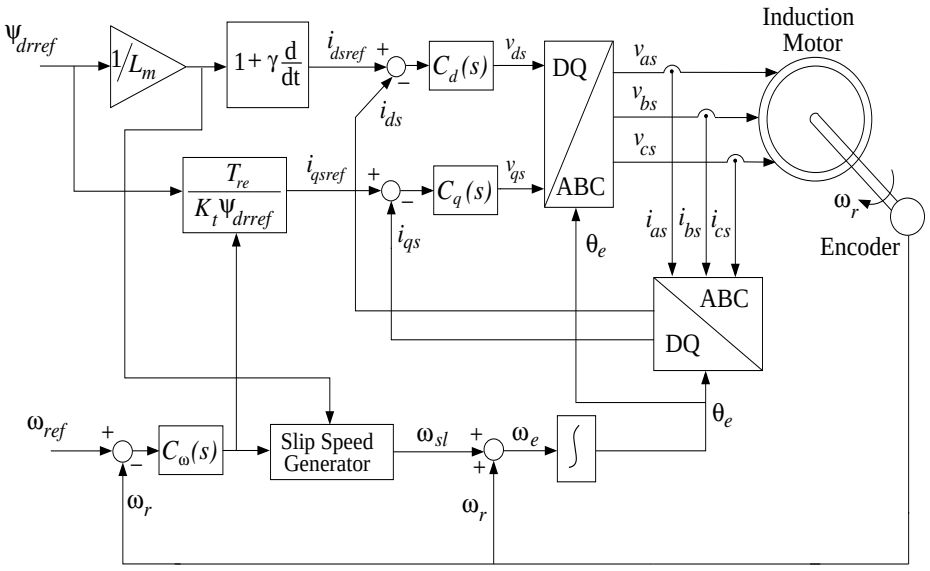

Figure 6.1: Indirect vector control scheme for induction motor.

The proposed dynamic controller structure is shown in Fig. 6.2 where $K(s)$ represents

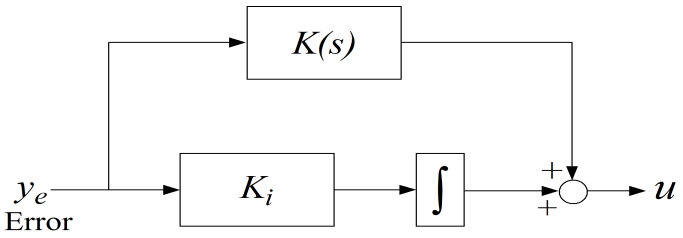

Figure 6.2: Controller structure.

the dynamic controller that improves the dynamic performance, whereas the integral gain K_i takes care of the steady-state error. The case of $K(s) = K_p$, with K_p constant, represents a PI controller. To this end, the IM model being high order, a simple P-controller for $K(s)$ is too restrictive to govern the system dynamics. Earlier works, such as [3], attempted to improve the system performance using a 3^{rd} order dynamic controller, where the design is based on compensation scheme in frequency domain. In this work, we use a generic state-space model of such DOF controller as:

$$\begin{aligned} K(s) : \dot{\hat{x}}_c =& \hat{A}_c \hat{x}_c + \hat{B}_c y_e, \\ u =& \hat{C}_c \hat{x}_c + \hat{D}_c y_e \end{aligned} \tag{6.1}$$

where $\hat{x}_c$ is the state of the dynamic controller, y_e is the error signal fed to the controller, u is the controller output that is fed to the plant, $\hat{A}_c$, $\hat{B}_c$ and $\hat{C}_c$, $\hat{D}_c$ are the controller matrices which are to be designed for each of the $C_\omega(s)$, $C_d(s)$ and $C_q(s)$. The order of the dynamic controller can be chosen as high as the plant order. For demonstration, we consider a first-order dynamic controller just to highlight its superiority over the PI one. Besides, use of P control transfers step errors (for example step change in reference) proportionally to the inverter whereas the proposed dynamical one transfers it smoothly that reduces the wear and tear in the mechanical components.

6.3 IVCIM Model

The motor model is considered in the synchronously rotating reference frame through the $d-q$ axis representation, where the d-axis is in phase to the magnetizing flux and its quadrature axis is the q-axis [6]. The $d-q$ axis equivalent circuit considering core-loss is shown in Fig. 6.3 [147], where i_{ds}, i_{qs}, i_{dfe}, i_{qfe}, i_{dm} and i_{qm} are the direct and quadrature components of stator, iron-loss and magnetizing currents, respectively. The corresponding

IM model can be written as:

$$\left.\begin{aligned}
\frac{di_{ds}}{dt} &= -(\eta_5+\eta_2\eta_4L_m)i_{ds}+\omega_e i_{qs}-\eta_3\eta_4L_m\psi_{dr}+\eta_3\eta_4L_rL_mi_{dm}+\eta_4v_{ds}\\
\frac{di_{qs}}{dt} &= -\omega_e i_{ds}-(\eta_5+\eta_2\eta_4L_m)i_{qs}-\eta_3\eta_4L_m\psi_{qr}+\eta_3\eta_4L_rL_mi_{qm}+\eta_4v_{qs}\\
\frac{d\psi_{dr}}{dt} &= -\eta_1\psi_{dr}+\omega_{sl}\psi_{qr}+\eta_1L_mi_{dm}\\
\frac{d\psi_{qr}}{dt} &= -\omega_{sl}\psi_{dr}-\eta_1\psi_{qr}+\eta_1L_mi_{qm}\\
J\frac{d\omega_r}{dt} &= K_m(T_e-T_L)-B_m\omega_r\\
\frac{di_{dm}}{dt} &= \eta_2i_{ds}+\eta_3\psi_{dr}-\eta_3L_ri_{dm}+\omega_ei_{qm}\\
\frac{di_{qm}}{dt} &= \eta_2i_{qs}+\eta_3\psi_{qr}-\eta_3L_ri_{qm}-\omega_ei_{dm}
\end{aligned}\right\} \quad (6.2)$$

where electromagnetic torque $T_e = K_l(\psi_{dr}i_{qm}-\psi_{qr}i_{dm})$, $K_l = \frac{3PL_m}{4(L_r-L_m)}$, $K_m = \frac{P}{2}$, $\eta_1 = \frac{R_r}{L_r-L_m}$, $\eta_2 = \frac{R_{fe}}{L_m}$, $\eta_3 = \frac{\eta_2}{L_r-L_m}$, $\eta_4 = \frac{1}{L_s-L_m}$, $\eta_5 = R_s\eta_4$, $i_{dm} = i_{ds}+i_{dr}-i_{dfe}$, $i_{qm} = i_{qs}+i_{qr}-i_{qfe}$ where i_{dr} and i_{qr} are the direct and quadrature components of rotor currents; ψ_{dr} and ψ_{qr} are the direct and quadrature components of rotor fluxes.

Note that, the IVC scheme for induction motor is governed by $i_{dsref} = \frac{\psi_{drref}+\gamma\dot{\psi}_{drref}}{L_m}$, $i_{qsref} = \frac{T_{re}}{K_t\psi_{drref}}$, $\omega_{sl} = \frac{(\sigma+\delta)L_mi_{qsref}}{\psi_{dref}}$, where i_{dsref} is the reference flux component of current; i_{qsref} is the reference torque component of current; ψ_{drref} is the reference flux; T_{re} is the torque output of the speed controller, $K_t = \frac{3PL_m}{4L_r}$. $\sigma = \frac{R_r}{L_r}$ is the inverse of the rotor time-constant and δ is a perturbation in σ due to variation in rotor resistance.

The output of the current controllers in Fig. 3.1 are the stator voltages, which can be written as:

$$\left.\begin{aligned}
v_{ds} &= u_{ds}+K_{id}\int(i_{dsref}-i_{ds})dt\\
v_{qs} &= u_{qs}+K_{iq}\int(i_{qsref}-i_{qs})dt
\end{aligned}\right\} \quad (6.3)$$

where $u_{ds} = K_d(s)(i_{dsref}-i_{ds})$ and $u_{qs} = K_q(s)(i_{qsref}-i_{qs})$.

The objective of this work is to design $K_d(s)$, $K_q(s)$ and $K_\omega(s)$ in such a way that the IVCIM works well even in the presence of uncertain δ and T_L. The corresponding feedback control system is shown in Fig. 6.4, where $w(t)$ is the disturbance that incorporates the effects of δ and T_L in the system dynamics. The controllers uses the measured output signal $y(t)$ to generate the control input signal $u(t)$ with the control objective to minimize the effect of $w(t)$ on the output $z(t)$ in the H_∞ control framework [115, 151]. The models for such a design are developed and a design procedure is demonstrated.

6.4 Control Problem Formulation

A sequential design procedure is followed for designing the controllers in which the inner-loop current controllers are designed first, and these are further incorporated in the model while designing the outer speed-loop controller. For the purpose, the two controller design models are presented in this section.

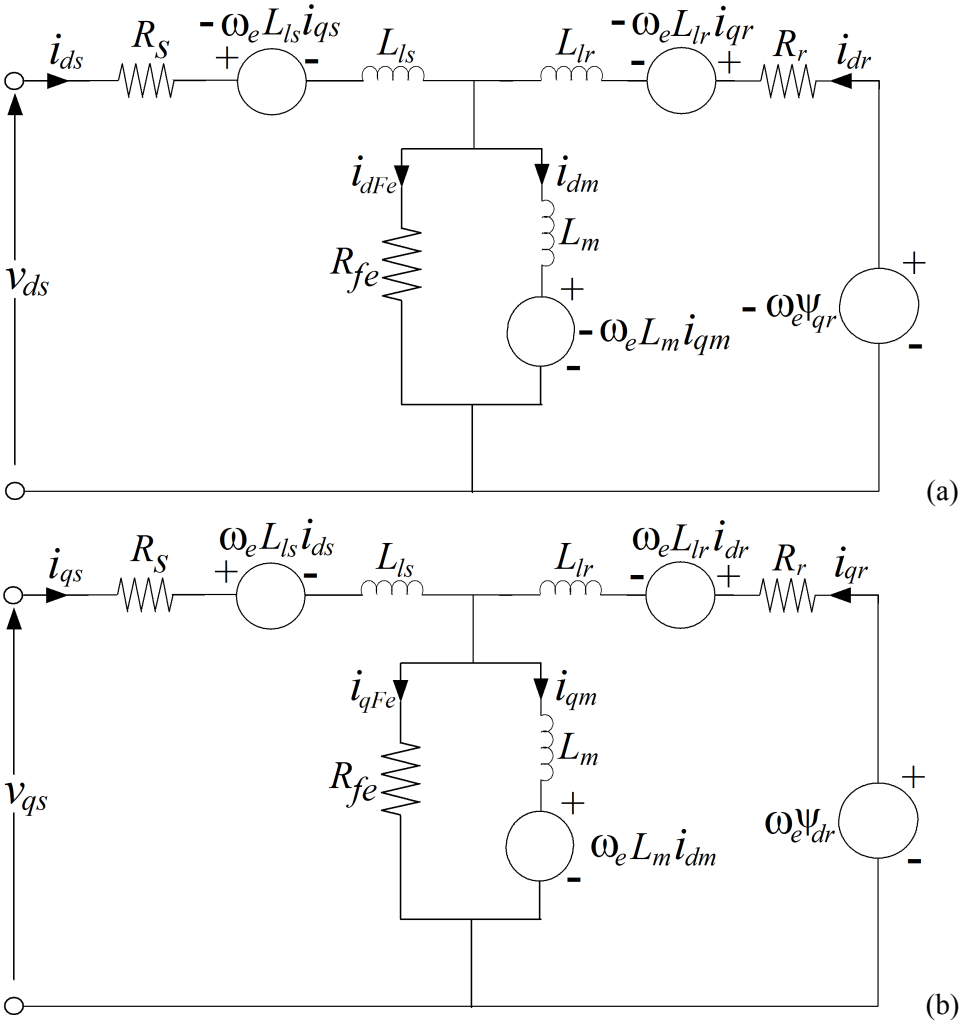

Figure 6.3: $d-q$ axis equivalent circuit with iron core loss:(a) d-equivalent circuit. (b) q-equivalent circuit.

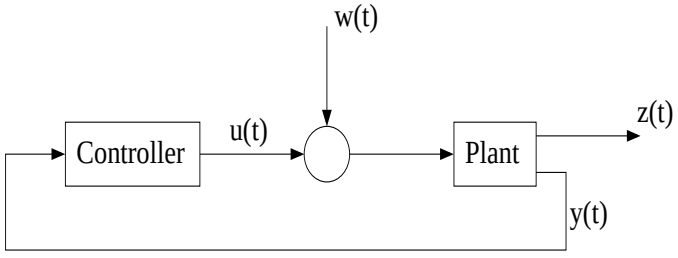

Figure 6.4: Block-diagram of a feedback control system with disturbance.

6.4.1 Current-Loop Model

The DOF controllers for the two current controllers $C_d(s)$ and $C_q(s)$ are designed simultaneously. In view of the first-order dynamics of the DOF controllers as in (6.1), the two controller states can be augmented and can be represented as a single controller with the controller matrices defined as:

$$\hat{A}_c = \begin{bmatrix} a_d & 0 \\ 0 & a_q \end{bmatrix}, \hat{B}_c = \begin{bmatrix} b_d & 0 \\ 0 & b_q \end{bmatrix}, \hat{C}_c = \begin{bmatrix} c_d & 0 \\ 0 & c_q \end{bmatrix}, \hat{D}_c = \begin{bmatrix} d_d & 0 \\ 0 & d_q \end{bmatrix} \tag{6.4}$$

where a_j, b_j, c_j and d_j, $j = d, q$, are the controller parameters for the respective DOFs. Note that, the above controller parameters are structured and can only be addressed through decentralized controller [143, 151] design framework. The states of the respective integral gains are included in the plant model as described in the following.

Since the speed-loop controller will be designed later, the speed dynamics is not included in this model. Further, it is considered that $\omega_r = \omega_{ref}$. Note that, the disturbance input to the system is through the uncertain terms involving δ. Now, define the states of the IM model as $x_1 = i_{ds}$, $x_2 = i_{qs}$, $x_3 = \psi_{dr}$, $x_4 = \psi_{qr}$, $x_5 = i_{dm}$, $x_6 = i_{qm}$, and states of the integral gains as $x_7 = \int (i_{dsref} - i_{ds})dt$, $x_8 = \int (i_{qsref} - i_{qs})dt$. Then, in view of (6.2) and (6.3), the linear current-loop model can be written as:

$$\left.\begin{aligned}
\dot{x}_1 =& -(\eta_5 + \eta_2\eta_4 L_m)x_1 + \left(\omega_{ref} + \frac{(\sigma+\delta)L_m i_{qsref}}{\psi_{drref}}\right)x_2 - \eta_3\eta_4 L_m x_3 \\
&+ \eta_3\eta_4 L_r L_m x_5 + \eta_4(u_d + K_{id}x_7) \\
\dot{x}_2 =& -\left(\omega_{ref} - x_5 + \frac{(\sigma+\delta)L_m i_{qsref}}{\psi_{drref}}\right)x_1 - (\eta_5 + \eta_2\eta_4 L_m)x_2 - \eta_3\eta_4 L_m x_4 \\
&+ \eta_3\eta_4 L_r L_m x_6 + \eta_4(u_q + K_{iq}x_8) \\
\dot{x}_3 =& -\eta_1 x_3 + \frac{(\sigma+\delta)L_m i_{qsref}}{\psi_{drref}}x_4 + \eta_1 L_m x_5 \\
\dot{x}_4 =& -\frac{(\sigma+\delta)L_m i_{qsref}}{\psi_{drref}}x_3 - \eta_1 x_4 + \eta_1 L_m x_6 \\
\dot{x}_5 =& \eta_2 x_1 + \eta_3 x_3 - \eta_3 L_r x_5 + \frac{(\sigma+\delta)L_m i_{qsref}}{\psi_{drref}}x_6 \\
\dot{x}_6 =& \eta_2 x_2 + \eta_3 x_4 - \frac{(\sigma+\delta)L_m i_{qsref}}{\psi_{drref}}x_5 - \eta_3 L_r x_6 \\
\dot{x}_7 =& L_m^{-1}\gamma\dot{\psi}_{drref} + L_m^{-1}\psi_{drref} - x_1 \\
\dot{x}_8 =& i_{qsref} - x_2
\end{aligned}\right\} \tag{6.5}$$

where $u_d = K_1(s)\left(L_m^{-1}\gamma\dot{\psi}_{drref} + L_m^{-1}\psi_{drref} - x_1\right)$ and $u_q = K_2(s)\left(i_{qsref} - x_2\right)$.

The above current-loop model (6.5) further can be written as

$$\dot{x}_{cur} = A_{cur}x_{cur} + B_{cur}u_{cur} + E_{cur}w_{cur}, \qquad y = C_{cur}x_{cur} \tag{6.6}$$

where x_{cur}=$[x_1, \cdots, x_8]^T$, $u_{cur} = \begin{bmatrix} u_{ds} & u_{qs} \end{bmatrix}^T$ and $y_{cur} = \begin{bmatrix} x_7 & x_8 \end{bmatrix}^T$. The corresponding system matrix A_{cur} is given as $A_{cur} = \begin{bmatrix} A_{cur1} & A_{cur2} \end{bmatrix}$,

$$A_{cur1} = \begin{bmatrix} -(\eta_5 + \eta_2\eta_4 L_m) & \omega_{ref} + \frac{\sigma L_m i_{qsref}}{\psi_{drref}} & -\eta_3\eta_4 L_m & 0 \\ -\omega_{ref} - \frac{\sigma L_m i_{qsref}}{\psi_{drref}} & -(\eta_5 + \eta_2\eta_4 L_m) & 0 & -\eta_3\eta_4 L_m \\ 0 & 0 & -\eta_1 & \frac{\sigma L_m i_{qsref}}{\psi_{drref}} \\ 0 & 0 & -\frac{\sigma L_m i_{qsref}}{\psi_{drref}} & -\eta_1 \\ \eta_2 & 0 & \eta_3 & 0 \\ 0 & \eta_2 & 0 & \eta_3 \\ -1 & 0 & 0 & 0 \\ 0 & -1 & 0 & 0 \end{bmatrix},$$

$$A_{cur2} = \begin{bmatrix} \eta_3\eta_4 L_r L_m & 0 & \eta_4 K_{id} & 0 \\ 0 & \eta_3\eta_4 L_r L_m & 0 & \eta_4 K_{iq} \\ \eta_1 L_m & 0 & 0 & 0 \\ 0 & \eta_1 L_m & 0 & 0 \\ -\eta_3 L_r & \omega_{ref} + \frac{\sigma L_m i_{qsref}}{\psi_{drref}} & 0 & 0 \\ -\omega_{ref} - \frac{\sigma L_m i_{qsref}}{\psi_{drref}} & -\eta_3 L_r & 0 & 0 \\ 0 & 0 & 0 & 0 \\ 0 & 0 & 0 & 0 \end{bmatrix},$$

The control input matrix and output matrices are given as

$$B_{cur} = \begin{bmatrix} \eta_4 & 0 & \mathbf{0}_{1\times 6} \\ 0 & \eta_4 & \mathbf{0}_{1\times 6} \end{bmatrix}^T, \; C_{cur} = \begin{bmatrix} \mathbf{0}_{1\times 6} & -1 & 0 \\ \mathbf{0}_{1\times 6} & 0 & -1 \end{bmatrix}. \tag{6.8}$$

The disturbance is defined as:

$$w_{cur} = \begin{bmatrix} \delta x_1 & \delta x_2 & \cdots & \delta x_6 & \xi_1 & \xi_2 & \cdots & \xi_5 \end{bmatrix}^T$$

where $\xi_1, \cdots, \xi_5$ represent the disturbance induced by the magnetizing currents i_{dm} and i_{qm} and the corresponding disturbance input matrix E_{cur} is given in (6.7) on page 90.

Augmenting (6.1) (in view of (6.4)) and (6.6), and after some algebraic manipulation,

$$Ecur = \begin{bmatrix} E_{cur1} & E_{cur2} \end{bmatrix},$$

$$E_{cur1} = \begin{bmatrix} 0 & \frac{L_m i_{qsref}}{\psi_{drref}} & 0 & 0 & 0 & 0 \\ -\frac{L_m i_{qsref}}{\psi_{drref}} & 0 & 0 & 0 & 0 & 0 \\ 0 & 0 & 0 & \frac{L_m i_{qsref}}{\psi_{drref}} & 0 & 0 \\ 0 & 0 & -\frac{L_m i_{qsref}}{\psi_{drref}} & 0 & 0 & 0 \\ 0 & 0 & 0 & 0 & 0 & \frac{L_m i_{qsref}}{\psi_{drref}} \\ 0 & 0 & 0 & 0 & -\frac{L_m i_{qsref}}{\psi_{drref}} & 0 \\ 0 & 0 & 0 & 0 & 0 & 0 \\ 0 & 0 & 0 & 0 & 0 & 0 \end{bmatrix}, \tag{6.7}$$

$$E_{cur2} = \begin{bmatrix} 0 & 1 & 0 & 0 & 0 & 0 & 0 & 0 \\ 0 & 0 & 1 & 0 & 0 & 0 & 0 & 0 \\ 0 & 0 & 0 & 1 & 0 & 0 & 0 & 0 \\ 0 & 0 & 0 & 0 & 1 & 0 & 0 & 0 \\ 0 & 0 & 0 & 0 & 0 & 1 & 0 & 0 \end{bmatrix}^T.$$

the closed-loop system can be represented as:

$$\dot{\tilde{x}}_{cur} = (\tilde{A}_{cur} + \tilde{B}_{cur}\tilde{F}_{cur}\tilde{C}_{cur})\tilde{x} + \tilde{E}_{cur}\tilde{w}_{cur} \tag{6.9}$$

where $\tilde{x}_{cur} = \begin{bmatrix} x_{cur}^T & \hat{x}_{cur}^T \end{bmatrix}^T$, $\hat{x}_{cur}$ is the controller states, $\tilde{w}_{cur} = \begin{bmatrix} w_{cur}^T & \mathbf{0}_{1\times 2} \end{bmatrix}^T$ and

$$\tilde{A}_{cur} = \begin{bmatrix} A_{cur} & \mathbf{0}_{8\times 2} \\ \mathbf{0}_{2\times 8} & \mathbf{0}_{2\times 2} \end{bmatrix}, \ \tilde{B}_{cur} = \begin{bmatrix} B_{cur} & \mathbf{0}_{8\times 2} \\ \mathbf{0}_{2\times 2} & I_2 \end{bmatrix},$$
$$\tilde{C}_{cur} = \begin{bmatrix} C_{cur} & \mathbf{0}_{2\times 2} \\ \mathbf{0}_{2\times 2} & I_2 \end{bmatrix}, \ \tilde{F}_{cur} = \begin{bmatrix} \hat{D}_c & \hat{C}_c \\ \hat{B}_c & \hat{A}_c \end{bmatrix}.$$

Following Fig. 6.4, the output vector $z(t)$ is chosen so as to minimize the effect of $w(t)$ on the stator currents and rotor fluxes of the motor. The corresponding choice is

$$\tilde{z}_{cur} = \tilde{G}_{cur}\tilde{x}_{cur} \tag{6.10}$$

where $\tilde{G}_{cur} = I$.

The system model (6.9) along with (6.10) is used to design the current-loop controller parameters (6.4). For this, Algorithm 2 on page 59 is followed. The designed controller (6.4) is further used to model the outer speed-loop control problem in the following section.

6.4.2 Speed-Loop Model

The speed dynamics and the current controller states are included in the model. The new state definitions are: $x_9 = \omega_r$, $x_{10} = \int(\omega_{ref} - \omega_r)dt$, $\begin{bmatrix} x_{11} & x_{12} \end{bmatrix} = \hat{x}_{cur}$. The corresponding

model can be written as

$$\left.\begin{aligned}
\dot{x}_1 =& -(\eta_5+\eta_2\eta_4 L_m)x_1+[x_9+(\sigma+\delta)L_m(K_t\psi_{drref}^2)^{-1}(K_{i\omega}x_{10}+v_\omega)]x_2\\
&-\eta_3\eta_4 L_m x_3+\eta_3\eta_4 L_r L_m x_5+\eta_4\left(\hat{c}_d x_{11}+\hat{d}_d(L_m^{-1}\psi_{drref}-x_1)+K_{id}x_7\right)\\
\dot{x}_2 =& -[x_9+(\sigma+\delta)L_m(K_t\psi_{drref}^2)^{-1}(K_{i\omega}x_{10}+v_\omega)]x_1-(\eta_5+\eta_2\eta_4 L_m)x_2\\
&-\eta_3\eta_4 L_m x_4+\eta_3\eta_4 L_r L_m x_6+\eta_4\left(\hat{c}_q x_{12}+\hat{d}_q\left((K_t\psi_{drref})^{-1}(K_{i\omega}x_{10}+v_\omega)\right.\right.\\
&\left.\left.-x_2\right)+K_{id}x_8\right)\\
\dot{x}_3 =& -\eta_1 x_3+(\sigma+\delta)L_m(K_t\psi_{drref}^2)^{-1}(K_{i\omega}x_{10}+v_\omega)x_4+\eta_1 L_m x_5\\
\dot{x}_4 =& -(\sigma+\delta)L_m(K_t\psi_{drref}^2)^{-1}(K_{i\omega}x_{10}+v_\omega)x_3-\eta_1 x_4+\eta_1 L_m x_6\\
\dot{x}_5 =& \eta_2 x_1+\eta_3 x_3-\eta_3 L_r x_5+[x_9+(\sigma+\delta)L_m(K_t\psi_{drref}^2)^{-1}(K_{i\omega}x_{10}+v_\omega)]x_6\\
\dot{x}_6 =& \eta_2 x_2+\eta_3 x_4-[x_9+(\sigma+\delta)L_m(K_t\psi_{drref}^2)^{-1}(K_{i\omega}x_{10}+v_\omega)]x_5-\eta_3 L_r x_6\\
\dot{x}_7 =& L_m^{-1}\gamma\dot{\psi}_{drref}+L_m^{-1}\psi_{drref}-x_1\\
\dot{x}_8 =& (K_t\psi_{drref})^{-1}(K_{i\omega}x_{10}+v_\omega)-x_2\\
J\dot{x}_9 =& K_m\left[K_l(x_3x_6-x_4x_5)-T_L\right]-B_m x_9\\
\dot{x}_{10} =& \omega_{ref}-x_9\\
\dot{x}_{11} =& \hat{a}_d x_{11}+\hat{b}_d(L_m^{-1}\gamma\dot{\psi}_{drref}+L_m^{-1}\psi_{drref}-x_1)\\
\dot{x}_{12} =& \hat{a}_q x_{12}+\hat{b}_q((K_t\psi_{drref})^{-1}(K_{i\omega}x_{10}+v_\omega)-x_2)
\end{aligned}\right\} \tag{6.11}$$

Note that, unlike the current-loop model, (6.11) is nonlinear. Here, $i_{qsref} = (K_t\psi_{drref})^{-1}(K_{i\omega}x_{10}+v_\omega)$ where v_ω is the dynamic controller for the outer speed-loop.

Iron loss effect

The iron loss affect on IVCIM is analyzed using linearization of (6.11). For this, the equilibrium of the states is determined for the nominal model at $\delta = 0$ and $x_9^e = \omega_{ref}$ as:

$$\left.\begin{aligned}
x_1^e =& \frac{\psi_{drref}}{L_m},\ \ x_2^e=\frac{T_{re}}{K_t\psi_{drref}},\ \ x_3^e=\frac{(L_r\eta_3-\beta_1)x_5^e+\beta_2 x_2^e-\eta_2 x_1^e}{\eta_3},\\
x_4^e =& \frac{L_m\eta_1^2 x_6^e-L_m\eta_1\omega_{sl}^e x_5^e}{\eta_1^2+(\omega_{sl}^e)^2},\ \ x_5^e=\frac{d_1}{d_2}\ \text{ and }\ x_6^e=\frac{\beta_1 x_5^e-\beta_2 x_2^e}{\omega_{ref}+\omega_{sl}^e}
\end{aligned}\right\} \tag{6.12}$$

where $x^e=[x_1^e,\cdots,x_6^e]$ are the states of the equilibrium point and

$$\begin{aligned}
\beta_1 =& \frac{(\omega_{ref}+\omega_{sl}^e)\left((\eta_1^2+(\omega_{sl}^e)^2)(\omega_{ref}+\omega_{sl}^e)+\eta_3\eta_1 L_m\omega_{sl}^e\right)}{\eta_3\left(L_m\eta_1^2-(\eta_1^2+(\omega_{sl}^e)^2)L_r\right)},\\
\beta_2 =& \frac{\eta_2(\omega_{ref}+\omega_{sl}^e)(\eta_1^2+(\omega_{sl}^e)^2)}{\eta_3\left(L_m\eta_1^2-(\eta_1^2+(\omega_{sl}^e)^2)L_r\right)},\ \ d_1=\frac{\beta_2 x_2^e-\eta_2 x_1^e}{\eta_3}+\frac{L_m\eta_1^2\beta_2\omega_{sl}^e x_2^e}{\eta_1(\omega_{ref}+\omega_{sl}^e)(\eta_1^2+(\omega_{sl}^e)^2)},\\
d_2 =& L_m+\frac{\omega_{sl}^e L_m\eta_1^2\beta_1}{\eta_1(\omega_{ref}+\omega_{sl}^e)(\eta_1^2+(\omega_{sl}^e)^2)}-\frac{(\omega_{sl}^e)^2 L_m\eta_1}{\eta_1(\eta_1^2+(\omega_{sl}^e)^2)}-\frac{(L_r\eta_3-\beta_1)}{\eta_3}.
\end{aligned}$$

Here, $x_1^e, \cdots, x_6^e$ are the states of the equilibrium point. Note that, remaining states of the equilibrium point $x_7^e, \cdots, x_{12}^e$ can also be obtained using (6.12) into the nonlinear model, though these are not required for the proposed controller design.

From (6.12), it is depicted that due to the presence of R_{fe} in IM core, coupling occurs in $i_{qs}, \psi_{dr}, \psi_{qr}, i_{dm}$ and i_{qm}. Hence, in steady-state, the developed torque T_e is not equivalent to torque command T_{re}. Such discrepancy results in larger i_{qs}, dependency on ω_r and violates the decoupling of flux d and torque q current components. The simulation results corresponding to iron loss is shown in Fig. 6.5. It is observed that due to iron loss, as T_L is applied or ω_{ref} is varied, transient as well as steady-state value of i_{qs} is affected. Defining

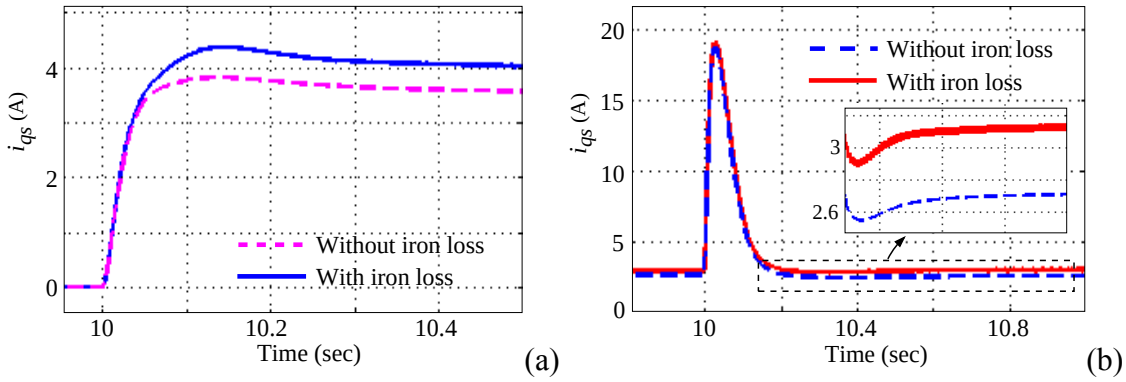

Figure 6.5: Iron loss affect on stator current i_{qs}: (a) i_{qs} with change in T_L (6.5 N·m). (b) i_{qs} with change in ω_{ref} (100 rad/sec to 140 rad/sec at $T_L = 5$ N·m).

the new state vector as $x_{spd}^T = \begin{bmatrix} x_{cur}^T & x_9 & \cdots & x_{12} \end{bmatrix}$, the linearized model of (6.2) along with the current-loop controller in the form (6.1) with (6.4) can be represented as:

$$\Delta\dot{x}_{spd} = A_{spd}\Delta x_{spd} + E_{spd}\Delta w_{spd} + B_{spd}\Delta u_{spd},\ \Delta y_{spd} = C_{spd}\Delta x_{spd} \tag{6.13}$$

where the disturbance input is considered as $\Delta w_{spd} = \begin{bmatrix} \Delta\delta x_1 & \cdots & \Delta\delta x_6 & \xi_1 & \cdots & \xi_5 & \Delta T_L \end{bmatrix}^T$. The corresponding system matrix can be

obtained as follows.

$$A_{spd} = \begin{bmatrix} A_{cur} + A_{o1} & A_{o2} \\ A_{o3} & A_{o4} \end{bmatrix},$$

$$A_{o1} = \begin{bmatrix} \begin{bmatrix} 0 & \omega_{ref} & \mathbf{0}_{1\times2} \\ -\omega_{ref} & 0 & \mathbf{0}_{1\times2} \\ \mathbf{0}_{2\times1} & \mathbf{0}_{2\times1} & \mathbf{0}_{2\times2} \end{bmatrix} & \mathbf{0}_{4\times4} \\ \mathbf{0}_{4\times4} & \begin{bmatrix} 0 & \omega_{ref} & \mathbf{0}_{1\times2} \\ -\omega_{ref} & 0 & \mathbf{0}_{1\times2} \\ \mathbf{0}_{2\times1} & \mathbf{0}_{2\times1} & \mathbf{0}_{2\times2} \end{bmatrix} \end{bmatrix},$$

$$A_{o2} = \begin{bmatrix} x_2^e & \frac{\sigma L_m x_2^e K_{i\omega}}{K_t \psi_{drref}^2} & \eta_4 c_d & 0 \\ -x_1^e & \frac{b_q K_{i\omega}}{K_t \psi_{drref}} - \frac{\sigma L_m x_1^e K_{i\omega}}{K_t \psi_{drref}^2} & 0 & \eta_4 c_d \\ 0 & \frac{\sigma L_m x_4^e K_{i\omega}}{K_t \psi_{drref}^2} & 0 & 0 \\ 0 & -\frac{\sigma L_m x_3^e K_{i\omega}}{K_t \psi_{drref}^2} & 0 & 0 \\ x_6^e & \frac{\sigma L_m x_6^e K_{i\omega}}{K_t \psi_{drref}^2} & 0 & 0 \\ -x_5^e & -\frac{\sigma L_m x_3^e K_{i\omega}}{K_t \psi_{drref}^2} & 0 & 0 \\ 0 & 0 & 0 & 0 \\ 0 & \frac{K_{i\omega}}{K_t \psi_{drref}} & 0 & 0 \end{bmatrix},$$

$$A_{o3} = \begin{bmatrix} \mathbf{0}_{2\times2} & \frac{K_m K_l}{J} \begin{bmatrix} -x_6^e & x_5^e & x_4^e & -x_3^e \\ 0 & 0 & 0 & 0 \end{bmatrix} & \mathbf{0}_{2\times2} \\ \begin{bmatrix} -b_d & 0 \\ 0 & -b_q \end{bmatrix} & \mathbf{0}_{2\times4} & \mathbf{0}_{2\times2} \end{bmatrix},$$

$$A_{o4} = \begin{bmatrix} -\frac{B_m}{J} & 0 & 0 & 0 \\ -1 & 0 & 0 & 0 \\ 0 & 0 & a_d & 0 \\ 0 & \frac{b_q K_{i\omega}}{K_t \psi_{drref}} & 0 & a_q \end{bmatrix}$$

The control input matrix B_{spd} is given in (6.14) and other matrices are given by

$$\begin{aligned} B_{spd} &= \begin{bmatrix} B_{spd1} & B_{spd2} \end{bmatrix}, \\ B_{spd1} &= \begin{bmatrix} \frac{\sigma L_m x_2^e}{K_t \psi_{drref}^2} & \frac{\eta_4 d_q}{K_t \psi_{drref}} - \frac{\sigma L_m x_1^e}{K_t \psi_{drref}^2} & \frac{\sigma L_m x_4^e}{K_t \psi_{drref}^2} & -\frac{\sigma L_m x_3^e}{K_t \psi_{drref}^2} & \frac{\sigma L_m x_6^e}{K_t \psi_{drref}^2} & -\frac{\sigma L_m x_5^e}{K_t \psi_{drref}^2} \end{bmatrix}^T, \\ B_{spd} &= \begin{bmatrix} 0 & \frac{1}{K_t \psi_{drref}} & 0 & 0 & 0 & \frac{b_q}{K_t \psi_{drref}} \end{bmatrix}^T. \end{aligned} \tag{6.14}$$

$$E_{spd} = \begin{bmatrix} E_{cur} & \mathbf{0}_{8\times1} \\ \mathbf{0}_{4\times8} & \begin{bmatrix} \frac{K_m}{J} & \mathbf{0}_{1\times3} \end{bmatrix}^T \end{bmatrix}, \; C_{spd} = \begin{bmatrix} \mathbf{0}_{4\times1} & -1 & \mathbf{0}_{7\times1} \end{bmatrix}$$

The state-space parameters of speed-loop dynamic controller of first-order $K_{\omega}(s)$ are taken as a_{ω}, b_{ω}, c_{ω}, d_{ω}.

Then augmenting (6.13) with the dynamic controller and carrying out algebraic manipulation, the closed-loop system can be represented as:

$$\dot{\tilde{x}}_{spd} = (\tilde{A}_{spd} + \tilde{B}_{spd}\tilde{F}_{spd}\tilde{C}_{spd})\tilde{x} + \tilde{E}_{spd}\tilde{w}_{spd} \tag{6.15}$$

where $\tilde{x}_{spd} = \begin{bmatrix}\Delta x_{spd}^T & \hat{x}_{spd}^T\end{bmatrix}^T$, $\hat{x}_{spd}$ is the controller state, $\tilde{w}_{spd} = \begin{bmatrix}w_{spd}^T & 0\end{bmatrix}^T$ and

$$\tilde{A}_{spd} = \begin{bmatrix} A_{spd} & \mathbf{0}_{12\times 1} \\ \mathbf{0}_{1\times 12} & 0 \end{bmatrix},\ \tilde{B}_{spd} = \begin{bmatrix} B_{spd} & \mathbf{0}_{12\times 1} \\ 0 & 1 \end{bmatrix},$$
$$\tilde{C}_{spd} = \begin{bmatrix} C_{spd} & 0 \\ \mathbf{0}_{1\times 12} & 1 \end{bmatrix},\ \tilde{F}_{spd} = \begin{bmatrix} d_{\omega} & c_{\omega} \\ b_{\omega} & a_{\omega} \end{bmatrix}.$$

Now, the output vector $z(t)$ is chosen so as to minimize the effect of $w(t)$ on the stator currents, rotor fluxes and speed of the motor. The corresponding choice is

$$\tilde{z}_{spd} = \tilde{G}_{spd}\tilde{x}_{spd} \tag{6.16}$$

where $\tilde{G}_{spd} = I$ is considered in this work.

The system model (6.15) along with (6.16) is used to design the speed-loop controller. Note that, the current-loop and the speed-loop dynamical controller design problems are formulated in same framework and one requires to design $\tilde{F}_{cur}$ (for the current-loop controller) and/or $\tilde{F}_{spd}$ (for the speed-loop controller), which are the dynamic feedback gain matrices. In addition, $\tilde{F}_{cur}$ is having a restricted structure than the usual full matrix in the form of a block-diagonal one. The design of such a restricted feedback matrix is treated in decentralized control theory framework. We adopt the same with the objective that one has to design $\tilde{F}_{cur}$ and $\tilde{F}_{spd}$ such that the effect of $\tilde{w}$ on $\tilde{z}$ is minimized.

Remark 1

The disturbance vector $\tilde{w}$ includes several disturbance elements. One may choose alter the disturbance consideration in the design by making a different choice, e.g. if only load disturbance effect to be minimized then $\tilde{w}$ should contain only the T_L term and the remaining disturbances can be enforced to zero. The corresponding modification is required to be made in the $\tilde{E}$ matrix. Similarly, one may choose the fictitious output $\tilde{z}(t)$ in order to select on which variables the disturbance effect is to be minimized. For current-loop design, $\tilde{z}$ may include only the i_{ds} and the i_{qs}, whereas, for the speed-loop controller, it may contain only the ω_r. The corresponding $\tilde{G}$ matrix need to be rewritten based on such choices.

Remark 2

Since the control problem formulated in the static output feedback framework and, particularly, keeping in view of the decentralized structure of the current-loop controller,

the above algorithm is seen to yield satisfactory result. However, it is well known that there exists no necessary and sufficient condition for designing static output feedback controller so far. To this effect, the above algorithm also yields controllers that are sufficient and hence conservative. One may use improved design methods for static output feedback controllers for improving the design and thereby controller performance. Also, several other possibilities or design methods can be attempted on the same state-space model, e.g. using different design methods for the two controllers, using a centralized structure of the current loop controller that are not possible for the conventional design methods.

Remark 3

The above algorithm yields a controller gain that ensures the disturbance rejection satisfying (4.23). The benefit of state-space model presented in this work can also be used to satisfy transient performances through pole placement in LMI region [152], which may further improve the dynamic performance of the controller.

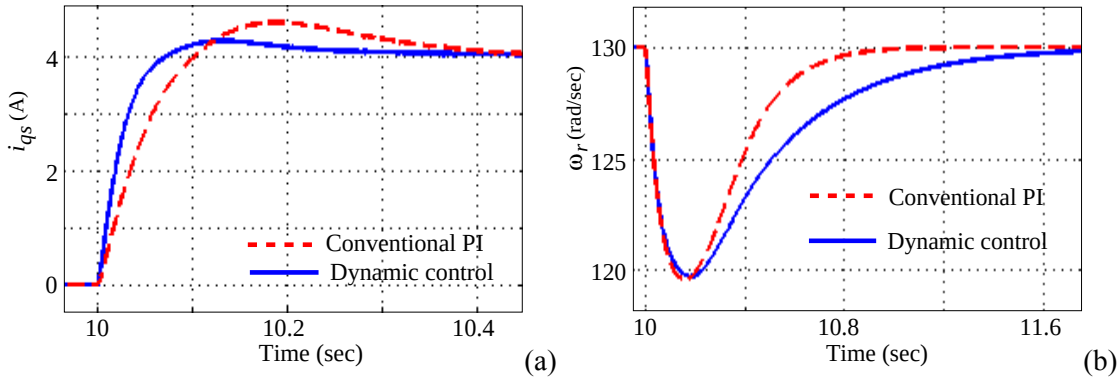

Figure 6.6: Comparison between proposed design and conventional PI when $T_L = 6.5$ N·m is applied at 10 sec for $\omega_{ref} = 130$ rad/sec: (a) Motor speed; (b) Stator current i_{qs}.

6.5 Performance Evaluation

6.5.1 Simulation Results

The available designs are carried out for the above setup neglecting the iron loss dynamics in the model. The corresponding motor parameters are given in Table 3.4. The PI design of [4] is first followed for the inner-loop controllers yielding $K_{pd} = 8.97$, $K_{pq} = 8.97$, $K_{id} = 1536$ and $K_{iq} = 2142$. Whereas, for the speed-loop controller, design of [94] yields $K_{p\omega} = 3.4$ and $K_{i\omega} = 34$. However, the speed gains are reset to $K_{p\omega} = 0.5$ and $K_{i\omega} = 1.5$ to avoid the IM non-starting. Also, these gains are found to achieve nominal control performance.

The integral gains for the proposed dynamic controller are chosen same as the one obtained for the PI controller above. The proposed dynamic controller is then designed using Algorithm 2 for the reference inputs as given in Table 4.1. After 40 and 5 iterations,

for inner and outer loop, respectively, these controllers are obtained as:

$$K_d(s) = K_q(s) = \frac{2.611s + 13.25}{s + 5.076}, K_\omega(s) = \frac{0.7363s + 1.047}{s + 1.422}$$

The simulation results of the proposed controller with a comparison to the conventional PI design approach are shown in Fig. 6.6 and Fig. 6.7. The comparison of two schemes for

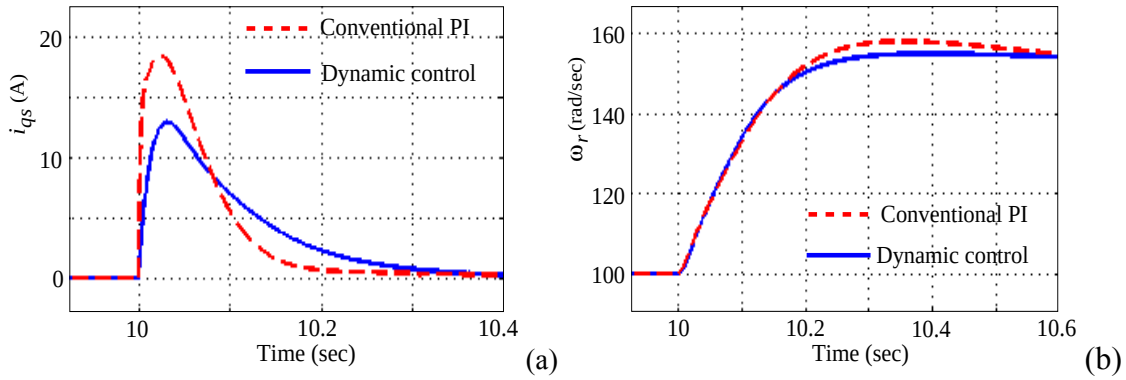

Figure 6.7: Comparison between proposed design and conventional PI when ω_{ref} is increased from 100 to 150 rad/sec: (a) Motor speed; (b) Stator current i_{qs}.

change in load is shown in Fig. 6.6. The observed ω_r with conventional one shows faster response but more undershoot as compared to proposed design. On the other hand, the stator current i_{qs} of the proposed design shows a better dynamic response (peak-overshoot and settling time) than the conventional PI.

In second case, a step change in ω_{ref} from 100 rad/sec to 150 rad/sec. Fig. 6.7 shows the robustness comparison of two schemes for change in speed from 100 rad/sec to 150 rad/sec. For the proposed design, ω_r shows smooth and fast convergence and less overshoot as compared to conventional one. It is accessed that the settling time in i_{qs} with the conventional one is better but shows large overshoot than the proposed design technique.

6.5.2 Experimental Test

The obtained controller design is validated on a test rig having a KIRLOSKAR make IM with motor parameters of Table 3.4. A dc generator (shunt type) is coupled to provide a load to IM. An infrared encoder is used to sense motor speed. The motor is powered from a SEMIKRON make inverter. The IVCIM operation is implemented using dSPACE 1103 board. The controller sampling frequency and sinusoidal pulse width modulation (SPWM) switching frequency are taken as 10 kHz and 5 kHz, respectively. The robustness on rotor resistance variation is tested for $\delta = 0.2\sigma$, which lies in limits of $-0.5\sigma < \delta < 0.41\sigma$ to ensure minimum phase condition [3].

The experiment is first carried out with the conventional PI design in the presence of rotor resistance perturbation as $\delta = 0$ and $\delta = 0.2\sigma$. This δ is changed in real time using a variable array tool in dSPACE control desk. The variation of i_{qs} and ω_r with sudden T_L

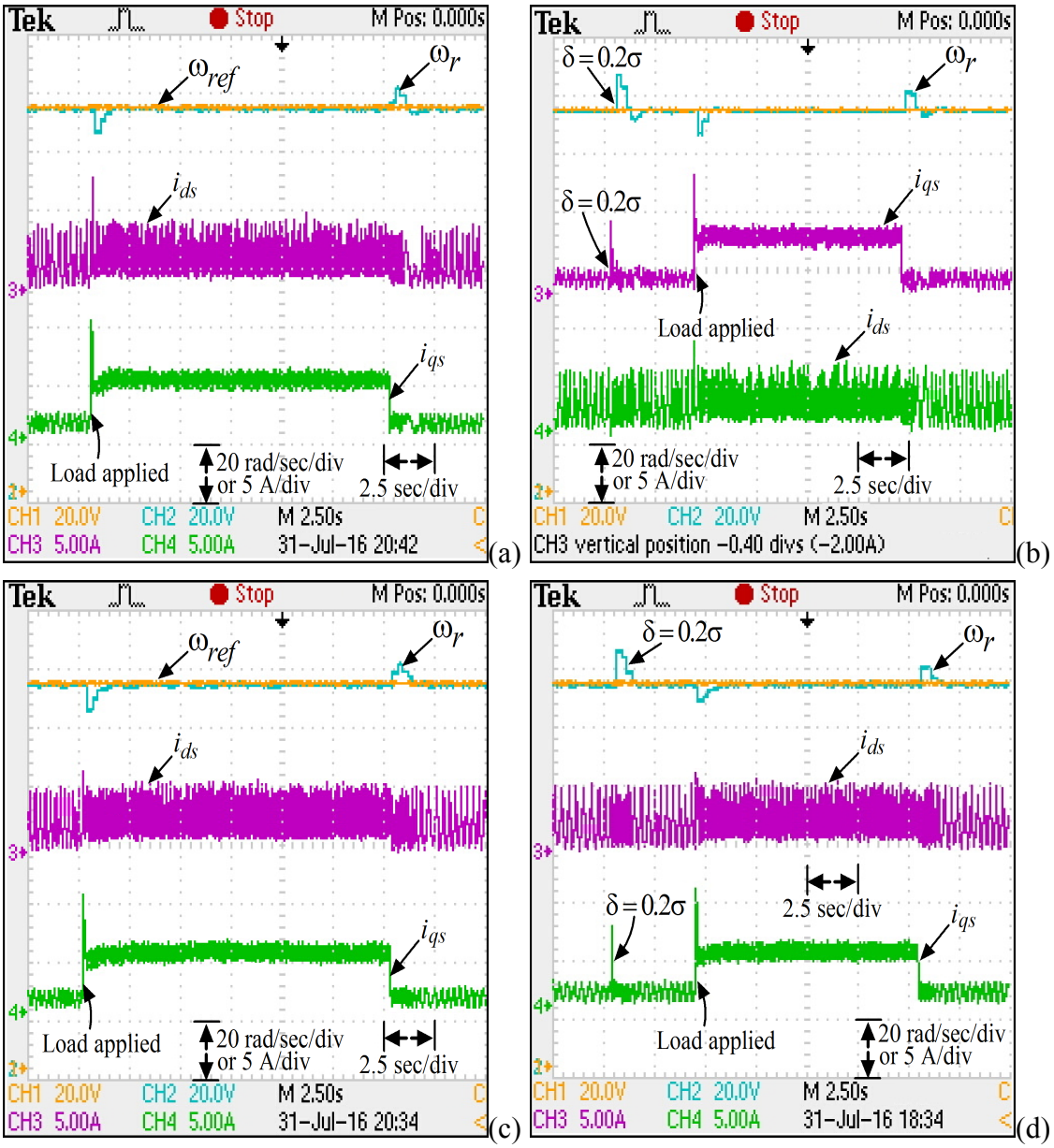

Figure 6.8: Experiment result for variation in T_L from 0 to 6.5 N·m at $\omega_{ref} = 130$ rad/sec: (a)-(b) Conventional PI. (c)-(d) Proposed design.

of approximate 6.5 N·m is shown in Fig. 6.8(a)-(b). It is depicted that, at $\delta = 0$, i_{ds} has large overshoot (Fig. 6.8(a)) and further, it is distorted as δ increases to 0.2σ (Fig. 6.8(b)). In addition, due to $\delta = 0.2\sigma$, i_{qs} and ω_r takes more time to settle at steady-state value. The load variation effect with the proposed controller is shown in Fig. 6.8(c)-(d). It is assessed that at $\delta = 0.2\sigma$, ω_r, i_{ds} and i_{qs} with the proposed controller show transient performance similar to $\delta = 0$.

The performance of the existing design [3] is also tested using the real time experiment. The corresponding controller is given in (6.17). For this experiment, speed-loop is controlled using the design of [3] and stator currents are controlled using proposed dynamical controller. However, the motor could not start. Hence, first, speed-loop is controlled using proposed

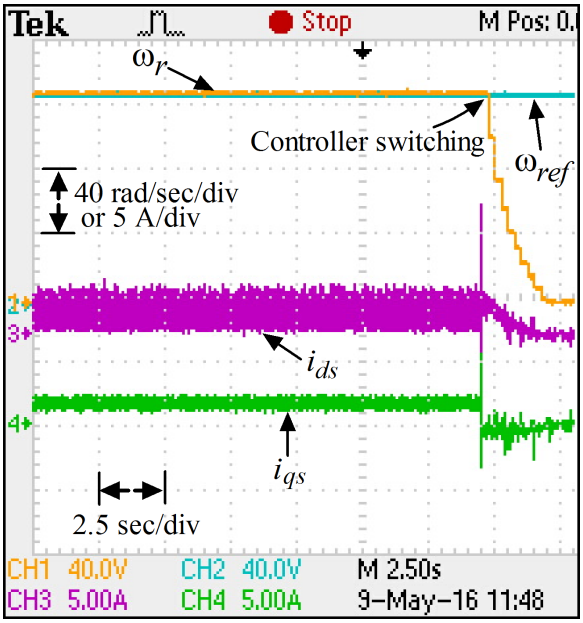

Figure 6.9: Experiment result for existing speed loop design [3] at $\omega_{ref} = 130$ rad/sec.

dynamic controller and then in steady-state, it is switched to (6.17). The corresponding result is shown in Fig. 6.9. It is observed that IM becomes unstable with (6.17).

$$C_{\omega}(s) = \frac{2(s+90)^2(s+22)}{s(s+210)(s+87)} \tag{6.17}$$

Next, the speed tracking performance between the conventional one and proposed design is compared. For this, ω_{ref} is changed in step from ($100 \rightarrow 150 \rightarrow 100$ rad/sec). The corresponding result is shown in Fig. 6.10(a)-(b). It is observed that ω_r of conventional PI oscillate with larger shoots, which is increased as δ is changed to 0.2σ. The shoot in i_{ds} and i_{qs} is also high. Whereas, ω_r and both stator currents show superior performance by the proposed design in Fig. 6.10(c)-(d). Note that, for low speed-loop bandwidth PI controller gains as $K_{p\omega} < 0.5$ and $K_{i\omega} < 1.5$, the motor response will be more deteriorated (larger settling time as observed in Fig. 5.11). The experimental results for high bandwidth gains $K_{p\omega} = 1$, $K_{i\omega} = 3$ is shown in Fig. 6.11(a). It is observed that for such gains, the settling time and shoot for ω_r are improved than that with the lower bandwidth gains. However, shoot in i_{ds} and i_{qs} are increased to higher values. On the other hand, motor response with dynamic design of neglected iron loss dynamics is shown in Fig. 6.11(b). It is observed that ω_r, i_{ds} and i_{qs} with dynamic one show better performance than that with the PI design. However, these currents show larger shoot and lesser smoothness than that with the full IM model (incorporating iron loss dynamics) based proposed controller.

The current tracking response for the proposed design is shown in Fig. 6.12(a)-(b). It is observed that both currents smoothly track the reference currents.

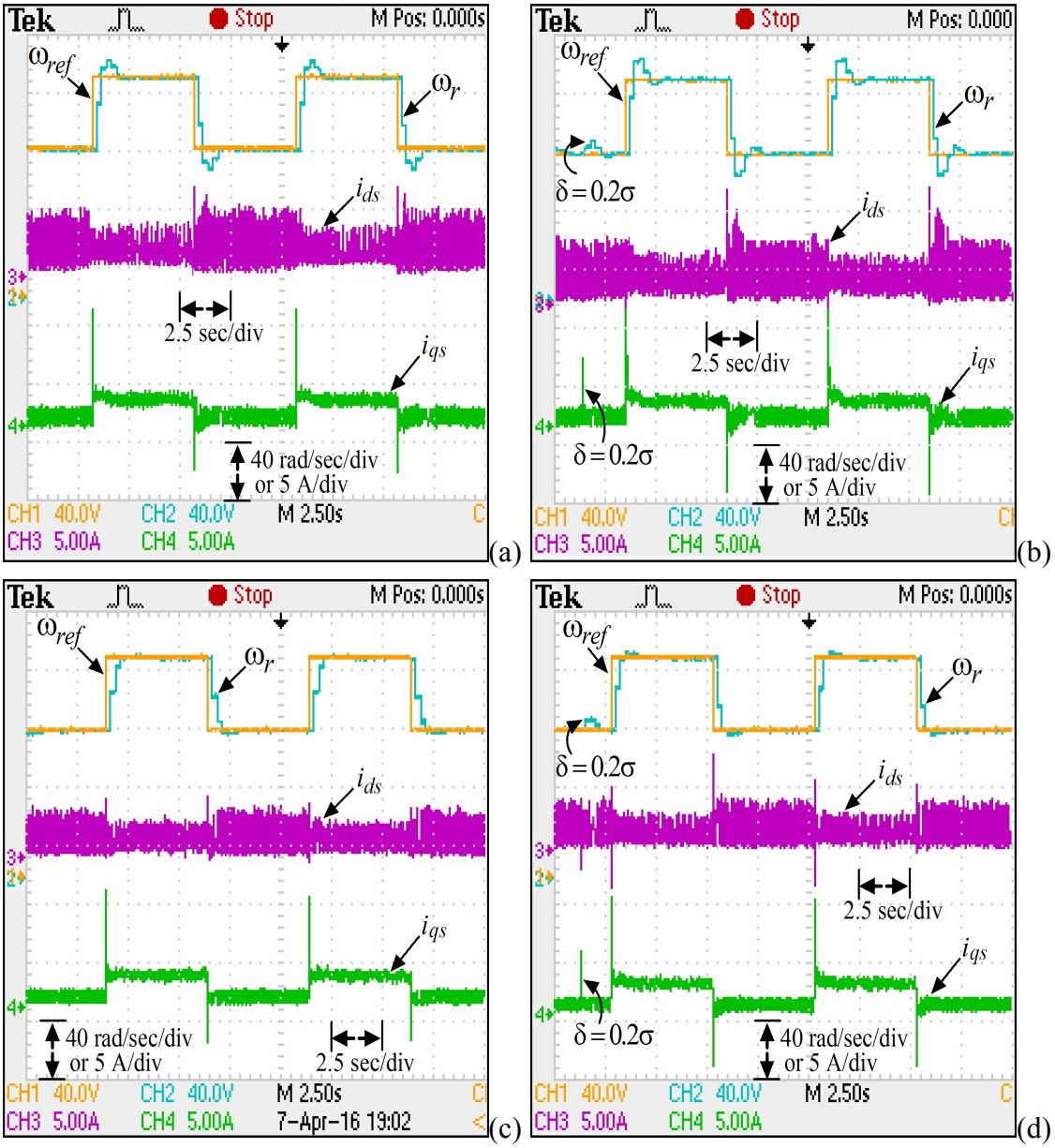

Figure 6.10: Experiment result for variation in ω_{ref} from 100 $\rightarrow$ 150 $\rightarrow$ 100 rad/sec: (a)-(b) Conventional PI. (c)-(d) Proposed design.

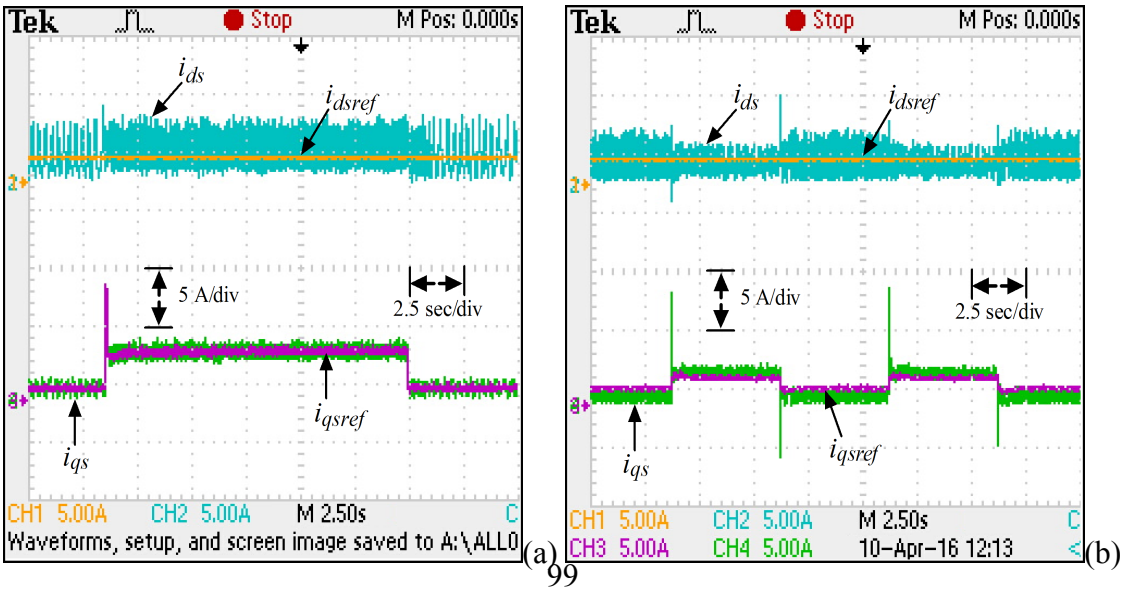

Figure 6.12: Experimental result of current tracking performance for change in: (a) T_L. (b) ω_{ref}.

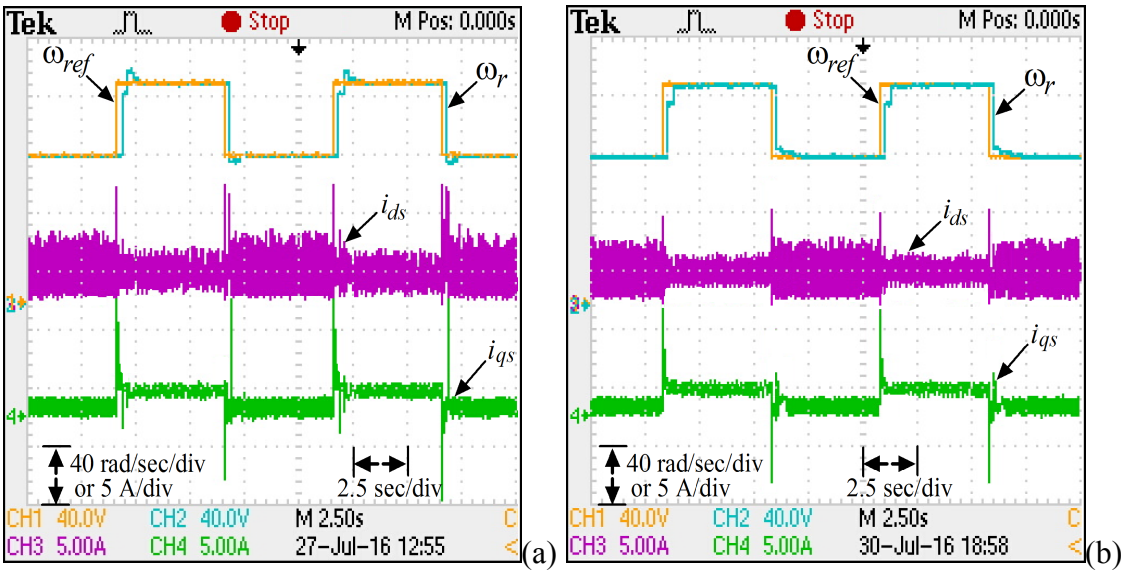

Figure 6.11: Experiment result for variation in ω_{ref} from $100 \rightarrow 150 \rightarrow 100$ rad/sec at $\delta = 0$: (a) Conventional with $K_{p\omega} = 1$, $K_{i\omega} = 3$. (b) Dynamic controller without considering iron loss dynamics.

6.6 Chapter Summary

In this work, a dynamic controller design is proposed for the IVCIM system. The controller is designed in a dynamic output feedback framework ensuring robust H_∞ performance. Iterative LMI algorithm is employed for the controller design. The simulation and experimental comparison show superiority of the proposed design over conventional PI on speed, rotor resistance, and load torque variations. In the next chapter, conclusion and future work directions of the proposed works are pointed out.

Chapter 7
Conclusion and Future work directions

7.1 Thesis summary

The prolonged operation of induction motor may change its parameters, e.g., rotor resistance, magnetizing inductance, etc. In vector control techniques, IVCIM is preferred over direct one as it is simpler, requires less computing power for transformations and yield high decoupled torque performance. However, the rotor resistance variation affects this decoupling and may lead to stability issues in IVCIM.

Stability analysis and controller design of the IVCIM is carried out in this thesis. Being inherently nonlinear, large-order and MIMO system, IVCIM poses multiple challenging problems, some of which have been addressed in this work. First, stability analysis through linearized system dynamics and bifurcation analysis due to rotor resistance variation have been carried out. Then, several different controller design methods based on state-space framework have been carried out. Such designs are new and provide superior performance with appropriate definition of performance measures. The same have been demonstrated through several simulation and experimental results. **Chapters 3-6** present new contributions that are made in this work.

7.2 Contribution of the Thesis

The rotor resistance variation induces perturbation in slip speed and cause detuning of IVCIM control operation. Such detuning affect the control performance and may lead to bifurcations, which may cause oscillation or high stator currents. The steady-state behavior of IVCIM can be improved by determining the bifurcation conditions and its dependence on controller gains. For such purpose, the following contributions are made in **Chapter 3**.

- Bifurcation analysis of a general (with time varying reference signal) as well as the classical IVCIM drive system has been carried out.
- The full-order nonlinear IM model has been used to analyze the IVCIM stability.
- Equilibrium point for the 8^{th} order IM model has been derived analytically.

- An algorithm has been constructed through which SNB and HB points are determined.
- HB condition at any loading condition has been studied in detail that can be exploited to obtain limits of outer speed-loop gains to avoid bifurcation.
- Effect of subestimation of rotor resistance on general IVCIM has been analyzed.
- Occurrence of complex bifurcation phenomenon, such as BTB, ZHB and effect of speed-loop gain variation on such bifurcations have also been studied.
- Experimental validation of SNB and HB has also been presented.

For better regulating performance of IVCIM, inner current and outer speed-loop must be tuned properly. This tuning becomes significant in the presence of rotor resistance and load torque variations. In **Chapter 4**, for improving the dynamic performance and overcoming the limitations of individual designs of all the loops, a concurrent design method for IVCIM system is proposed. The following contributions are made in this work:

- A multiple-input and multiple-output (MIMO) static output feedback (SOF) based closed-loop control structure has been framed in order to account for the concurrent PI design of the speed and current-loop controllers in synchronous rotating reference frame.
- The rotor resistance variation and the load torque have been considered as disturbances.
- An iterative linear matrix inequality (ILMI) based H_∞ control design technique has been employed to design the PI gains.
- A comparison of the present design with the existing one through simulation and experimental results has been demonstrated.

The stator currents of the IM are coupled to each other. The torque response is affected by coupling between these currents. The decoupling schemes, e.g., feedforward decoupling, modified PI controllers, etc., induce complexity and burden on signal processing in the conventional IVCIM system. To mitigate the coupling, the below contributions are constructed in **Chapter 5**:

- The sensitivity of the stator currents has been determined on current controller gains.
- The decoupling effect has been treated as a performance criterion for current-loop controller design.
- For the purpose, a MIMO SOF based closed-loop structure has been formulated for the linearized model of the IVCIM.

- An ILMI based controller design technique has been applied to design the PI gains.
- Simulation and experimental results have been presented that corroborates the effectiveness of the proposed controller design technique as compared to the conventional feedforward decoupling one.

Using the PI controller, a smooth dynamic performance for IVCIM is hard to obtain on sharp changes in reference quantities, e.g., reference motor speed, load torque. The performance is also degraded due to the presence of rotor resistance variation. In addition, the iron loss in IM core also affects the IVCIM performance. To improve this, the following contributions are framed in **Chapter 6**:

- A performance based dynamic controller design has been proposed for IVCIM.
- For better performance, the iron loss dynamics have been incorporated in IM model.
- First, the inner-loop dynamic controller has been designed in synchronous rotating reference frame.
- After obtaining the controller gains, it has been incorporated in the outer speed-loop design.
- The rotor resistance variation, load torque and uncertainty due to iron loss have been considered as disturbances.
- A MIMO dynamic output feedback (DOF) based closed-loop structure has been framed in order to account for the controller design.
- An ILMI based H_∞ control design technique has been employed to design the gains.
- A performance comparison of the proposed and the conventional PI controller has been demonstrated through simulation and experimental results.

7.3 Future Research Directions

Future works may be carried out on the following issues.

1. The bifurcation behavior is not limited to three-phase IM only, the same has also been observed in vector controlled five-phase induction motor and doubly fed induction generator. The present analysis may be extended to such cases in future.
2. The present bifurcation analysis is carried out for PI-controlled IVCIM, the same can be easily employed for other linear controllers with necessary changes in the controller model. For example, the same evaluation procedure can be followed on an LTI speed-controller.

3. Certain dynamics, e.g., inverter, motor losses, controller response delay, motor response delay, dc generator dynamics, etc., can be added to the IVCIM model that may improve the controller performance.

4. The coupling minimization problem can be appended with parameter variations that affects the IVCIM performance considerably. Moreover, for improving the bandwidth of decoupling current controllers, the desired states can be added to the performance output variable.

5. The dynamic controller design can be addressed to coupling minimization problem. Moreover, this controller design technique can be applied to other AC machines, e.g., permanent magnet synchronous motor.

6. The proposed output feedback techniques (static and dynamic) can be combined with other controller designs to yield better performance, e.g., predictive control.

Chapter A

Nonlinear Dynamical System

A nonlinear system is a set of nonlinear equations (algebraic, difference, differential, integral, functional, or abstract operator equations, etc.) used to describe a physical model. This theory has found applications in physics, chemistry, mathematics, biology, medicine, economics, and various engineering disciplines [153] due to the reason that all physical dynamical systems are inherently nonlinear to certain extent. A nonlinear autonomous system can be represented by the following.

$$\dot{x}(t) = f(x(t), u(t)) \tag{A.1}$$

where x is a vector of states and u is the external input.

A.1 Equilibrium point

An equilibrium point of the system is the point where once the system state reaches, it stays forever there till it is not externally perturbed. It can be formalized as $x = x^e$ is an equilibrium for $\dot{x}(t) = f(x(t))$ if $f(x^e) = 0$.

Example *Logistic Growth Model [89]*

$$\dot{x}(t) = r\left(1 - \frac{x(t)}{K}\right)x(t) \tag{A.2}$$

where $r > 0$, $K > 0$, $x > 0$ denotes the population and K is called the carrying capacity. For the scalar system $x(t) \in R$, stability can be determined from the sign of $f(x(t))$ around the equilibrium point. Here (A.2) is unstable for $x = 0$ and stable for $x(t) = K$.

A.2 Linear System

A system is a linear if it follows the property of the superposition and homogeneity. A linear time invariant (LTI) system with input $u(t)$ can be represented as

$$\dot{x}(t) = Ax(t) + Bu(t) \tag{A.3}$$

where A is called the system matrix and B is the input matrix.

An LTI system has the following properties [153].

1. It has an unique equilibrium point if A is nonsingular.
2. If A is singular, the nullspace defines a continuum of equilibria.
3. If all eigenvalues of A have negative real parts, with respect to any initial conditions, the equilibrium point is stable
4. Its general solution can be obtained analytically

A.3 Linearization

A nonlinear system behavior can be analyzed with an approximate solution. One method to find approximate solutions is by linearization around the equilibrium point. This method is exploits local stability property of the system around the equilibrium point. The Local stability properties of the equilibrium point x^e can be determined by linearizing the vector field $f(x)$ at x^e as (by using Taylor's expansion):

$$f(x^e + \Delta x(t)) = f(x^e) + \frac{\partial f(x(t))}{\partial x(t)} \mid_{x=x^e} \Delta x(t) + \text{Higher order terms} \tag{A.4}$$

Since $f(x^e) = 0$, the linearized model is $\dot{\Delta} x(t) = A\Delta x(t)$.

Here, if $\Re\lambda_i(A) < 0$ for each of the eigenvalues λ_is of A then x^e is asymptotically stable. Whereas, if $\Re\lambda_i(A) > 0$ for some eigenvalues λ_is of A then x^e is unstable.

Example *Pendulam [88]*

$$\begin{aligned} \dot{x}_1 =& x_2 \\ x_2(t) =& -\frac{k}{m}x_2(t) - \frac{g}{l}sinx_1(t) \end{aligned} \tag{A.5}$$

Above (A.7) has two equilibria (0,0) and (π,0). The linearized system for (A.7) can be written as

$$\begin{bmatrix} \Delta\dot{x}_1(t) \\ \Delta\dot{x}_2(t) \end{bmatrix} = \begin{bmatrix} 0 & 1 \\ -\frac{g}{l}cosx_1(t) & -\frac{k}{l} \end{bmatrix} \begin{bmatrix} \Delta x_1(t) \\ \Delta x_2(t) \end{bmatrix} \tag{A.6}$$

It can be seen that (A.6) is stable for $x_1^e = 0$ and unstable for $x_1^e = \pi$, which is also evident from its physical behavior of the two equilibrium point.

A.4 Characteristics of Nonlinear System

A nonlinear system behavior is complex compared to the linear one. It is characterized by multiple equilibrium point, limit cycles, finite escape time, bifurcations and chaos phenomenon. Since the IM model (2.20) considered in this work is a nonlinear one, it is

important to understand such phenomenon for analyzing the system behavior and possibly avoiding dangerous phenomena.

A.4.1 Multiple Isolated Equilibrium Points

A linear system can have only one isolated equilibrium point or a continuum. Therefore, it can have only one steady-state operating point that attracts the states of the system irrespective of the initial state. Whereas, a nonlinear system can have more than one isolated equilibrium point, e.g., pendulam system (A.6) has two isoloated equilibria (one stable and one unstable). The state may converge to one of several steady-state operating points, which depends on the initial state of the system.

A.4.2 Limit Cycles

In real life, stable oscillations are produced by the nonlinear systems. These systems can generate oscillations of fixed amplitude and frequency, irrespective of the initial state. This type of oscillation is known as limit cycles. Limit cycles in nonlinear systems are different from linear oscillations in a number of fundamental aspects. First, the amplitude of the self-sustained oscillations is independent of the initial condition. On the other hand, the oscillation of a marginally stable linear system has its amplitude determined by its initial conditions. Second, marginally stable linear systems are very sensitive to changes in system parameters whereas limit cycles for nonlinear systems are not easily affected by the parameter changes.

Example *Van der pol oscillator [88]*

$$\begin{aligned} \dot{x}_1(t) =& x_2(t) \\ \dot{x}_2(t) =& -x_1(t) + \alpha(1 - x_1^2(t))x_2(t) \end{aligned} \tag{A.7}$$

When $\alpha = 0$, we have a continuum of periodic solutions, while in the case $\alpha \neq 0$ there is only one. The corresponding behavior for various initial conditions is shown in Fig. A.1. It is observed that for all initial conditions, the states converges to a periodic orbit, which

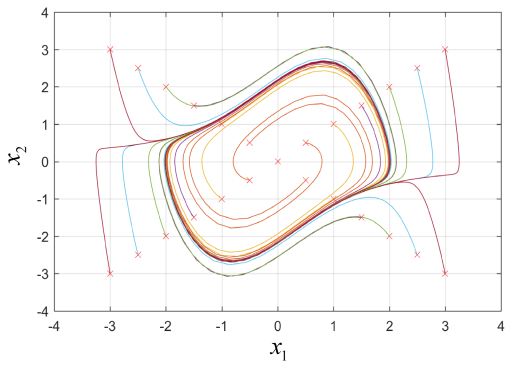

Figure A.1: Limit cycle behavior.

represent a limit cycle behavior.

A.4.3 Finite Escape Time

The state of an unstable linear system goes to infinity as time approaches infinity. Whereas, a nonlinear system's state can go to infinity in finite time.

Example Consider the following nonlinear system.

$$\dot{x}(t) = x^2(t) \tag{A.8}$$

The solution of (A.8) can be determined as

$$x(t) = \frac{1}{\frac{1}{x_0} - t} \tag{A.9}$$

It can be seen that $x(t) \to \infty$ within finite time.

A.4.4 Bifurcations

As the parameters of nonlinear dynamic systems are changed, the stability of the equilibrium point may change (as it does in linear systems). Also, the number of equilibrium points may change for nonlinear systems. Values of these parameters at which the qualitative nature of the system's motion changes are known as critical or bifurcation values. The fundamental bifurcations can be defined as follows [89, 90, 154, 155].

Saddle Node Bifurcation (SNB)

In this bifurcation, equilibrium points are created and destroyed. As the bifurcation parameter varies, the equilibrium points come nearby, collide and annihilate.

For this bifurcation, eigenvalues crosses through the origin and become positive. It can be understand by the following example.

$$\begin{aligned} \dot{x}_1(t) =& \alpha - x_1^2(t), \\ \dot{x}_2(t) =& - x_2(t) \end{aligned} \tag{A.10}$$

At $\alpha > 0$, two fixed point exist for (A.10) as stable node $(\sqrt{\alpha}, 0)$ and saddle $(-\sqrt{\alpha}, 0)$. Here x^e varies with α. Therefore, α is a bifurcation parameter. As α is changed from negative to zero, equilibrium points are changed from two to one. Further change in α to a positive value leads to unstable behavior since equilibrium point vanishes. The corresponding Jacobian matrix is given by

$$A = \begin{bmatrix} -2\sqrt{\alpha} & 0 \\ 0 & -1 \end{bmatrix} \tag{A.11}$$

The eigenvalues of the above matrix A is obtained as:

$$\lambda = -2\sqrt{\alpha}, -1 \tag{A.12}$$

Here one eigenvalues varies with α. The corresponding eigenvalue variation is shown in Fig. A.2.

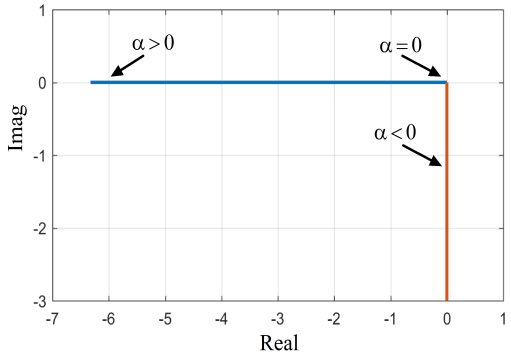

Figure A.2: Variation of eigenvalue for SNB.

It is observed that at $alpha > 0$, eigenvalues is negative, hence system is stable. Further, at $\alpha = 0$, eigenvalue becomes zero and for $\alpha < 0$, system becomes unstable since equilibrium point vanishes.

Hopf Bifurcation (HB)

This bifurcation connects equilibria with periodic motion. In this bifurcation, sustained oscillations are appeared when the system's parameters move from the critical condition.

The HB phenomenon is demonstrated by the following example.

$$\begin{aligned} \dot{r}(t) =& r(\alpha - r^2(t)) \\ \dot{\theta}(t) =& \omega + br^2(t) \end{aligned} \tag{A.13}$$

The three parameters, α, ω and b determines the nonlinear behavior of the system. At the origin, the Jacobian matrix of (A.16) is determined as

$$A = \begin{bmatrix} \alpha & -\omega \\ \omega & \alpha \end{bmatrix} \tag{A.14}$$

The eigenvalues of the above matrix A is obtained as:

$$\lambda = \alpha \pm i\omega \tag{A.15}$$

It can be seen that the eigenvalues are negative for $\alpha < 0$, becomes imaginary as $\alpha = 0$ and further increment in α causes system instability since eigenvalues becomes positive as crosses through the imaginary axis. The corresponding eigenvalue variation for $\omega = 2$ is shown in Fig. A.3.

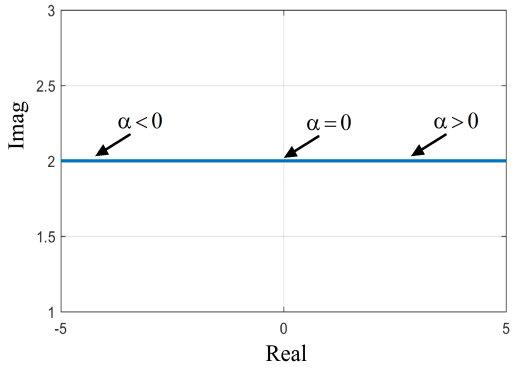

Figure A.3: Variation of eigenvalue for HB.

It is observed that eigenvalue crosses through the imaginary axis as α increases from zero. The HB condition for a dynamical system can be summarized as:

1. At the equilibrium point, the Jacobian matrix has only simple imaginary eigenvalues $\pm i$ with no other eigenvalues on the imaginary axis.

2. **Transversality Condition**: The change in sign of the real part of the complex eigenvalue takes place as it passes through the HB point. This condition is termed as transversality $\frac{\mathrm{d}(Re(\lambda(\alpha_H)))}{\mathrm{d}\alpha} \neq 0$ where λ is the eigenvalue of the system and α_H is the HB point. It guarantees that the eigenvalues crosses the imaginary axis as α (bifurcation parameter) varies.

Bogdanov Takens Bifurcaion (BTB)

In this bifurcation, two real eigenvalues simultaneously crosses imaginary axis. This singularity introduces the multiplicity of equilibrium solutions and the appearance of an oscillatory branch via the HB mechanism. An example of a dynamical system having such kind of bifurcation is given as:

$$\begin{aligned} \dot{x}_1(t) =& x_2(t) \\ \dot{x}_2(t) =& \alpha_1 + \alpha_2 x_1(t) + x_1^2(t) + x_1(t)x_2(t) \end{aligned} \tag{A.16}$$

Here, (A.16) has one state's equilibrium at zero and the other one follows solution of a quadratic equation. The solution of quadratic equation yields a condition for the existence of the equilibrium point and BTB.

Zero Hopf Bifurcation (ZHB)

In ZHB, system has the equilibrium $x = 0$ with one zero eigenvalue $\lambda_1 = 0$ and a pair of pure imaginary eigenvalues $\lambda_{2,3} = \pm i$. An example of dynamical system for ZHB is given

as follows:

$$\begin{aligned}\dot{x}_1(t) =& \alpha_1 + x_1^2(t) + a x_2^2(t) \\ \dot{x}_2(t) =& x_2(t)(\alpha_2 + b x_1(t) + x_1^2(t))\end{aligned} \tag{A.17}$$

For $x_2(t) = 0$, two equilibrium points exist for $x_1(t)$ state as a function of α_1. Whereas, for $x_2(t) > 0$, a nontrivial equilibrium point appears as a quadratic function of α_1 and α_2. As these parameters vary, one eigenvalue crosses through the origin and the other two eigenvalues cross through the imaginary axis that represent ZHB.

References

[1] D. G. Holmes, B. P. McGrath, and S. G. Parker, "Current regulation strategies for vector-controlled induction motor drives," *IEEE Trans. Ind. Electron.*, vol. 59, no. 10, pp. 3680–3689, Oct. 2012.

[2] P. Alkorta, O. Barambones, J. A. Cortajarena, and A. Zubizarrreta, "Efficient multivariable generalized predictive control for sensorless induction motor drives," *IEEE Trans. Ind. Electron.*, vol. 61, no. 9, pp. 5126–5134, Sep. 2014.

[3] L. A. Brooks, J. L. Castro, and E. L. Castro, "Speed and position controllers using indirect field-oriented control:a classical control approach," *IEEE Trans. Ind. Electron.*, vol. 61, no. 4, pp. 1928–1943, April. 2014.

[4] M. Comanescu, L. Xu, and T. Batzel, "Decoupled current control of sensorless induction-motor drives by integral sliding mode," *IEEE Trans. Ind. Electron.*, vol. 55, no. 11, pp. 3836–3845, Nov. 2008.

[5] W. Leonhard, *Control of Electrical Drives*. Springer-Verlag, 1990.

[6] B. K. Bose, *Power Electronics and AC Drives*. Englewood Cliffs, NJ: Prentice-Hall, 1987.

[7] R. Krishnan and F. C. Doran, "Study of parameter sensitivity in high performance inverter-fed induction motor drive systems," *IEEE Trans. Industry Appl.*, vol. IA-23, no. 4, pp. 623–635, July/August 1987.

[8] P. A. S. De Wit, R. Ortega, and I. Mareels, "Indirect field-oriented control of induction motors is robustly globally stable," *Automatica*, vol. 32, no. 10, pp. 1393–1402, Feb/March 1996.

[9] A. S. Bazanella and R. Reginatto, "Robustness margins for indirect field oriented control of induction motors," *IEEE Trans. Autom. Control*, vol. 45, no. 6, pp. 1226–1231, June 2000.

[10] B. Karanayil, M. F. Rahman, and C. Grantham, "Online stator and rotor resistance estimation scheme using artificial neural networks for vector controlled speed sensorless induction motor drive," *IEEE Trans. Ind. Electron.*, vol. 54, no. 1, pp. 167–176, Feb. 2007.

[11] S. Maiti and C. Chakraborty, "Model reference adaptive controller-based rotor resistance and speed estimation techniques for vector controlled induction motor drive utilizing reactive power," *IEEE Trans. Ind. Electron.*, vol. 55, no. 2, pp. 594–601, Feb. 2008.

[12] C. M. Verrelli, A. Savoia, M. Mengoni, R. Marino, P. Tomei, and L. Zarri, "On-line identification of winding resistances and load torque in induction machines," *IEEE Trans. Control Syst. Technol.*, vol. 22, no. 4, pp. 1629–1637, Jul. 2014.

[13] A. S. Bazanella and R. Reginatto, "Robust tuning of the speed loop in indirect field oriented control of induction motors," *Automatica*, vol. 37, no. 11, pp. 1811–1818, April 2001.

[14] F. Gordillo, F. Salas, R. Ortega, J. Aracil, and R. Reginatto, "Hopf bifurcation in indirect field-oriented control of induction motors," *Automatica*, vol. 38, no. 5, pp. 829–835, May 2002.

[15] F. Salas, F. Gordillo, J. Aracil, and R. Reginatto, "Codimension-two bifurcations in indirect field oriented control of induction motor drives," *Int. J. Bifurcation and Chaos*, vol. 18, no. 3, pp. 779–792, June 2008.

[16] Y. Gao and K. T. Chau, "Chaotification of induction motor drives under periodic speed command," *Elect. Pow. Comp. and Syst.*, vol. 31, no. 11, pp. 1083–1099, 2003.

[17] K. T. Chau and Z. Wang, *Chaos in Electric Drive Systems: Analysis, Control and Application*. John Wiley and Sons (Asia) Pte Ltd., 2011.

[18] A. Bedr Ozer and E. Akin , "Chaos control in vector-controlled induction motor drive," *Elect. Pow. Comp. and Syst.*, vol. 36, no. 7, pp. 733–740, 2008.

[19] J. Rodriguez, R. M. Kennel, J. R. Espinoza, M. Trincado, C. A. Silva, and C. A. Rojas, "High-performance control strategies for electrical drives: An experimental assessment," *IEEE Trans. Ind. Electron.*, vol. 59, no. 2, pp. 812–820, 2012.

[20] J. Jung and K. Nam, "A vector control scheme for EV induction motors with a series iron loss model," *IEEE Trans. Ind. Electron.*, vol. 45, no. 4, pp. 617–624, Aug. 1998.

[21] M. Boussak and K. Jarray, "A high-performance sensorless indirect stator flux orientation control of induction motor drive," *IEEE Trans. Ind. Electron.*, vol. 53, no. 1, pp. 41–49, Feb 2006.

[22] T. M. Rowan, R. J. Kerkman, and D. Leggate, "A simple on-line adaption for indirect field orientation of an induction machine," *IEEE Trans. Industry Appl.*, vol. 27, no. 4, pp. 720–727, July/Aug. 1991.

[23] G. Kenne, T. A. -Ali, F. L. -Lagarrigue, and A. Arzande, "Real-time speed and flux adaptive control of induction motors using unknown time-varying rotor resistance and load torque," *IEEE Trans. Energy Convers.*, vol. 24, no. 2, pp. 375–387, Jun. 2009.

[24] T. M. Jahns, "Motion control with permanent-magnet AC machines," *Proc. IEEE*, vol. 82, no. 8, pp. 1241–1252, Aug. 1994.

[25] P. C. Sen , *Principles of electric machines and power electronics*. John Wiley & Sons, 2007.

[26] R. Lessmeier, W. Schumacher, and W. Leonhard, "Microprocessor-controlled AC-servo drives with synchronous or induction motors: Which is preferable?" *IEEE Trans. Industry Appl.*, vol. IA-22, no. 5, pp. 812–819, Sep. 1986.

[27] R. D. Lorenz, T. A. Lipo, and D. W. Novotny, "Motion control with induction motors," *Proc. IEEE*, vol. 82, no. 8, pp. 1215–1240, Aug. 1994.

[28] R. Gabriel, W. Leonhard, and C. J. Nordby, "Field-oriented control of a standard AC motor using microprocessors," *IEEE Trans. Industry Appl.*, vol. IA-16, no. 2, pp. 186–192, Mar. 1980.

[29] W. Leonhard, "Microcomputer control of high dynamic performance ac-drives—a survey," *Automatica*, vol. 22, no. 1, pp. 1–19, Jan. 1986.

[30] Y. Y. Tzou and H. J. Wu, "Multimicroprocessor-based robust control of an AC induction servo motor," *IEEE Trans. Industry Appl.*, vol. 26, no. 3, pp. 441–449, May 1990.

[31] H. L. –Huy, "Microprocessors and digital ICs for motion control," *Proc. IEEE*, vol. 82, no. 8, pp. 1140–1163, Aug. 1994.

[32] Y. -Y. Tzou, "DSP-based robust control of an AC induction servo drive for motion control," *IEEE Trans. Control Syst. Technol.*, vol. 4, no. 6, pp. 614–626, Nov. 1996.

[33] P. C. Krause, O. Wasynczuk, and S. D. Sudhoff, *Analysis of Electric Machinery and Drive Systems*. Wiley India, 2004.

[34] B. K. Bose, "Scalar decoupled control of induction motor," *IEEE Trans. Industry Appl.*, vol. IA-20, no. 1, pp. 216–225, Jan. 1984.

[35] A. S. –Ahmed and N. A. O. Demerdash, "Fault-tolerant operation of delta-connected scalar- and vector-controlled AC motor drives," *IEEE Trans. Power Electron.*, vol. 27, no. 6, pp. 3041–3049, Jun. 2012.

[36] I. Kioskeridis and N. Margaris, "Loss minimization in scalar-controlled induction motor drives with search controllers," *IEEE Trans. Power Electron.*, vol. 11, no. 2, pp. 213–220, Mar. 1996.

[37] M. Suetake, I. N. d. Silva, and A. Goedtel, "Embedded DSP-based compact fuzzy system and its application for induction-motor v/f speed control," *IEEE Trans. Ind. Electron.*, vol. 58, no. 3, pp. 750–760, Mar. 2011.

[38] C. –C. Wang and C. –H. Fang, "Sensorless scalar-controlled induction motor drives with modified flux observer," *IEEE Trans. Energy Convers.*, vol. 18, no. 2, pp. 181–186, Jun. 2003.

[39] B. K. Bose, "Scalar decoupled control of induction motor," *IEEE Trans. Industry Appl.*, vol. IA-20, no. 1, pp. 216–225, Jan. 1984.

[40] X. Fu and S. Li, "A novel neural network vector control technique for induction motor drive," *IEEE Trans. Energy Convers.*, vol. 30, no. 4, pp. 1428–1437, Dec. 2015.

[41] R. Gunabalan, P. S. kumar, F. Blaabjerg, O. Ojo, and V. Subbiah, "Analysis and implementation of parallel connected two-induction motor single-inverter drive by direct vector control for industrial application," *IEEE Trans. Power Electron.*, vol. 30, no. 12, pp. 6472–6475, Dec. 2015.

[42] M. Wolkiewicz, G. Tarchała, T. O. -Kowalska, and C. T. Kowalski, "Online stator interturn short circuits monitoring in the DFOC induction-motor drive," *IEEE Trans. Ind. Electron.*, vol. 63, no. 4, pp. 2517–2528, Apr. 2016.

[43] D. Stojić, M. Milinković, S. Veinović, and I. Klasnić, "Improved stator flux estimator for speed sensorless induction motor drives," *IEEE Trans. Power Electron.*, vol. 30, no. 4, pp. 2363–2371, Apr. 2015.

[44] A. M. Bazzi, V. T. Buyukdegirmenci, and P. T. Krein, "System-level power loss sensitivity to various control variables in vector-controlled induction motor drives," *IEEE Trans. Industry Appl.*, vol. 49, no. 3, pp. 1367–1373, May 2013.

[45] A. K. Abdelsalam, M. I. Masoud, M. S. Hamad, and B. W. Williams, "Modified indirect vector control technique for current-source induction motor drive," *IEEE Trans. Industry Appl.*, vol. 48, no. 6, pp. 2433–2442, Nov. 2012.

[46] H. B. Shin and J. G. Park, "Anti-windup PID controller with integral state predictor for variable-speed motor drives," *IEEE Trans. Ind. Electron.*, vol. 59, no. 3, pp. 1509–1516, Mar. 2012.

[47] A. N. Smith, S. M. Gadoue, and J. W. Finch, "Improved rotor flux estimation at low speeds for torque MRAS-based sensorless induction motor drives," *IEEE Trans. Energy Convers.*, vol. 31, no. 1, pp. 270–282, Mar. 2016.

[48] Y. B. Zbede, S. M. Gadoue, and D. J. Atkinson, "Model predictive MRAS estimator for sensorless induction motor drives," *IEEE Trans. Ind. Electron.*, vol. 63, no. 6, pp. 3511–3521, June 2016.

[49] M. Comanescu and L. Xu, "An improved flux observer based on PLL frequency estimator for sensorless vector control of induction motors," *IEEE Trans. Ind. Electron.*, vol. 53, no. 1, pp. 50–56, Feb. 2005.

[50] M. Uddin and M. Hafeez, "FLC-based DTC scheme to improve the dynamic performance of an IM drive," *IEEE Trans. Industry Appl.*, vol. 48, no. 2, pp. 823–831, Mar. 2012.

[51] B. E. Badsi, B. Bouzidi, and A. Masmoudi, "Bus-clamping-based DTC: An attempt to reduce harmonic distortion and switching losses," *IEEE Trans. Ind. Electron.*, vol. 60, no. 3, pp. 873–884, Mar. 2013.

[52] Y. Zhang, J. Zhu, Z. Zhao, W. Xu, and D. G. Dorrell, "An improved direct torque control for three-level inverter-fed induction motor sensorless drive," *IEEE Trans. Power Electron.*, vol. 27, no. 3, pp. 1502–1513, Mar. 2012.

[53] B. E. Badsi, B. Bouzidi, and A. Masmoudi, "DTC scheme for a four-switch inverter-fed induction motor emulating the six-switch inverter operation," *IEEE Trans. Power Electron.*, vol. 28, no. 7, pp. 3528–3538, Jul. 2013.

[54] N. V. Naik and S. P. Singh, "A comparative analytical performance of F2DTC and PIDTC of induction motor using DSPACE-1104," *IEEE Trans. Ind. Electron.*, vol. 62, no. 12, pp. 7350–7359, Dec. 2015.

[55] V. N. N, A. Panda, and S. P. Singh, "A three-level fuzzy-2 DTC of induction motor drive using SVPWM," *IEEE Trans. Ind. Electron.*, vol. 63, no. 3, pp. 1467–1479, Mar. 2016.

[56] M. Montanari, S. M. Peresada, C. Rossi, and A. Tilli, "Speed sensorless control of induction motors based on a reduced-order adaptive observer," *IEEE Trans. Control Syst. Technol.*, vol. 15, no. 6, pp. 1049–1064, Nov. 2007.

[57] H. K. Khalil, E. G. Strangas, and S. Jurkovic, "Speed observer and reduced nonlinear model for sensorless control of induction motors," *IEEE Trans. Control Syst. Technol.*, vol. 17, no. 2, pp. 327–339, March 2009.

[58] F. –Z. Peng and T. Fukao, "Robust speed identification for speed-sensorless vector control of induction motors," *IEEE Trans. Industry Appl.*, vol. 30, no. 5, pp. 1234–1240, Sep. 1994.

[59] V. Verma, C. Chakraborty, S. Maiti, and Y. Hori, "Speed sensorless vector controlled induction motor drive using single current sensor," *IEEE Trans. Energy Convers.*, vol. 28, no. 4, pp. 938–950, Dec. 2013.

[60] M. Jones, S. N. Vukosavic, D. Dujic, and E. Levi, "A synchronous current control scheme for multiphase induction motor drives," *IEEE Trans. Energy Convers.*, vol. 24, no. 4, pp. 860–868, Dec. 2009.

[61] A. T. Alexandridis, G. C. Konstantopoulos, and Q. C. Zhong, "Advanced integrated modeling and analysis for adjustable speed drives of induction motors operating with minimum losses," *IEEE Trans. Energy Convers.*, vol. 30, no. 3, pp. 1237–1246, Sept. 2015.

[62] M. Mengoni, L. Zarri, A. Tani, G. Serra, and D. Casadei, "Stator flux vector control of induction motor drive in the field weakening region," *IEEE Trans. Power Electron.*, vol. 23, no. 2, pp. 941–949, Mar. 2008.

[63] G. Pellegrino, R. I. Bojoi, and P. Guglielmi, "Unified direct-flux vector control for AC motor drives," *IEEE Trans. Industry Appl.*, vol. 47, no. 5, pp. 2093–2102, Sep. 2011.

[64] S. M. A. Cruz, A. Stefani, F. Filippetti, and A. J. M. Cardoso, "A new model-based technique for the diagnosis of rotor faults in RFOC induction motor drives," *IEEE Trans. Ind. Electron.*, vol. 55, no. 12, pp. 4218–4228, Dec. 2008.

[65] M. Comanescu and L. Xu, "An improved flux observer based on PLL frequency estimator for sensorless vector control of induction motors," *IEEE Trans. Ind. Electron.*, vol. 53, no. 1, pp. 50–56, Feb. 2005.

[66] C. Gerada, K. J. Bradley, M. Sumner, and P. Sewell, "Evaluation and modeling of cross saturation due to leakage flux in vector-controlled induction machines," *IEEE Trans. Industry Appl.*, vol. 43, no. 3, pp. 694–702, May. 2007.

[67] R. –J. Wai and K. –M. Lin, "Robust decoupled control of direct field-oriented induction motor drive," *IEEE Trans. Ind. Electron.*, vol. 52, no. 3, pp. 837–854, Jun. 2005.

[68] A. Consoli, G. Scarcella, and A. Testa, "Slip-frequency detection for indirect field-oriented control drives," *IEEE Trans. Industry Appl.*, vol. 40, no. 1, pp. 194–201, Jan. 2004.

[69] J. O. Pinto, B. K. Bose, and L. E. B. da Silva, "A stator-flux-oriented vector-controlled induction motor drive with space-vector PWM and flux-vector synthesis by neural networks," *IEEE Trans. Industry Appl.*, vol. 37, no. 5, pp. 1308–1318, Sep. 2001.

[70] L. J. Garces, "Parameter adaption for the speed-controlled static AC drive with a squirrel-cage induction motor," *IEEE Trans. Industry Appl.*, vol. IA-16, no. 2, pp. 173–178, Mar. 1980.

[71] M. S. Zaky, "Stability analysis of speed and stator resistance estimators for sensorless induction motor drives," *IEEE Trans. Ind. Electron.*, vol. 59, no. 2, pp. 858–870, Feb. 2012.

[72] T. –S. Kwon, M. –H. Shin, and D. –S. Hyun, "Speed sensorless stator flux-oriented control of induction motor in the field weakening region using luenberger observer," *IEEE Trans. Power Electron.*, vol. 20, no. 4, pp. 864–869, Jul. 2005.

[73] P. Y. Lin and Y. S. Lai, "Novel voltage trajectory control for field-weakening operation of induction motor drives," *IEEE Trans. Industry Appl.*, vol. 47, no. 1, pp. 122–127, Jan. 2011.

[74] M. S. Zaky, M. M. Khater, S. S. Shokralla, and H. A. Yasin, "Wide-speed-range estimation with online parameter identification schemes of sensorless induction motor drives," *IEEE Trans. Ind. Electron.*, vol. 56, no. 5, pp. 1699–1707, May 2009.

[75] M. Masiala, B. Vafakhah, J. Salmon, and A. M. Knight, "Fuzzy self-tuning speed control of an indirect field-oriented control induction motor drive," *IEEE Trans. Industry Appl.*, vol. 44, no. 6, pp. 1732–1740, Nov. 2008.

[76] M. Salo and H. Tuusa, "Vector-controlled PWM current-source-inverter-fed induction motor drive with a new stator current control method," *IEEE Trans. Ind. Electron.*, vol. 52, no. 2, pp. 523–531, Apr. 2005.

[77] M. Boussak and K. Jarray, "A high-performance sensorless indirect stator flux orientation control of induction motor drive," *IEEE Trans. Ind. Electron.*, vol. 53, no. 1, pp. 41–49, Feb. 2005.

[78] G. K. Singh, D. K. P. Singh, K. Nam, and S. K. Lim, "A simple indirect field-oriented control scheme for multiconverter-fed induction motor," *IEEE Trans. Ind. Electron.*, vol. 52, no. 6, pp. 1653–1659, Dec. 2005.

[79] S. Peresada, A. Tilli, and A. Tonielli, "Theoretical and experimental comparison of indirect field-oriented controllers for induction motors," *IEEE Trans. Power Electron.*, vol. 18, no. 1, pp. 151–163, Jan. 2003.

[80] I. Takahashi and T. Noguchi, "A new quick-response and high-efficiency control strategy of an induction motor," *IEEE Trans. Industry Appl.*, no. 5, pp. 820–827, Sep. 1986.

[81] M. Depenbrock, "Direct self-control (DSC) of inverter-fed induction machine," *IEEE Trans. Power Electron.*, vol. 3, no. 4, pp. 420–429, Oct. 1988.

[82] L. Yang, X. Ma, and D. Dai, "Hopf bifurcation in doubly fed induction generator under vector control," *Chaos, Sol. Fract.*, vol. 41, no. 5, pp. 2741–2749, 2009.

[83] M. J. Duran, F. Salas, and M. R. Arahal, "Bifurcation analysis of five-phase induction motor drives with third harmonic injection," *IEEE Trans. Ind. Electron.*, vol. 55, no. 5, pp. 2006–2014, May 2008.

[84] G. Chen, D. J. Hil, and X. Yu, *Bifurcation control: theory and applications*. Springer Science & Business Media, 2003, vol. 293.

[85] G. Espinosa-Perez, G. W. Chang, R. Ortega, and E. Mendes, "On field-oriented control of induction motors: tuning of the PI gains for performance enhancement," in *Proc. IEEE Conf. Decision Control*, 1998, pp. 971–976.

[86] M. Rashed, P. F. A. MacConnell, A. F. Stronach, and P. Acarnley, "Sensorless indirect-rotor-field-orientation speed control of a permanent-magnet synchronous motor with stator-resistance estimation," *IEEE Trans. Ind. Electron.*, vol. 54, no. 3, pp. 1664–1675, June 2007.

[87] A. V. R. Teja, V. Verma, and C. Chakraborty, "A new formulation of reactive-power-based model reference adaptive system for sensorless induction motor drive," *IEEE Trans. Ind. Electron.*, vol. 62, no. 11, pp. 6797–6808, Nov. 2015.

[88] H. K. Khalil, *Nonlinear Systems*, 3rd ed. Upper Saddle River, NJ: Prentice-Hall, 2002.

[89] Y. A. Kuznetsov, *Elements of applied bifurcation theory*, 3rd ed. Springer-Verlag, 2004.

[90] J. Q. Sun and A. C. J. Luo, *Bifurcation and chaos in complex systems*. Elsevier, 2006, vol. 1.

[91] S. Banerjee and G. C. Verghese, *Nonlinear Phenomena in Power Electronics: Attractors, Bifurcations, Chaos, and Nonlinear Control*. Piscataway, NJ: IEEE Press, 2001.

[92] Allan Clark, *Elements of abstract algebra*. Courier Corporation, 1984.

[93] F. Salas, R. Reginatto, F. Gordillo, and J. Aracil, "Bogdanov-takens bifurcation in indirect field oriented control of induction motor drives," in *Proc. IEEE Conf. Decision Control*, vol. 4, 2004, pp. 4357–4362.

[94] G.-W. Chang, G. Espinosa-Perez, E. Mandes, and R. Ortega, "Tuning rules for the PI gains of field-oriented controllers of induction motors," *IEEE Trans. Ind. Electron.*, vol. 47, no. 3, pp. 592–602, Jun. 2000.

[95] A. S. Bazanella, R. Reginatto, and R. Valiati, "On hopf bifurcations in indirect field oriented control of induction motors: designing a robust PI controller," in *Decision and Control, 1999. Proceedings of the 38th IEEE Conference on*, 1999, pp. 689–694.

[96] S. M. Gadoue, D. Giaouris, and J. W. Finch, "MRAS sensorless vector control of an induction motor using new sliding-mode and fuzzy-logic adaptation mechanisms," *IEEE Trans. Energy Convers.*, vol. 25, no. 2, pp. 394–402, 2010.

[97] H. Sira-Ramírez, F. González-Montañez, J. Alexander Cortés-Romero, and A. Luviano-Juárez,, "A robust linear field-oriented voltage control for the induction motor: experimental results," *IEEE Trans. Ind. Electron.*, vol. 60, no. 8, pp. 3025–3033, 2013.

[98] M. N. Uddin and S. W. Nam, "Development of a nonlinear and model-based online loss minimization control of an IM drive," *IEEE Trans. Energy Convers.*, vol. 23, no. 4, pp. 1015–1024, Dec. 2008.

[99] ——, "Development and implementation of a nonlinear-controller-based IM drive incorporating iron loss with parameter uncertainties," *IEEE Trans. Ind. Electron.*, vol. 56, no. 4, pp. 1263–1272, Apr. 2009.

[100] C. Garcia, J. Rodriguez, C. Silva, C. Rojas, P. Zanchetta, and H. Abu-Rub, "Full predictive cascaded speed and current control of an induction machine," *IEEE Trans. Energy Convers.*, vol. 31, no. 3, pp. 1059–1067, Sep. 2016.

[101] G. C. Konstantopoulos, A. T. Alexandridis, and E. D. Mitronikas, "Bounded nonlinear stabilizing speed regulators for VSI-fed induction motors in field-oriented operation," *IEEE Trans. Control Syst. Technol.*, vol. 22, no. 3, pp. 1112–1121, May 2014.

[102] D. M. Brod and D. W. Novotny, "Current control of VSI-PWM inverters," *IEEE Trans. Industry Appl.*, vol. IA-21, no. 3, pp. 562–570, May 1985.

[103] R. D. Lorenz and D. B. Lawson, "Performance of feedforward current regulators for field-oriented induction machine controllers," *IEEE Trans. Industry Appl.*, vol. IA-23, no. 4, pp. 597–602, Jul./Aug. 1987.

[104] M. P. Kazmierkowski and L. Malesani, "Current control techniques for three-phase voltage-source PWM converters: A survey," *IEEE Trans. Ind. Electron.*, vol. 45, no. 5, pp. 691–703, Oct. 1998.

[105] F. B. d. Blanco, M. W. Degner, and R. D. Lorenz, "Dynamic analysis of current regulators for AC motors using complex vectors," *IEEE Trans. Industry Appl.*, vol. 35, no. 6, pp. 1424–1432, Nov. 1999.

[106] S. -M. Yang and C. -H. Lee, "A deadbeat current controller for field oriented induction motor drives," *IEEE Trans. Power Electron.*, vol. 17, no. 5, pp. 772–778, Sep. 2002.

[107] V. Verma, C. Chakraborty, S. Maiti, and Y. Hori, "Speed sensorless vector controlled induction motor drive using single current sensor," *IEEE Trans. Energy Convers.*, vol. 28, no. 4, pp. 938–950, Dec. 2013.

[108] T. M. Rowan and R. J. Kerkman, "A new synchronous current regulator and an analysis of current-regulated PWM inverters," *IEEE Trans. Industry Appl.*, vol. IA-22, no. 4, pp. 678–690, Jul./Aug. 1986.

[109] A. G. Yepes, A. Vidal, J. Malvar, O. López, and J. D. -Gandoy, "Tuning method aimed at optimized settling time and overshoot for synchronous proportional-integral current control in electric machines," *IEEE Trans. Power Electron.*, vol. 29, no. 6, pp. 3041–3054, Jun. 2014.

[110] L. A. Amézquita-Brooks, J. Licéaga-Castro, E. Licéaga-Castro, and C. E. Ugalde-Loo, "Induction motor control: Multivariable analysis and effective decentralized control of stator currents for high-performance applications," *IEEE Trans. Ind. Electron.*, vol. 62, no. 11, pp. 6818–6832, Nov. 2015.

[111] J. C. Doyle, K. Glover, P. P. Khargonekar, and B. A. Francis, "State-space solutions to standard H_2 and H_∞ control problems," *IEEE Trans. Autom. Control*, vol. 34, no. 8, pp. 831–847, 1989.

[112] Y. -Y. Cao, J. Lam, and Y. -X. Sun, "Static output feedback stabilization: An ILMI approach," *Automatica*, vol. 34, no. 12, pp. 1641 – 1645, Dec. 1998.

[113] J. Gadewadikar, F. L. Lewis, K. Subbarao, K. Peng, and B. M. Chen, "H_∞ static output-feedback control for rotorcraft," *J. Intell. and Robot. Syst.*, vol. 54, no. 4, pp. 629–646, 2009.

[114] K. Cao, X. Gao, H. K. Lam, and A. Vasilakos, "H-infinity fuzzy PID control synthesis for Takagi Sugeno fuzzy systems," *Control Theory Appl., IET*, vol. 10, no. 6, pp. 607–616, 2016.

[115] H. Bevrani and T. Hiyama, "Multiobjective PI/PID control design using an iterative linear matrix inequalities algorithm," *Int. J. Control Automatn. and Syst.*, vol. 5, no. 2, pp. 117–127, 2007.

[116] F. Zheng, Q.-G. Wang, and T. H. Lee, "On the design of multivariable PID controllers via LMI approach," *Automatica*, vol. 38, no. 3, pp. 517–526, 2002.

[117] J. Chiasson, *Modeling and high performance control of electric machines*. Piscataway, NJ, USA: IEEE Press, 2005.

[118] P. Gahinet, A. Nemirovskii, A. J. Laub, and M. Chilali , *The LMI control toolbox*. The Math-Works Inc., Natick, Mass., May 1995.

[119] L. Harnefors and H.-P. Nee, "Model-based current control of AC machines using the internal model control method," *IEEE Trans. Industry Appl.*, vol. 34, no. 1, pp. 133–141, Jan 1998.

[120] D Arun Dominic and T. Raj Chelliah, "Analysis of field-oriented controlled induction motor drives under sensor faults and an overview of sensorless schemes," *ISA Trans.*, vol. 53, no. 5, pp. 1680–1694, 2014.

[121] N. Bounar, A. Boulkroune, and F. Boudjema, "Fuzzy adaptive controller for a DFI-motor," in *Complex System Modelling and Control Through Intelligent Soft Computations*, 2015, pp. 87–110.

[122] ——, "Adaptive fuzzy control of doubly-fed induction machine," vol. 16, no. 2, pp. 98–110, 2014.

[123] N. Bounar, A. Boulkroune, F. Boudjema, M. M'Saad, and M. Farza, "Adaptive fuzzy vector control for a doubly-fed induction motor," vol. 151, pp. 756–769, 2015.

[124] F. Lima, W. Kaiser, I. N. da Silva, and A. A. Oliveira Jr., "Speed neuro-fuzzy estimator applied to sensorless induction motor control," vol. 10, no. 5, pp. 2065–2073, 2012.

[125] L. A. Amézquita-Brooks, E. Licéaga-Castro, J. Licéaga-Castro, and C. E. Ugalde-Loo, "Flux-torque cross-coupling analysis of FOC schemes: Novel perturbation rejection characteristics," *ISA Trans.*, vol. 58, pp. 446–461, 2015.

[126] J. Jung and K. Nam, "A dynamic decoupling control scheme for high-speed operation of induction motors," *IEEE Trans. Ind. Electron.*, vol. 46, no. 1, pp. 100–110, Feb 1999.

[127] F. Briz, M. W. Degner, and R. D. Lorenz, "Analysis and design of current regulators using complex vectors," *IEEE Trans. Industry Appl.*, vol. 36, no. 3, pp. 817–825, May 2000.

[128] S. Sangwongwanich and S. Suwankawin, "A speed-sensorless IM drive with modified decoupling control," in *Power Conversion Conference - Nagaoka 1997., Proceedings of the*, vol. 1, Aug 1997, pp. 85–90.

[129] J. Jung, S. Lim, and K. Nam, "PI type decoupling control scheme for high speed operation of induction motors," in *IEEE Power Electronics Specialists' Conference (PESC)*, vol. 2, Jun. 1997, pp. 1082–1085.

[130] F.-Jeng Lin, R.-Jong Wai, C.-Hong Lin, and D.-Chung Liu, "Decoupled stator-flux-oriented induction motor drive with fuzzy neural network uncertainty observer," *IEEE Trans. Ind. Electron.*, vol. 47, no. 2, pp. 356–367, Apr 2000.

[131] S. Suwankawin and S. Sangwongwanich, "A speed-sensorless IM drive with decoupling control and stability analysis of speed estimation," *IEEE Trans. Ind. Electron.*, vol. 49, no. 2, pp. 444–455, Apr 2002.

[132] B. Bahrani, S. Kenzelmann, and A. Rufer, "Multivariable-PI-based current control of voltage source converters with superior axis decoupling capability," *IEEE Trans. Ind. Electron.*, vol. 58, no. 7, pp. 3016–3026, 2011.

[133] S. K. Kommuri, J. J. Rath, K. C. Veluvolu, M. Defoort, and Y. C. Soh, "Decoupled current control and sensor fault detection with second-order sliding mode for induction motor," *Control Theory Appl., IET*, vol. 9, no. 4, pp. 608–617, 2015.

[134] N. Kumar, T. Chelliah, and S. Srivastava, "Adaptive control schemes for improving dynamic performance of efficiency-optimized induction motor drives," *ISA Trans.*, vol. 57, pp. 301–310, 2015.

[135] J. Lee, J. Hong, K. Nam, R. Ortega, L. Praly, and A. Astolfi, "Sensorless control of surface-mount permanent-magnet synchronous motors based on a nonlinear observer," *IEEE Trans. Power Electron.*, vol. 25, no. 2, pp. 290–297, 2010.

[136] W. K. Ho, O . P. Gan, E. B. Tay, and E. L. Ang, "Performance and gain and phase margins of well-known PID tuning formulas," *IEEE Trans. Control Syst. Technol.*, vol. 4, no. 4, pp. 473–477, 1996.

[137] D. N. Zmood and D. G. Holmes, "Stationary frame current regulation of PWM inverters with zero steady-state error," *IEEE Trans. Power Electron.*, vol. 18, no. 3, pp. 814–822, May. 2003.

[138] A. S. Bazanella, R. Reginatto, and R. Valiati, "On hopf bifurcations in indirect field oriented control of induction motors: Designing a robust PI controller," in *Proc. IEEE Conf. Decision Control*, 1999, pp. 689–694.

[139] M. A. Khan, M. N. Uddin, and M. A. Rahman, "Real time performance investigation of an intelligent controller based speed control of induction motor drives," in *2011 IEEE International Electric Machines Drives Conference (IEMDC)*, May 2011, pp. 164–169.

[140] X. Fu and S. Li, "A novel neural network vector control technique for induction motor drive," *IEEE Trans. Energy Convers.*, vol. 30, no. 4, pp. 1428–1437, Dec. 2015.

[141] H. S.-Ramírez, F. G.-Montañez, J. A. C.-Romero, and A. L.-Juárez, "A robust linear field-oriented voltage control for the induction motor: Experimental results," *IEEE Trans. Ind. Electron.*, vol. 60, no. 8, pp. 3025–3033, Aug. 2013.

[142] G. C. Konstantopoulos, A. T. Alexandridis, and E. D. Mitronikas, "Bounded nonlinear stabilizing speed regulators for VSI-fed induction motors in field-oriented operation," *IEEE Trans. Control Syst. Technol.*, vol. 22, no. 3, pp. 1112–1121, May 2014.

[143] G. S. Deaecto, J. C. Geromel, and J. Daafouz, "Dynamic output feedback h_∞ control of switched linear systems," *Automatica*, vol. 47, no. 8, pp. 1713 –1720, 2011.

[144] H. Li, X. Jing, and H. R. Karimi, "Output-feedback-based h_∞ control for vehicle suspension systems with control delay," *IEEE Trans. Ind. Electron.*, vol. 61, no. 1, pp. 436–446, Jan. 2014.

[145] H. D. Choi, C. K. Ahn, P. Shi, L. Wu, and M. T. Lim, "Dynamic output-feedback dissipative control for T-S fuzzy systems with time-varying input delay and output constraints," *IEEE Trans. Fuzzy Syst.*, vol. 25, no. 3, pp. 511–526, June 2017.

[146] I. Boldea and S. A. Nasar, "Unified treatment of core losses and saturation in the orthogonal-axis model of electric machines," *IEE Procd. B - Elect. Pow. Appl.*, vol. 134, no. 6, pp. 355–363, Nov. 1987.

[147] E. Levi, "Impact of iron loss on behavior of vector controlled induction machines," *IEEE Trans. Industry Appl.*, vol. 31, no. 6, pp. 1287–1296, Nov. 1995.

[148] E. Levi, M. Sokola, A. Boglietti, and M. Pastorelli, "Iron loss in rotor-flux-oriented induction machines: identification, assessment of detuning, and compensation," *IEEE Trans. Power Electron.*, vol. 11, no. 5, pp. 698–709, Sep. 1996.

[149] M. N. Uddin and S. W. Nam, "Development and implementation of a nonlinear-controller-based IM drive incorporating iron loss with parameter uncertainties," *IEEE Trans. Ind. Electron.*, vol. 56, no. 4, pp. 1263–1272, April 2009.

[150] S. Yamamoto, H. Hirahara, A. Tanaka, T. Ara, and K. Matsuse, "Universal sensorless vector control of induction and permanent-magnet synchronous motors considering equivalent iron loss resistance," *IEEE Trans. Industry Appl.*, vol. 51, no. 2, pp. 1259–1267, March 2015.

[151] Y. Y. Cao, Y. X. Sun, and W. J. Mao, "Output feedback decentralized stabilization: ILMI approach," *Systems & Control Letters*, vol. 35, no. 3, pp. 183–194, 1998.

[152] C. Scherer, P. Gahinet, and M. Chilali, "Multiobjective output-feedback control via LMI optimization," *IEEE Trans. Autom. Control*, vol. 42, no. 7, pp. 896–911, Jul 1997.

[153] J.-Jacques E Slotine and W. Li, *Applied nonlinear control*. Prentice hall Englewood Cliffs, NJ, 1991.

[154] R. Seydel, *Practical bifurcation and stability analysis*. Springer Science & Business Media, 2009.

[155] S. H Strogatz, *Nonlinear dynamics and chaos: with applications to physics, biology, chemistry, and engineering*. Westview press, 2014.

Dissemination

Accepted Journals

1. Jitendra Kr. Jain, Sandip Ghosh and Somnath Maity,"A Numerical Bifurcation Analysis of Indirect Vector-Controlled Induction Motor", IEEE Transactions on Control System Technology. DOI: 10.1109/TCST.2017.2658191

2. Jitendra Kr. Jain, Sandip Ghosh, Somnath Maity and Pawel Dworak,"PI Controller Design for Indirect Vector Controlled Induction Motor: A Decoupling Approach", ISA Transactions. DOI: 10.1016/j.isatra.2017.05.016

Article under preparation

1. Jitendra Kr. Jain, Sandip Ghosh and Somnath Maity,"Speed Loop PI Controller Design for Indirect Vector Controlled Induction Motor"(Under Review).

2. Jitendra Kr. Jain, Sandip Ghosh and Somnath Maity,"A Dynamic Controller Design for Indirect Vector Controlled Induction Motor".